ABSTRACT

Title of Document: ASSEMBLY OF SILVER NANOCUBE CLUSTERS AND TUNING OF SURFACE PLASMON RESONANCES FOR SURFACE-ENHANCED RAMAN SCATTERING

Seung Yong Lee, Doctor of Philosophy, 2012

Directed By: Professor Oded Rabin, Department of Materials Science and Engineering

To prepare surface-enhanced Raman scattering (SERS) substrate with metal nanoparticle clusters, various deposition methods were used: (1) vertical deposition (VertD), (2) electrophoretic deposition (EPD), and (3) block-copolymer templated deposition (BCPTD). The EPD is a high throughput process. Substrates for VertD can be reused. The BCPTD does not require the use of any lithography technique. By means of these three deposition methods, metal nanoparticles, including silver nanocubes and gold nanospheres, were positioned at pre-determined substrate sites.

Various parameters, such as angle between cluster axis and laser polarization, gap size, number of cubes in clusters and cluster configurations, were investigated for their effect on SERS. Hexagonal arrays of gold nanoparticles with precisely controlled gap were investigated. The proximity of the plasmon resonance to the laser wavelength was correlated to the SERS enhancement. A database of SERS enhancement of silver nanocube clusters from monomers to tetramers was generated.

The analysis of the structures and enhancements in this database reveals that clusters should be aligned with the laser polarization to achieve high SERS enhancement. Increasing cluster size from dimers to tetramers improves the reproducibility of enhancement factor values. Non face-to-face clusters are better in SERS enhancement than face-to-face clusters. Sharp corners at the junctions are essential for high SERS enhancement.

ASSEMBLY OF SILVER NANOCUBE CLUSTERS AND TUNING OF SURFACEPLASMON RESONANCES FOR SURFACE-ENHANCED RAMAN SCATTERING

By

Seung Yong Lee

Dissertation submitted to the Faculty of the Graduate School of the
University of Maryland, College Park, in partial fulfillment
of the requirements for the degree of
Doctor of Philosophy
2012

Advisory Committee:
Professor Oded Rabin, Chair
Professor Robert M. Briber
Professor Raymond J. Phaneuf
Professor Isaak D. Mayergoyz
Professor John Melngailis

Dedication

To

my extraordinary **Sangju** and **Junhee**

Acknowledgements

When I started my Ph.D studies, I was just a technician. Now, I feel I have become a scientist. I could not have done this without Prof. Rabin. I appreciate his devoted guidance. He is an ideal advisor and a natural-born professor. I'm so lucky to have him as my advisor. I am very thankful to Prof. Mayergoyz for his cheerful encouragement and energetic collaboration. Also, I would like express my gratitude to my committee members: Prof. Briber, Prof. Phaneuf, and Prof. Melngailis. Their help was invaluable to me throughout my research. I thank Ling for his diligent collaboration and kind explanations.

Jane has been open-minded and showed me unbelievable tolerance to other cultures. She is always a good lab-mate. We helped each other every single tough day. I appreciate her help.

I must express my sincere gratitude and endless respect to my wife, Sangju. If it were not for Sangju, I could not have started and could not have finished it. I could cross a desert because of you. I feel sorry for my daughter, Junhee. I could not spend much time with you so far, but I will. I appreciate my parents and my parents-in-law. They always pray for me. Lastly, I appreciate all KOSTAM members. Playing tennis and drinking with them helped to relieve my stress.

Table of Contents

List of Tables

List of Figures

List of Schemes

List of Symbols

λ: wavelength
a: radius of metal nanoparticle
σ_{ext}: extinction cross section
V: particle volume
ω: angular frequency
c: the speed of light
ε_m: dielectric constant of surrounding medium
ε: dielectric constant of metal
ε_1: real part of dielectric constant of metal
ε_2: imaginary part of dielectric constant of metal
$\mathbf{E}_{out}$: electric field outside the sphere
$\mathbf{E}_0$: electric field of the incident light
$\mathbf{E}_{induced}$: induced electric field
x, y, z: Cartesian coordinates
x, **y**, **z**: unit vectors along x, y, z coordinates.
α: polarizability
G: overall SERS enhancement
n: number of cubes in a cluster
d_{ij}: gap between pairs of particles
θ_{ij}: angle between two particle axis among the cluster and laser polarization direction
δ_i: rotational angle of a cube
A_i: peak area at 1078cm^{-1} of aminothiophenol molecule Raman spectra measured with the *i*-direction polarized laser
$F_{Weibull}$: cumulative fraction
b: scaling parameter
c: shape parameter
$I_{normalized}$: normalized light intensity
$I_{cluster}$: intensity of light scattered by a nanoparticle cluster
I_{blank}: intensity of light scattered by the silicon substrate

1 Introduction to Raman Scattering, Surface-Enhanced Raman scattering and Silver Nanocubes

1.1 Raman Scattering

In 1928, inelastic photon scattering, so called Raman scattering, was first discovered by Sir C. V. Raman.[1] He used sunlight as the source, a telescope as the collector, and his eyes as the detector (Figure 1.1). When the light is scattered by molecules, most of the photons are elastically scattered so that there is no change in the energy of the photons. Only a small portion of photons is inelastically scattered so that the photons gain or lose energy after scattering. The energy change reflects the excitation or relaxation of the vibrational or rotational modes of the molecule. Raman scattering is a very powerful tool for chemical analysis, since it provides direct information on vibrational modes of sample molecules. However, the cross-section of Raman scattering is very small.[2] A large amount of molecules are needed for Raman analysis of samples. Usually condensed samples, such as solids or liquids, have a sufficient quantity of molecules for Raman analysis. However, interesting samples are often too dilute to generate a detectable Raman signal. Surface-enhanced Raman scattering is one approach to overcome the drawback of low-sensitivity

.

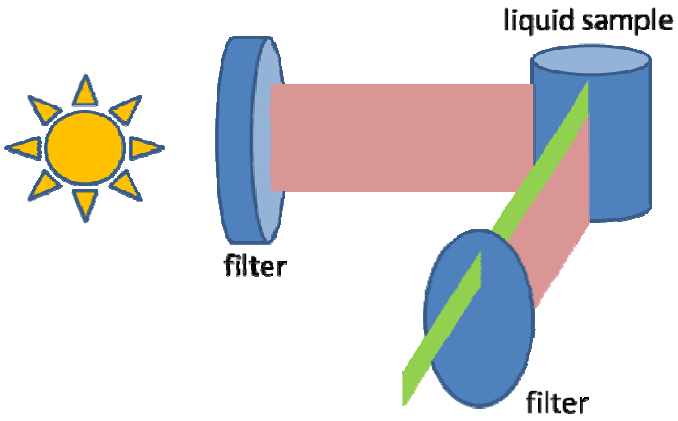

Figure 1.1. A diagram depicting Raman's experiment. Filtered light was scattered by a liquid sample. The scattered light was filtered again to separate components of inelastically scattered light from the scattered light.

1.2 Surface-Enhanced Raman Scattering (SERS)

SERS indicates the phenomenon that molecules adsorbed on (or located near) rough metal surfaces or metal nanostructures give out much stronger Raman signals than the molecules not near metal structures. The SERS is a sensitive analysis technique utilizing this phenomenon. The enhancement is sufficiently large to detect single molecules.[3] SERS phenomenon was discovered in 1977.[4] Molecules adsorbed on a rough metal surface exhibited a million times increase in their Raman signal. This large enhancement could not be accounted for simply by the increase in the number of molecules present on the rough metal surface. Due to the large enhancement, researchers have tried developing SERS substrates utilizing the SERS phenomenon. SERS substrates are ready-to-analyze devices providing large and reliable enhancement of Raman signal from sample molecules.

1.2.1 Mechanism

It is generally agreed that two mechanisms contribute to the overall large enhancement of SERS: an electromagnetic enhancement mechanism and a chemical enhancement mechanism.

The electromagnetic mechanism is based on the significantly amplified electromagnetic fields generated by the localized surface plasmon resonance (LSPR) of metal nanostructures.[5] The incident electromagnetic radiation excites surface plasmons in the metal nanostructure, which produce an enhanced electric field (amplified light) at the surface. The amplified light is Raman-scattered by molecules near the surface. Moreover, the Raman scattered light will also resonate with surface plasmons (under the right conditions). Then, the electric field of the Raman scattered light will be enhanced. Consequently, amplification of the electric field by the metal nanostructures occurs twice, *i.e.* once for the incident light and once for the Raman shifted light.

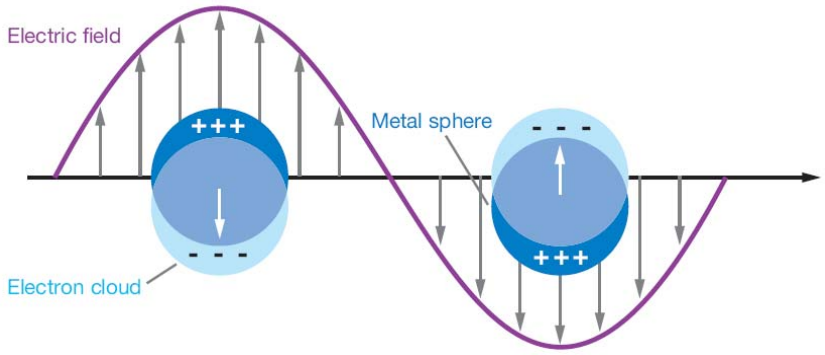

Figure 1.2. Schematic diagram illustrating a localized surface plasmon. The collective ocsillation of electrons is stimulated by the electric field of the incident light.[6]

To maximize both the amplifications, the surface plasmon resonance frequency of the metal nanostructure should be near that of the incident *and* Raman

scattered light. The plasmon resonance frequency of a metal nanostructure is determined by the size, shape, and composition of the metal nanostructure and the dielectric constant of medium (ε_m).

Mie solved Maxwell's equation to describe the scattering of light by a sphere.[7] Mie's solution can explain why the electric field near metal nanoparticles is amplified resulting in the enhancement of Raman signal and tell the conditions for maximizing the enhancement. The solution has the form of an analytical infinite series. When electromagnetic radiation is incident upon a metal nanostructure, the electric field of the radiation generates collective oscillations of the conduction electrons. For nanoparticles that are small compared to the wavelength λ of the exciting light ($2a << \lambda$), it can be assumed that only the dipole contributes to the extinction cross section σ_{ext} of the nanoparticles. Then, Mie's solution can be reduced into Equation 1.1 (dipole approximation),[8]

$$\sigma_{ext}(\omega) = 9\frac{\omega}{c}\varepsilon_m^{3/2}V\frac{\varepsilon_2(\omega)}{[\varepsilon_1(\omega)+2\varepsilon_m]^2+\varepsilon_2(\omega)^2} \qquad (1.1)$$

where V is the particle volume, ω is the angular frequency of the exciting light, c is the speed of light, and ε_m and $\varepsilon(\omega) = \varepsilon_1(\omega) + i\varepsilon_2(\omega)$ are the dielectric functions of the surrounding medium and the material itself. As indicated in Equation 1.1, the surface plasmon extinction band shows up when $\varepsilon_1(\omega) \sim -2\varepsilon_m(\omega)$, if $\varepsilon_2(\omega)$ is small or if it only weakly depends on ω. Equation 1.1 indicates that the peak position is size independent, in the contrary to the experimental evidence. The size dependency of the position of the surface plasmon extinction band can be accommodated by assuming size-dependent dielectric functions.[8] The optical behavior of larger ($2a > 30nm$) metal nanoparticles cannot be explained by Equation 1.1, since the extinction cross-

section of such nanoparticles is dominated by higher-order multipole absorption and scattering. The full Mie solution needs to be used. Qualitatively, the localized surface plasmon absorbance maximum shifts to longer wavelengths with increasing the size of the particles.

Assuming that a spherical particle whose radius is much smaller than the wavelength of light is embedded in a medium of dielectric constant ε_m and that the electric field E_0 of the incident light (electromagnetic wave) is a vector pointing along the z-axis, the electric field outside the sphere $\mathbf{E}_{out}$, can be expressed as[5]:

$$\mathbf{E}_{\text{out}} = \mathbf{E}_0 + \mathbf{E}_{\text{induced}} = E_0\mathbf{z} - \alpha E_0\left[\frac{\mathbf{z}}{r^3} - 3\frac{z}{r^5}(z\mathbf{z} + x\mathbf{x} + y\mathbf{y})\right] \quad (1.2)$$

$$\alpha = ga^3 \quad (1.3)$$

$$g = \frac{\varepsilon_1 - \varepsilon_m}{\varepsilon_1 + 2\varepsilon_m} \quad (1.4)$$

where the first term in Equation 1.2 is the applied field and the second term is the induced field. α is the polarizability of the sphere. E_0 is the magnitude of $\mathbf{E}_0$. Since the induced field is proportional to the metal polarizability, it becomes very large when ε_1 is equal to $-2\varepsilon_m$.

The intensity of light is proportional to the square of the electric field, $|\mathbf{E}_{out}|$, at the surface of the sphere (r = a). If |g| is large, then $|E_{out}|^2$ can be expressed as

$$|\mathbf{E}_{out}|^2 = {E_0}^2|g|^2(1 + 3\cos^2\theta) \quad (1.5)$$

where θ is the angle between the applied field polarization direction and the vector $\mathbf{r}$ that locates positions on the sphere surface. Therefore, the largest electric field intensity, $4{E_0}^2|g|^2$, is obtained when $\theta = 0$ and $\theta = 180^o$.

In SERS, Equation 1.5 determines the magnitude of the field at the sphere surface induced by the incident light. The second amplification happens to the

scattered Raman shifted light. We can determine the overall enhancement arising from incident and scattered fields,

$$G = \frac{{E_{out}}^2 {E'_{out}}^2}{{E_0}^4} \cong 16|g|^2|g'|^2 \qquad (1.6)$$

where the primed symbols indicate the values at the scattered frequency. The best way to get large enhancement is to make both fields resonate with surface plasmons.

The basics of the field enhancement by a metal nanosphere are described above. Field enhancements for other shapes, such as nanocubes and triangular nanoprisms, are usually calculated numerically, by using methods such as finite-difference time-domain (FDTD)[9] and discrete dipole approximation (DDA)[10].

In the electromagnetic enhancement mechanism, the enhancements of different molecules adsorbed on a particular surface should be identical. However, differences in the Raman intensity between CO and N_2 were reported experimentally though the polarizabilities of the molecules are nearly identical.[11] This discrepancy can be accounted for by a resonance Raman effect. Chemisorption of molecules generates new electronic states, which act as resonant intermediate states in Raman scattering.[12] Electrons or holes generated by excitation of the surface plamson are coupled to the HOMO or LUMO of the chemisorbed molecule (Figure 1.3). The existence of these states increases the probability of a Raman transition. This mechanism is site-specific and analyte-dependent.[13] For chemical enhancement, it is required that the molecules will be directly adsorbed to the metal surface. The chemical enhancement is thought to contribute an average enhancement factor of 100.

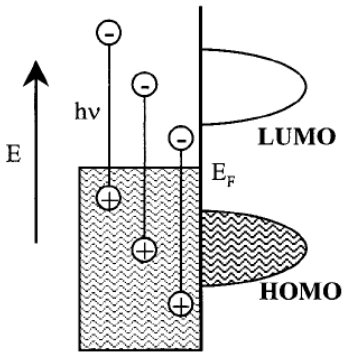

Figure 1.3. Schematic of relative energies of excited electron-hole pairs generated via excitation of the surface plasmon in the metal with respect to the HOMO and LUMO of the chemisorbed molecule.[12]

1.2.2 Important Factors in SERS

Large SERS enhancements have been observed in clusters consisting of metal nanoparticles. So-called 'hot-spots' showing large enhancement are generated by coupling between the nanoparticles and are located at junctions between nanoparticles. As mentioned in Section 1.2.1, to maximize the Raman enhancement, the surface plasmon resonance should be tuned to match with the incident light wavelength. In the tuning of the plasmon resonance of metal nanoparticle clusters, gap size and number of nanoparticles in clusters are important factors.

Many researchers have investigated the influence of the gap size on SERS enhancement.[14-18] Top-down approach utilizing e-beam lithography has been adopted mainly due to its high precision.[14, 15, 18]

Jain *et al.* formed gold nanodisk pair arrays with different gap size and investigated plasmon resonance frequencies from the arrays using microabsorption spectroscopy.[14] The experimental result in Figure 1.4 shows a red-shift of the plasmon resonance which increases as the metal nanodisks approach each other.

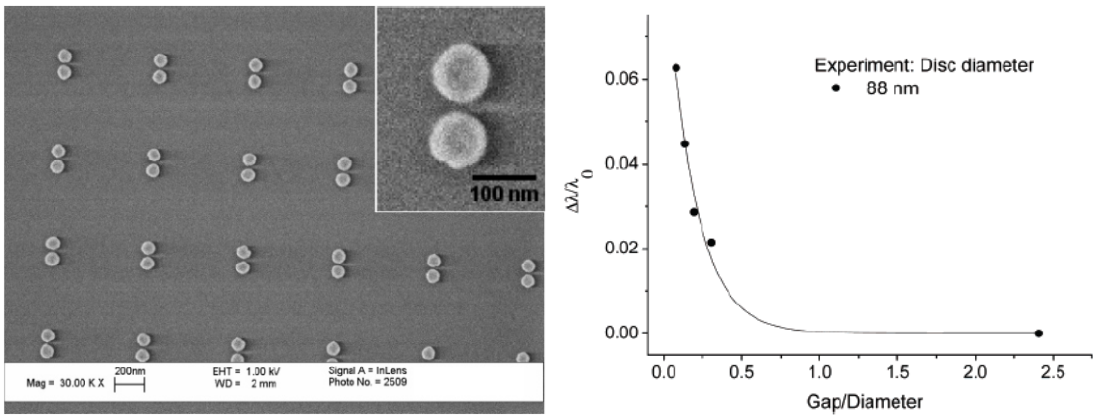

Figure 1.4. (a) Gold nanodisk pair array. (b) Plasmon resonance frequency change as a function of gap size.[14]

Schuck *et al.* reported the electric field enhancement trend with different gap sizes.[15] They fabricated metallic bowtie structures with different gap sizes by e-beam lithography technique and measured two-photon photoluminescence (TPPL). The TPPL results were used to determine the absolute values of the optical field enhancements of single Au bowties (by comparing the strength of TPPL from bowties with TPPL from a smooth Au film). The E^4 enhancement factor was over 10^6 for bowties with the smallest gaps of 16nm when a 830nm Ti:sapphire laser was used for excitation (Figure 1.5). As the gap size increased from 16 to 50nm, the E^4 enhancement factor decreased exponentially. Beyond a 50nm gap, the E^4 enhancement factors became almost constant, which indicates that there is almost no coupling between the two triangular features of the bowtie beyond this and that the constant value is associated with the enhancement by the individual triangular feature.

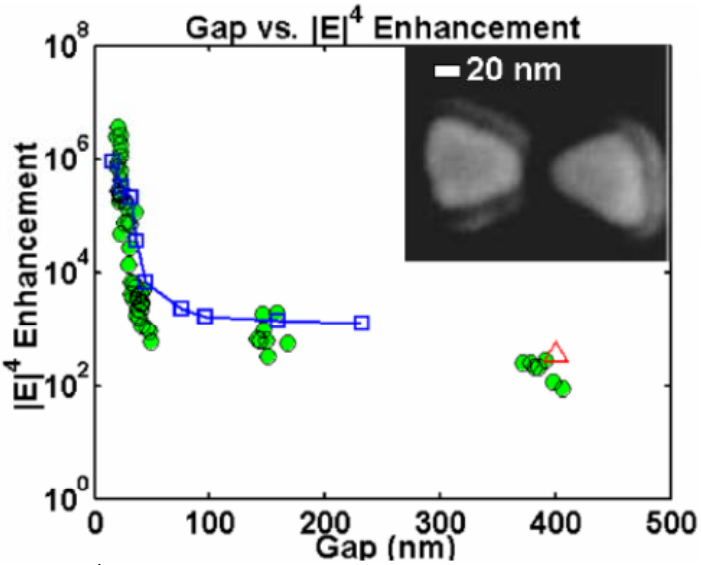

Figure 1.5. (circles) E^4 enhancement values of bowtie structure as a function of gap size. (open squares) Theoretical values.[15]

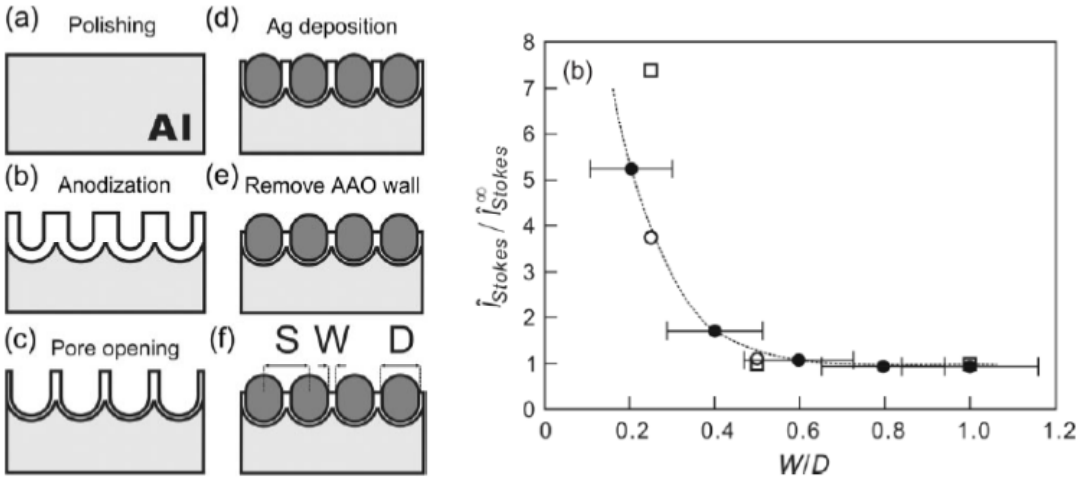

Figure 1.6. (left) Schematic diagram describing sample preparation. (right) Peak intensity change as a function of the ratio of gap size to particle diameter, (filled circle) experimental result, (open circle) theoretical prediction by Xu and Dignam and (open square) by Garcia-Vidal and Pendry. (dashed line) Trend line.[16]

Wang *et al.* reported that the SERS signal intensity increased exponentially as the gap size between silver nanoparticles decreased.[16] As shown in Figure 1.6, periodic silver nanoparticle arrays with different gap sizes were prepared using anodic alumina templates. The experimental result of Raman enhancement with

different gap sizes matched with previous theoretical prediction of interparticle-coupling-induced Raman enhancement.

Siegfried *et al.* fabricated gold nanogap arrays using interference lithography and shadow evaporation (Figure 1.7).[17] Sub-10nm gap sizes were realized and SERS signals were measured from the structures with different gap sizes. As shown in Figure 1.7, the SERS intensity increases strongly for gap sizes below 20nm. SERS intensity decreased when the gap size was less than 5nm, which is opposite to the expectation. Coalesce of gap side walls might cause this discrepancy of the experimental result from the expectation. Clearly the SERS intensity depends on the polarization direction (Figure 1.7 inset).

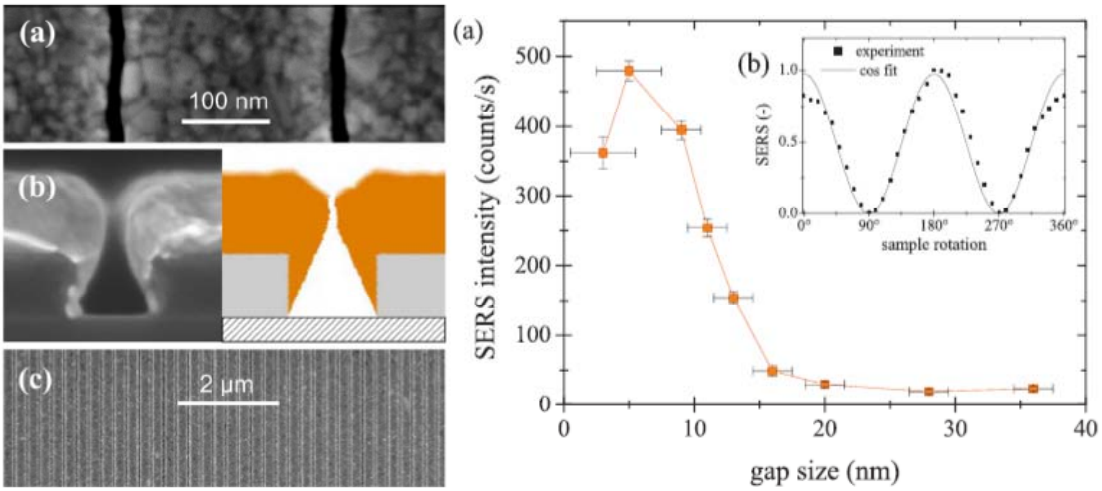

Figure 1.7. (left) Micrographs and scheme showing the gold nanogap arrays. (right) SERS intensities with different gap sizes. (inset) Normalized SERS intensity as a function of sample rotation**)**.[17]

Hatab *et al.* prepared suspended optical gold bowtie nanoantennae with various gap sizes (Figure 1.8).[18] The SERS enhancement factor increased exponentially with decreasing gap size as shown in Figure 1.8. The density of repeating bowtie units affects the SERS enhancement as well. If center-to-center

distance (ccd) without changing row-to-row distance (rrd) was controlled to get SERS response, it could provide more valuable result.

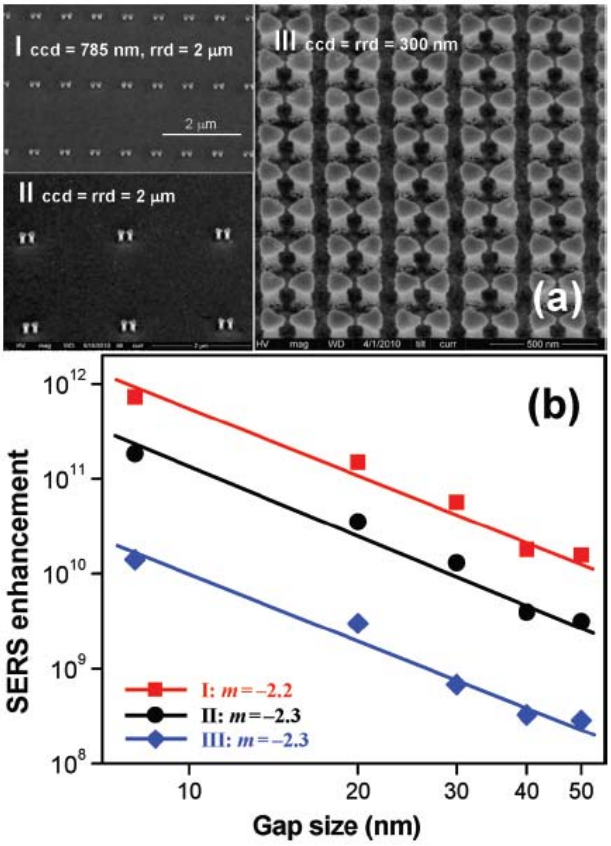

Figure 1.8. (a) Morphologies of bowtie arrays with different center-to-center distances (ccd) and row-to-row distances (rrd). (b) SERS enhancement change of each array with different gap sizes. Array I (ccd=785nm, rrd=2um) shows the highest EF value trend, while the most close-packed one, array III (ccd=rrd=300nm), recorded the lowest EF value trend.[18]

The cited works discussed above are valuable, since they elucidated the effect of gap size on the plasmon resonance frequency shift, electric field enhancement, and SERS intensity with precise control over gap size. However, as mentioned in Section 1.2.1, the most important factor for SERS enhancement is the difference between the plasmon resonance frequency and the wavelengths of incident and scattered light. The results introduced above will change if a different incident laser is used. Thus, when designing SERS substrates, the effect of (a) gap size on plasmon resonance frequency

and SERS enhancement (or field enhancement) and (b) wavelength of incident laser should be considered together.

When clusters consisting of metal nanoparticles are used for SERS substrates, the configuration and the number of nanoparticles affect the surface plasmon resonance. Several researchers reported plasmon resonance changes with cluster size.[19-21]

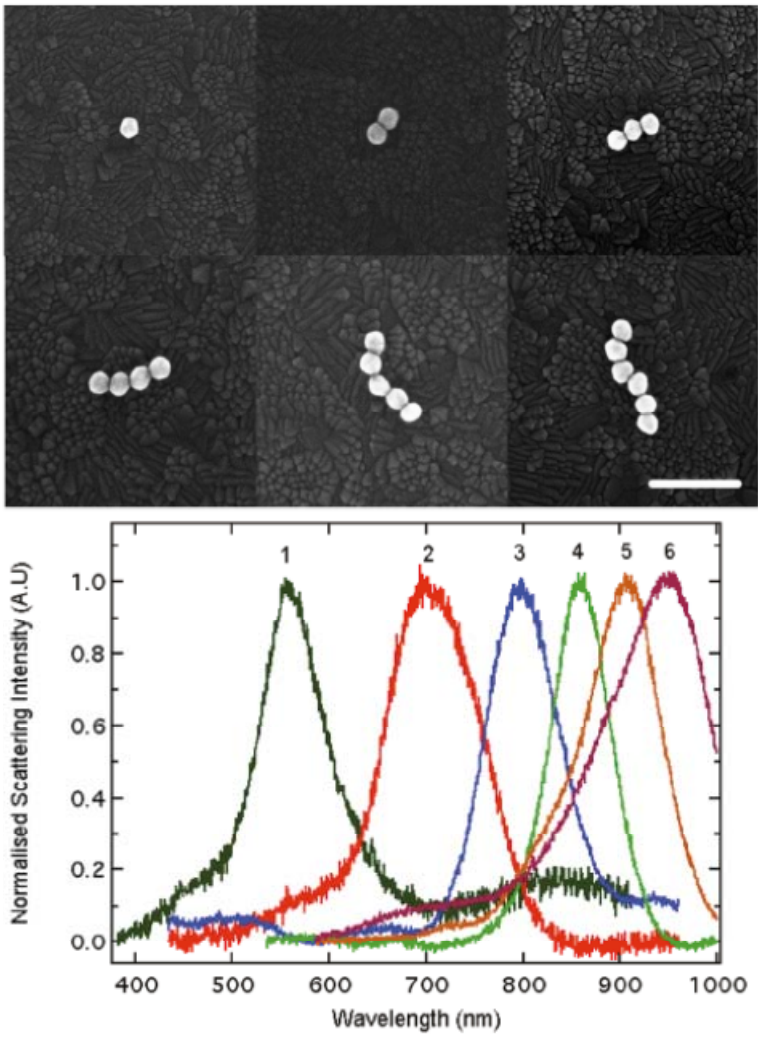

Figure 1.9. (upper) SEM images of self-assembled nanoparticle chains. Average diameter of gold particles is 64nm. Scale bar: 250nm. (lower) Normalized spectra of the nanoparticle chains in the upper images. Numbers on the peaks indicate chain length.[19]

A recent report by Barrow *et al.* shows a clear relation between the number of gold nanospheres in clusters and the plasmon resonance frequency.[19] The gold nanospheres were synthesized using a seed-mediated wet chemical method.[22] Clusters were formed in solution using thiolated single strand oligonucleotides via the method of Yao *et a*.[23] Clusters were deposited on an ITO substrate (Figure 1.9). Linear chains were selected for the optical measurements. The plasmon resonance peak red-shifts from 540nm to 950nm as the chain length increases from 1 (monomer) to 6 (hexamer).

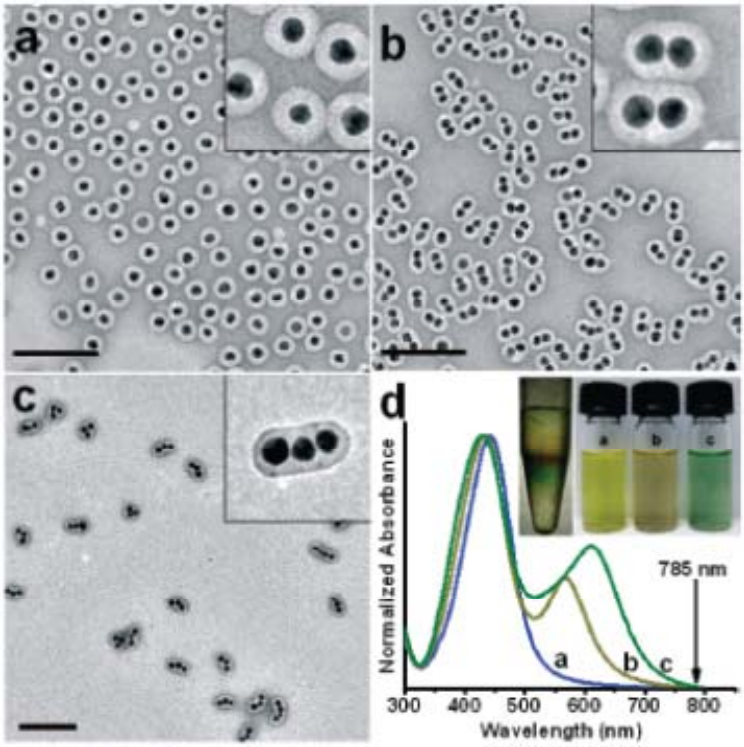

Figure 1.10. (a-c) TEM images and (d) UV-vis spectra of the samples enriched with Au@Ag (a) monomers, (b) dimers, and (c) trimers. Clusters are encapsulated in polystylene-*b*-poly(acrylic acid). Scale bars: 200nm.[20]

Chen *et al.* also reported clear spectral evolution and SERS enhancement with different cluster sizes as shown in Figure 1.10.[20] They prepared Au@Ag core-shell

nanoparticles. NaCl was used to induce nanoparticle aggregation. The clusters were sorted by size using differential centrifugation. Raman measurement with a 785nm laser indicates that the signals from dimers are 16 times stronger than those from monomers and the signals from trimers are 87 times stronger than those of monomers. The fact that this paper presented the formation of clusters, their UV-vis spectra and SERS response should be emphasized. It provides valuable information on SERS from clusters.

Wustholz *et al.* reported spectral change with cluster size and configuration from 30 clusters ranging from dimers to heptamers.[21] SiO_2-encapsulated Au nanoparticles clusters were prepared and characterized. Dramatic change in spectra with cluster size and configuration indicates the importance of the cluster size effect on the plasmon resonance. They claimed that a single hot-spot between two particles is sufficient to realize high EF value, and the 'extra' particles do not contribute significantly to the enhancement.

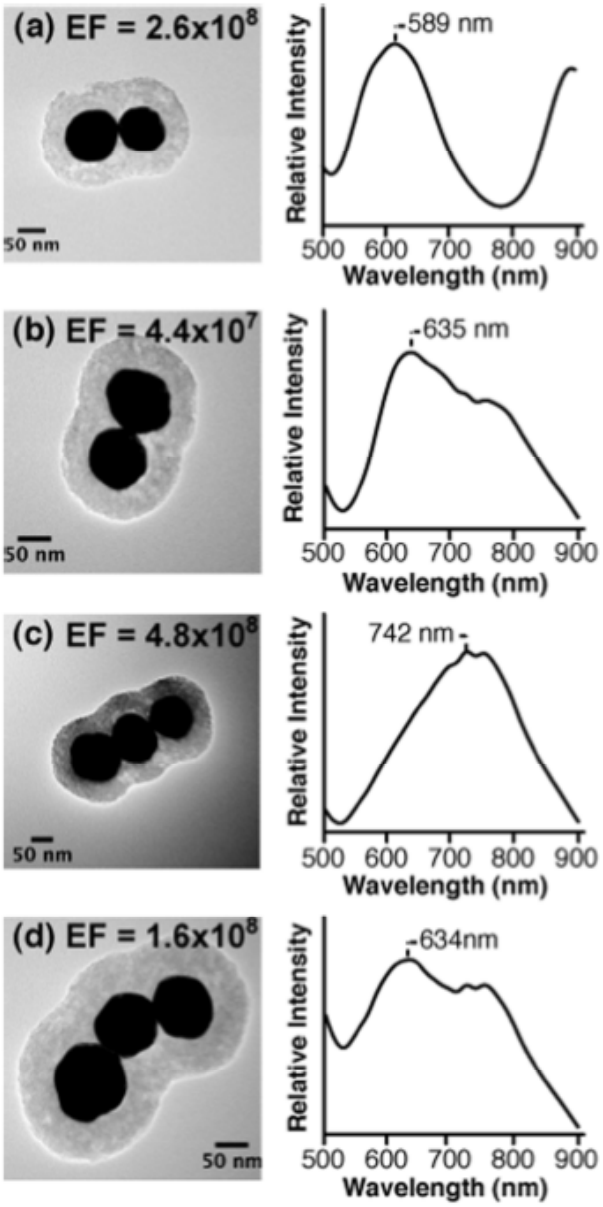

Figure 1.11. Cluster morphologies and LSPR spectra of dimers and trimers.[21]

The above cited works show spectral change by clustering.[19-21] Liquid suspensions and samples made by drop-casting were used for these experiments. Even though they provide valuable scientific information, neither the alignment of clusters nor the number of nanoparticles in clusters could be controlled in these approaches. Practically, clusters should be aligned along the laser polarization

direction and users should know where the clusters exist. To prepare SERS substrates for a certain laser, the number of particles in the clusters (determining the plasmon resonance) should be finely tuned. Controllability over clustering and position needs to be improved to realize SERS substrates based on nanoparticle clusters.

1.3 Organization of the Thesis

The ultimate objective of my thesis is to prepare SERS substrates showing high and reproducible enhancement with metal nanoparticles. As a first step, we demonstrated several ways of controlling the position of metal nanostructures, and then we tuned the plasmon resonance frequency of the metal nanostructures. We utilized several different deposition methods to guide metal nanoparticles into pre-determined positions. Once we can form addressable arrays of the nanoparticles, we can build a database of SERS responses from the nanostructures with various configurations.

Chapter 2: In this chapter, we will show how to synthesize AgNCs and why we choose AgNCs as the main building block for SERS substrates. Preheating time, an important parameter in synthesizing AgNCs, will be introduced.

Chapter 3: This chapter focuses on the SERS enhancement by AgNC dimers. AgNC dimers were formed in the pores by vertical deposition utilizing capillary force. The effect of dimer direction, gap size, and configuration on SERS enhancement was investigated.

Chapter 4: Electrophoretic deposition was adopted. AgNC dimers, trimers, and tetramers were successfully formed at pre-determined positions. The SERS

enhancement factor trend change by cluster size was investigated. A desirable configuration of clusters is suggested.

Chapter 5: Block-copolymer templates were used for guiding the placement of gold nanospheres, resulting in hexagonal arrays of gold nanospheres. The plasmon resonance was tuned by adjusting the size of the gold nanospheres and decreasing the gaps between them. We measured SERS enhancements of substrates with different gap size using different lasers. We emphasize the importance of matching of the laser wavelength to the plasmon resonance frequency.

Chapter 6: Unintended silver deposits along sidewalls of RIE-etched area were encountered. The nature and growth mechanism of the deposits were investigated and a way to control their presence was developed. We succeed in the localization of the RIE products and metal nanostructures. We use the metal nanostructures as catalysts for the growth silicon nanowires.

2 Synthesis of Silver Nanocubes (AgNCs)

2.1 Introduction

Each cube contains 8 sharp corners. Concentrated charge at the corners of nanocubes can generate higher electric fields than at the surface of spherical nanoparticles (Figure 2.1).[24] We can expect bigger enhancement from nanocubes, since SERS enhancement is approximately proportional to E^4. In addition to large electric field enhancement at nanocube corners, nanocube clusters can form junctions with larger areas of intense field than nanosphere clusters. Thus, nanocubes are promising for the fabrication of SERS substrates.

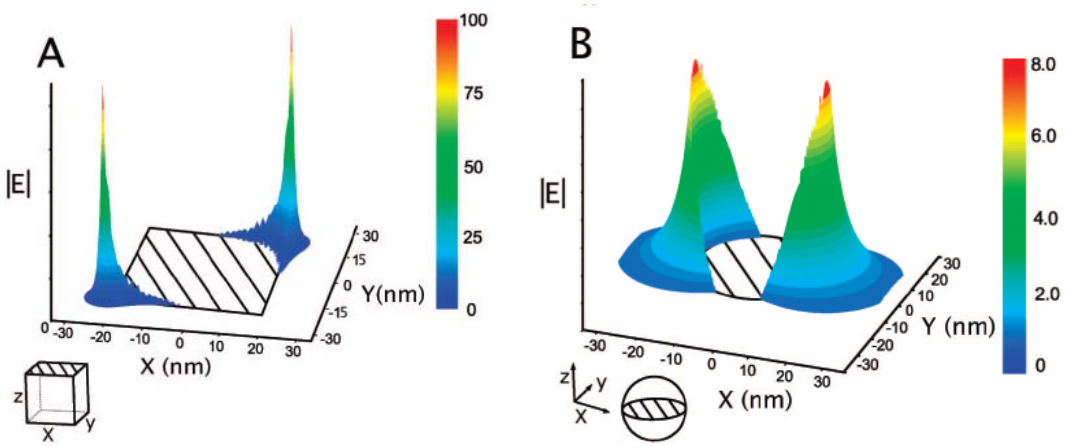

Figure 2.1. The electric field enhancement contours for a Ag nanocube of 38nm in edge length (A), and a Ag nanosphere of 35nm in diameter with an excitation wavelength of 515nm (B). For part A, the E-field of the incident light is along the [110] direction, and for part B, parallel to the x-axis.[24]

Silver is known as the best material for SERS. The chemistry and the crystallinity of the AgNCs is well-controlled at the stage of the synthesis. The AgNCs have perfect (100) facets and sharp corners. The roughness of AgNC surface is very

uniform due to the facets. All the cubes are single-crystals, eliminating effects of grain boundary and polycrystallinity. With AgNCs, we can focus on the effect of AgNC cluster configuration factors, such as geometric configuration and cluster size (number of nanocubes in a cluster).

For the reasons mentioned above, we regard AgNCs as ideal building block for SERS, either maximizing junction area or amplifying electric field by the corners. The first report on AgNCs, by Sun and Xia, appeared in Science 2002.[25] The AgNCs were synthesized by the polyol process. In the polyol process, alcohols containing multiple hydroxyl groups, such as ethylene glycol and pentanediol, act as both reductant and solvent. A capping agent, poly(vinyl pyrrolidone) (PVP) was used to induce the cubic shape. It is believed that selective interaction between PVP and various crystallographic planes of fcc silver suppresses the growth rate along the <100> direction and enhance the growth rate along the <111> direction, which results in the formation of single-crystalline nanocubes. The molar ratio between the repeating units of PVP and Ag ions determines the morphology of the products.[25, 26] A high ratio is used for nanocubes and a low ratio for nanowires. The addition of trace amounts of chloride ions helps the formation of nanocubes, since the precipitation of the low-solubility salt AgCl prevents the fast reduction of the metal ions that causes the formation of multiply twinned particles. Xia et al. suggested that the presence of gaseous oxygen and chloride ions enhances the etching of high-energy twin planes, which results in the sole formation of single-crystalline particles.[27]

2.2 Synthesis of AgNCs

Silver nanocubes were prepared according to the experimental procedure by Tao *et al.* in *Angew. Chem. Int. Ed.* 2006.[26] In this process, silver nitrate (Alfa Aesar, 99.995% metal basis) was used as precursor, polyvinypyrrolidone (PVP) (M_w=55K, SigmaAldrich) acted as shape controller, and 1,5-pentanediol (PDOH) (Acros, 98%) acted as solvent as well as reducing agent. It was reported that the PDOH, due to its high viscosity, slows the diffusion rate of reactants to encourage nucleation of single-crystalline particles over the multiply twinned particles which initiate nanowire growth.[26] However, the reaction temperature with PDOH is higher than that with ethylene glycol. We think the usage of PDOH accelerates the entire reaction rate, which results in shortening the reaction time relative to the reaction with ethylene glycol. At high temperature, PDOH reduces silver ions into silver metal. During the nucleation and the growth of silver metal, PVP suppresses growth along the <100> directions. Nanocubes are formed as a result of this growth. Reproducing the process described in Tao's paper is challenging. We changed the concentration of precursors and the temperature of the reaction with broad ranges to find the optimal conditions for the selective synthesis of AgNCs. Over 200 attempts were unsuccessful. At best, a few attempts resulted in less than 10% AgNC content. This problem was solved after focusing on the preheating time of PDOH. In Tao's procedure, the PDOH was preheated for 10min. PDOH acts as a reducing agent at high temperature. PDOH is oxidized also during the preheating period (no Ag^+ presence). Xia's group reported that aldehyde and carboxyl acid would be generated.[28] The reducing power of the PDOH solvent would therefore change with

preheating. We carried out the synthesis with different preheating times, from 1min to 10min. We found out there was the optimum preheating time and that each batch/bottle of PDOH has a different optimal preheating time. Each time we started to use a new bottle of PDOH, we needed to determine first its optimum preheating time. Figure 2.2 shows the dependence of the shape of the silver nanoparticles in the product on the preheating time.

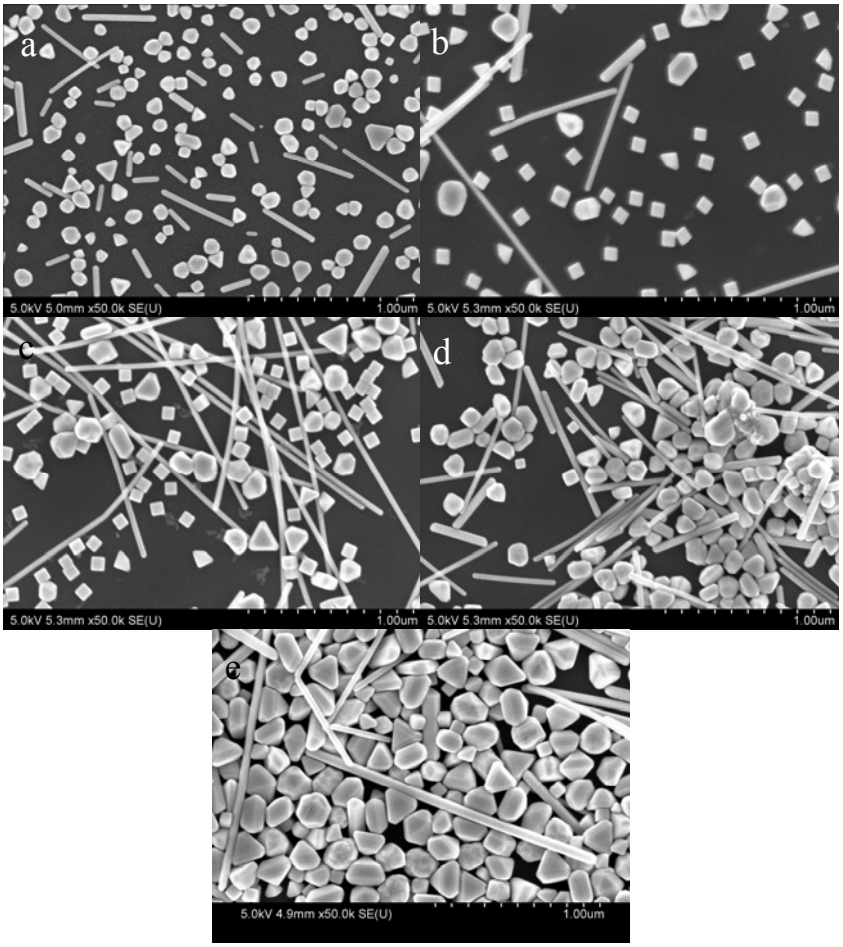

Figure 2.2. Microstructure of the products with different preheating time. (a) 1min, (b) 2min, (c) 4min, (d) 5min, and (e) 10+2min.

The preheating time controls two parameters. One is the reducing power of the PDOH mentioned above. The other is the temperature of the reaction solution. Figure 2.3 shows the change of temperature after immersing the reaction flask in a 190^{o}C oil

bath. The temperature of the reaction solution is 20°C before preheating. Note that the temperature of the reaction solution in the flask is 150°C with 2min preheating and 190°C with 10min preheating. To confirm that the dominant factor of the cube formation is the reducing power, not the temperature, we carried out 2 reactions: A. preheated for 2min, B. preheated for 10min, cooled down & preheated for another 2min. In both experiments, the temperature was the same, but the reducing power was not. Reaction B resulted in non-cubic shape of Ag nanoparticles (Figure 2.2e). Fewer cubes were seen in the product compared to Reaction A (Figure 2.2b). The non-cubic shape particle formation was caused by the difference of the reducing power. This result proves that the reducing power of PDOH is the important parameter of AgNC synthesis.

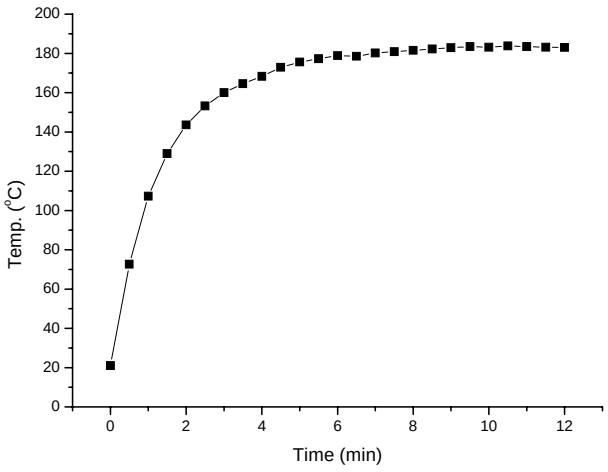

Figure 2.3. Temperature change of PDOH with time.

The optimal procedure for AgNC synthesis is summarized here: 0.1g silver nitrate and 0.12mg copper were dissolved in 5mL 1,5-pentanediol in a glass vial. It was ultra-sonicated for 30min at 35°C to enhance the dissolution. 0.2g PVP

(M_w=55K) was dissolved in 10mL 1,5-pentanediol in another glass vial by magnetic stirring. 5mL of 1,5-pentanediol in a flask were heated in a silicon oil bath at 190^{o}C for 2min. The two precursor solutions were injected into the preheated reaction solution at different rates: 0.125mL of the silver precursor every 60sec and 0.08mL of the PVP precursor every 30sec. The first injection of the PVP precursor was carried out 3sec after the first injection of the silver precursor. The injections were stopped after 8 injections of silver precursor to get the 100nm-long AgNCs.

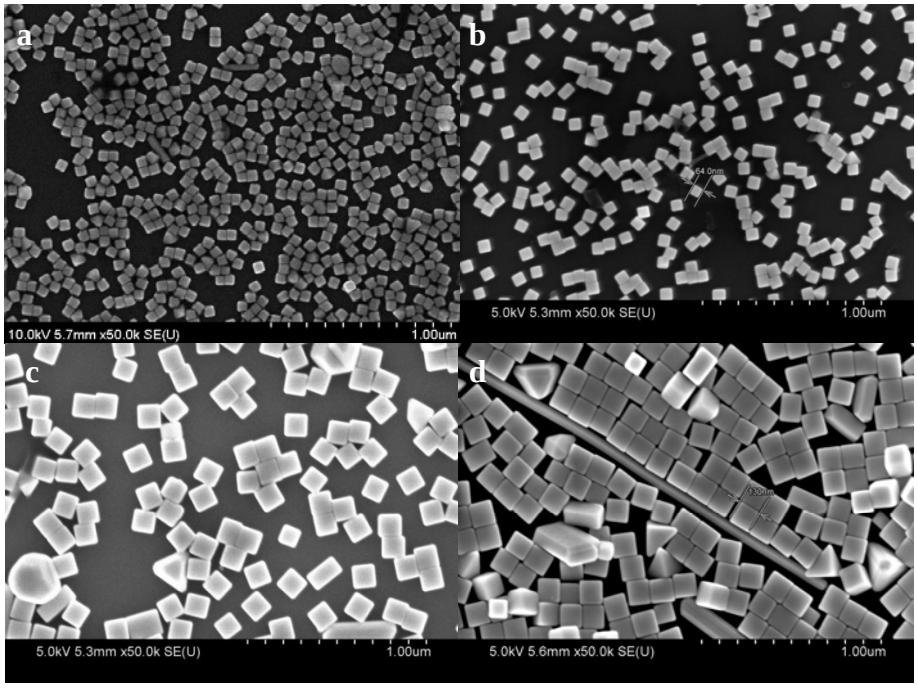

Figure 2.4. SEM images of AgNCs. (a) 50nm AgNCs, (b) 65nm AgNCs, (c) 100nm AgNCs, and (d) 130nm edged-AgNCs.

We could control the size of AgNCs by changing the amount of precursor injected. As more precursor was injected, the size of nanocubes increases (Figure 2.4). AgNCs with the edge length from 50nm to 130nm were prepared. UV-vis spectroscopy was used for the characterization of AgNC colloidal solutions. As

shown in Figure 2.5, the characteristic extinction peaks are red-shifted for the larger AgNCs.

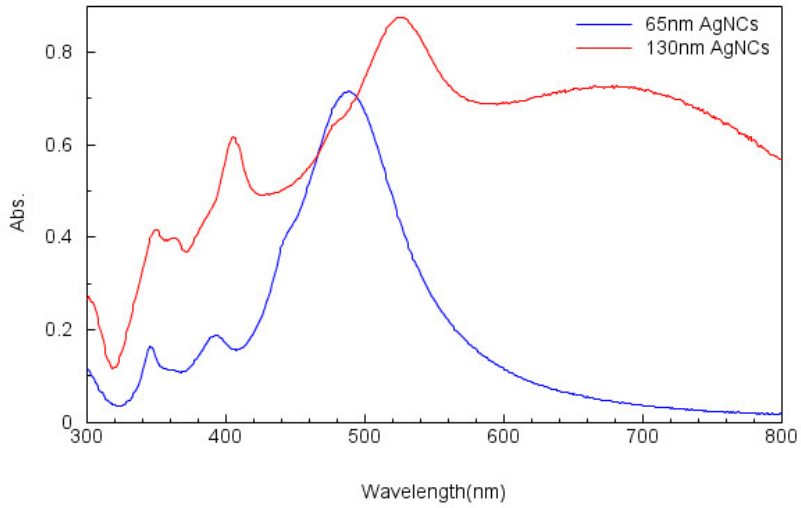

Figure 2.5. UV-vis absorption spectra of (blue) 65nm AgNCs and (red) 130nm AgNCs.

2.3 Optimization of Preheating Time

The optimal preheating time depends on the oxidation state of PDOH. Because the state differs from batch to batch of PDOH, the preheating time must be optimized for each new PDOH bottle.

For the optimization of the preheating time, a flask containing PDOH is immersed in the oil bath for 1min and silver precursor is injected in the flask. The color of the solution is monitored for a change to yellow. The optimized preheating time should be close to the time of the color change. If the color changes at *t* sec after the injection, we typically test preheating times from *t*+40 sec to *t*+70 sec. The optimal preheating time has been found to fall in a range of 90 ~ 200 sec. Once the preheating time is optimized, the cube size can be controlled by the number of

injections of silver precursor as described in Section 2.2, *e.g.* 4 injections of the silver precursor resulted in 80nm-AgNCs, 6 injections resulted in 110nm-AgNCs and so on.

One new batch of PDOH showed a very different behavior. After the injection of silver precursor at 1 min, the color of the reactant did not turn yellow even after 10min of additional heating. We inferred that the PDOH must be oxidized more than the others. As a consequence, the PDOH must lose the reducing power. For this PDOH, we continued to inject the silver precursor once a minute from 5min to 9min. The second injection at 5min caused the color to change to yellow. We obtained 110nm-AgNCs with this procedure. The size of cubes could be tuned by decreasing the time intervals between the injections, keeping the number of injections constant. For example: the silver precursor was injected at 1:00, 4:55, 5:54, 6:53, 7:52 and 8:51 after immersing the flask in the oil bath, which resulted in 80nm-AgNCs.

2.4 Size Dependence of Plasmon Resonance

Extinction spectra were obtained for various sizes of AgNCs dispersed in deionized (DI) water. The longest-wavelength peak was tracked, and plotted as a function of cube size (Figure 2.6). The plot shows a strong dependence of the peak position of the longest wavelength plasmon resonance on the size of cubes. The wavelength of the plasmon resonance peak can be used to "measure" the size of the cubes without electron microscope observation.

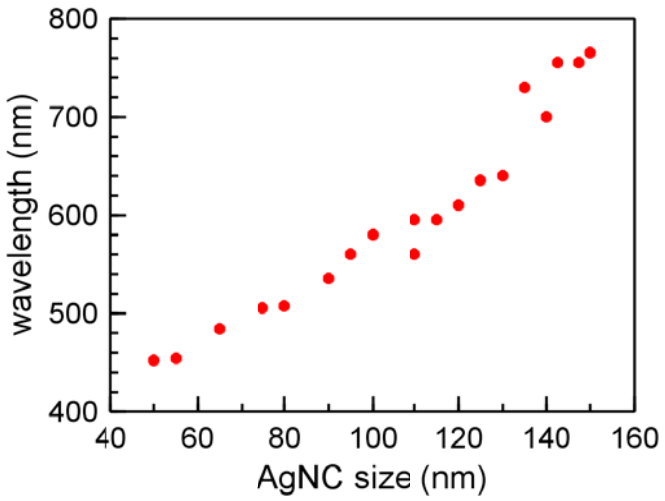

Figure 2.6. Longest-wavelength plasmon resonances as a function of silver nanocube size in water.

2.5 Conclusions

We can control the nucleation of silver in the polyol process and synthesize AgNCs in various sizes. The size of AgNCs can be easily controlled from 50nm to 130nm by changing the amount of the injected precursors or the periodicity of the injections. The state of PDOH is very critical for successful AgNC synthesis. The preheating time should be optimized for each bottle of PDOH, since the oxidation state is different from bottle to bottle.

The extinction spectra of AgNC aqueous solution can provide information of the size of AgNCs. The wavelength of the plasmon resonance peak can be used as an indicator of the size of cubes.

3 Surface-Enhanced Raman Scattering (SERS) on Silver Nanocubes by Vertical Deposition

3.1 Introduction

3.1.1 SERS with Silver Nanocubes (AgNCs)

Following the first appearance of AgNCs in 2002 (Figure 3.1a),[25] studies utilizing AgNCs for SERS applications have been performed.[24, 29-32] [2-6] In one of these efforts, the SERS enhancement of single AgNCs was measured with different orientation of the laser polarization direction (Figure 3.1b).[29] A single cube showed SERS enhancement dependence on the relative angle to the laser polarization direction, while truncated cubes did not show this dependence as depicted in Figure 3.1b. When the laser polarization was parallel to a face diagonal of a cube, SERS enhancement was higher than when it was not parallel (Figure 3.1b). SERS enhancement with a single AgNC was compared to that of a single silver nanosphere (AgNS) by Rycenga *et al*.[24] SERS enhancement by a single AgNC was higher than that of a single AgNS by a factor of 10^3. Sharp nanoscale features on the surface provide a greater SERS enhancement and this conclusion was confirmed by numerical calculation. The effort to look for hot-spots with silver nanocubes generating huge enhancement led Camargo *et al.* to investigate the junction between one AgNC and one Ag nanowire (NW).[30]SERS was enhanced by clustering of the two objects and the enhancement was dependent on relative orientations of the AgNC as shown in Figure 3.1c. Considering that the increase of SERS enhancement by the junction between a AgNC and a AgNW was at most by factor of 5, this clustering

was not so powerful in enhancement. The laser wavelength (λ=515nm) might be far from the plasmon resonance of the cluster.

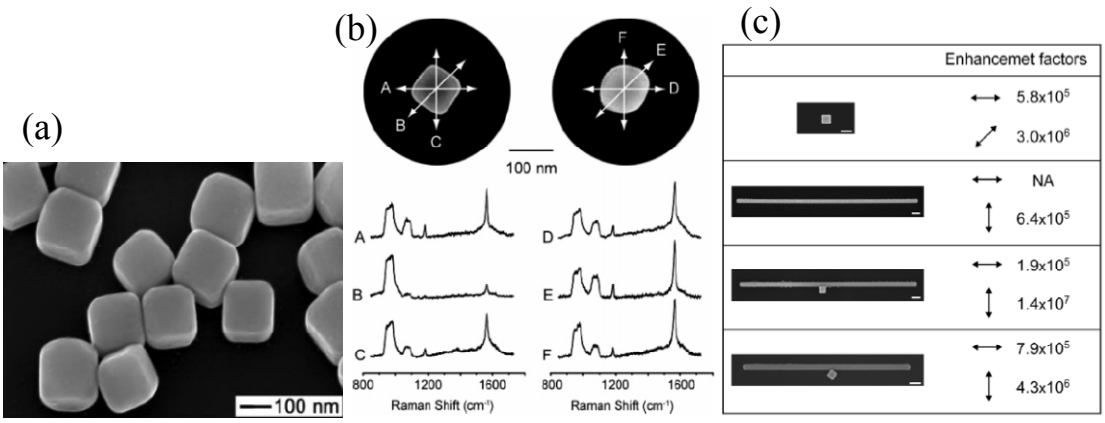

Figure 3.1. (a) A SEM image of silver nanocubes,[25] (b) SERS signal dependence on laser polarization direction, where A, B, C, D, E, and F indicate the direction of the laser polarization and corresponding SERS spectra.[29] (c) Enhancement factors with different configuration of a AgNC and a AgNW.[30]

In 2010, SERS signals from AgNC dimers were reported.[31] Three types of AgNC dimers were investigated by Xia's group as shown in Figure 3.2: 1. face-to-face (FF), 2. face-to-edge (FE) and 3. edge-to-edge (EE). They reported that SERS enhancement was the highest with a FF dimer and the lowest with an EE dimer. They concluded that the FF dimer showed the highest enhancement because FF dimers had the largest junction area. This research was the first work sorting dimers into three categories, though they presented data from only one dimer for each category.

Recently, Rycenga *et al.* demonstrated that hot-spot form between a AgNC monomer and a substrate (bottom gap).[32] They tested different substrates such as glass, silicon, silver, and gold to see the hot-spot formation. By removing all the molecules from the surfaces of the AgNCs except the molecules on the bottom face, the contribution of the molecules on the bottom face to SERS enhancement could be estimated. With metallic substrates (Ag or Au), the gap between the bottom face of a

AgNC and the substrate is a very important hot-spot where most of the enhancement is generated. When non-metallic substrates were used, the enhancement by the gap between the bottom face and the substrate is weak.

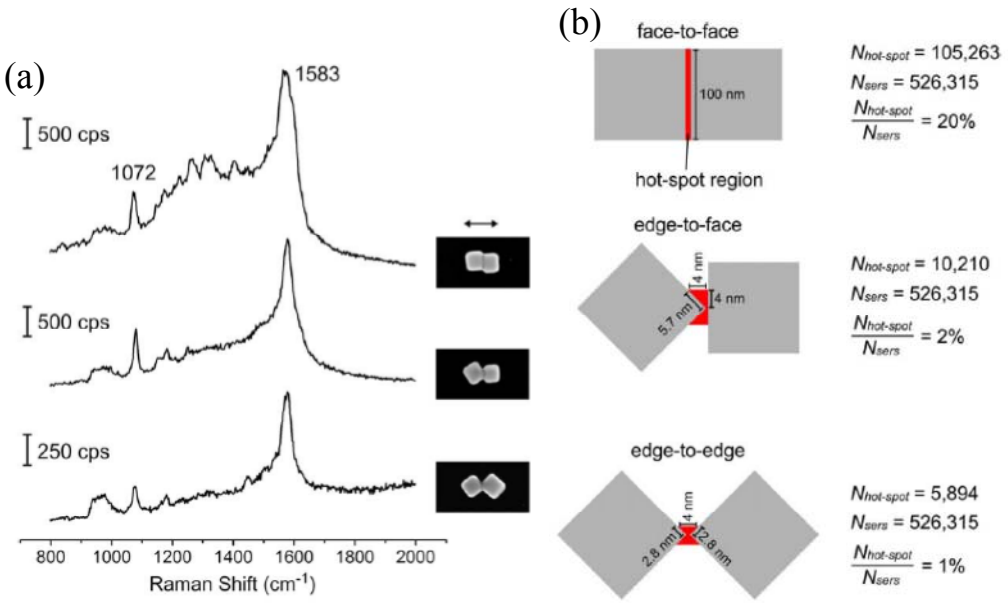

Figure 3.2. (a) SERS spectra with different AgNC dimer configuration. The face-to-face dimer shows the most intense SERS signal. (Edge length of cube ~ 100nm) (b) Calculation of the portion of molecules located where the gap is less than 4nm in the three different configurations.[31]

Most research groups working on SERS based on metal clusters utilize the drop-cast method to generate clusters.[29, 31, 33, 34] The drawback of the drop-cast method is the unpredictability of the position of the clusters on the substrate. Finding clusters for SERS measurement is time consuming. It is therefore not an adequate method for collecting a large number of SERS signals efficiently.

3.2 Design of Experiment

3.2.1 Clustering and Position

'Cluster' is an important keyword in SERS substrate design as discussed in Chapter 1. Single molecule detection was demonstrated with SERS in small particle clusters.[35] Hot-spots showing huge SERS enhancement occur at junctions between metal nanoparticles due to coupling between plasmons. Many researchers agree that the junctions play an important role in SERS enhancement. If we generate a lot of clusters with different configurations, we can correlate the configurations of the AgNC clusters to SERS enhancement. Our goal is to determine the optimized configuration of the AgNC clusters for SERS.

The complexity of the AgNC cluster system increases significantly with the number of cubes in the cluster. Even when confined to a flat substrate, the parameters needed to describe the cluster geometry, such as number of AgNCs (n), gap between pairs of particles (d_{ij}), angle between two particle axis among the cluster and laser polarization direction (θ_{ij}), and rotational angle of a cube (δ_i) (Scheme 3.1), construct a high dimensional space to investigate. (It is assumed that all the AgNCs contact the substrate through a faces; not an edge or a corner.) Even in the case of the simplest cluster, a dimer (n=2), three parameters d, θ, and δ are necessary to describe the cluster. We need to explore a 3-dimesional space to determine the correlation between the SERS enhancement and the three structural parameters, and find the optimal dimer configuration. The possible configurations of trimers (n=3) and tetramers (n=4) are innumerable. To accomplish our goals a new method is needed

for the fabrication and SERS characterization of a large number of AgNC clusters in an efficient manner.

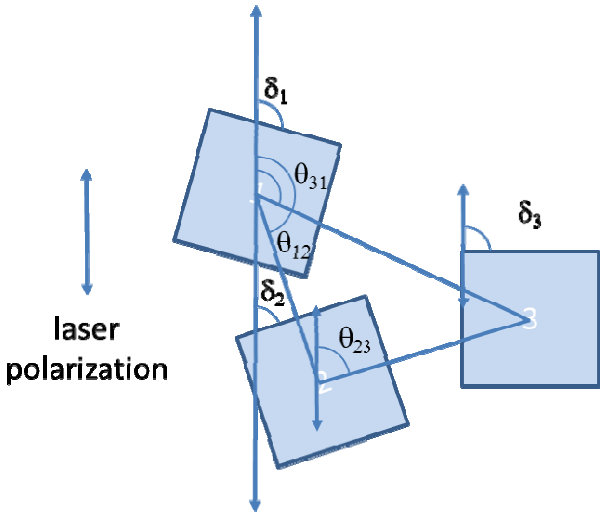

Scheme 3.1. A diagram describing a 3-cube cluster.

Here are the criteria for the new method: The method should be efficient in measuring SERS signals from many clusters. The method should generate a large number of clusters on a substrate that could be characterized automatically by the SERS instrument (*i.e.* clusters ordered in a square array). Sufficient separation between clusters is needed for discerning SERS signal from each cluster. The configuration of each cluster should be different so that we can explore the effect of the various structural parameters (n, d_{ij}, δ_i and θ_{ij}). Practically, it is not possible for us to investigate all the parameters. For convenience sake, the study will focus on clusters with a fixed n value. Therefore, the method is designed to allow us to control the parameter n during for fabrication of the clusters.

3.2.2 New Design for massive Raman Measurement

To measure SERS signals from a large number of AgNC clusters and build a database, we need to design a new method which enables us to utilize the automated mapping function of the microRaman instrument. The requirements are:

- Clusters are formed in a periodic array.
- Clusters are apart from each other to prevent interferences of signals from neighboring clusters.

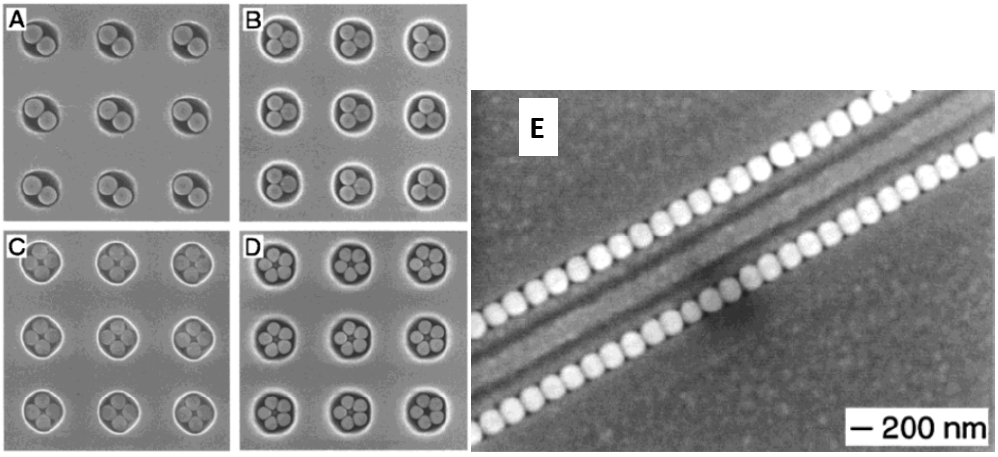

Figure 3.3. SEM images of aligned particles in the patterns. The pores were formed in a photo-resist layer, V-grooves was formed by anisotropic etch of Si(100) wafer. (A-D) 2um-diameter polystyrene spheres in pores, (E) 150nm-diameter silica sphere in V-grooves.[36]

To realize these requirements, we decided to guide the formation of AgNC clusters at patterned positions by utilizing capillary force, so called, 'directed self-assembly' process. Clustering of micro-sized spheres was already demonstrated by Xia's group (Figure 3.3).[36] As shown in Figure 3.3, 2um-diameter polystylene spheres were trapped in pores, forming identical clusters in the pores. Since the effect of Brownian motion exceeds the effect of capillary force at small particle size,

identical clusters of nanoparticles could not be formed in cylindrical pores. Linear arrays of 150nm-diameter silica sphere were formed in V-grooves.

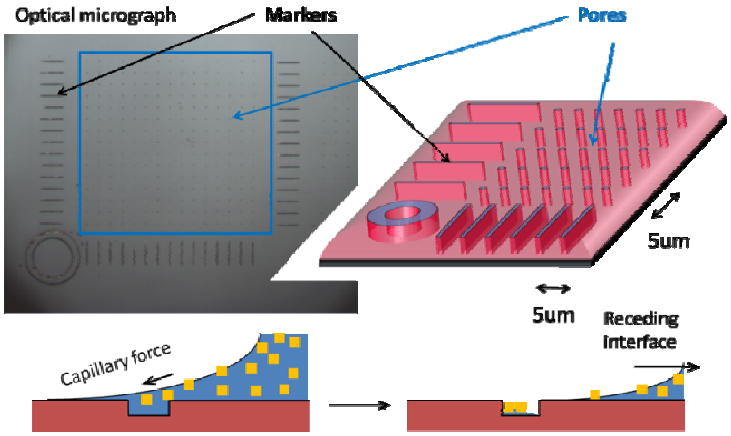

Figure 3.4. Schematic diagrams of the deposition process. The receding interface leaves silver nanocubes in the pores.

This process can be applied for our purpose. We expected to form AgNC clusters with various configurations due to the decrease of the capillary force effectiveness for our particle sizes. We trapped the AgNCs in the same way. Cavities were formed at pre-determined positions in a silicon substrate. As depicted in Figure 3.4, during the dewetting of the substrate (by evaporation or by mechanical translation), the interface between air and the colloidal solution swepts across the substrates. The capillary force at the rear edge of the meniscus drags the AgNCs into the cavities. Once the AgNCs are trapped in the cavities, we can remove excess AgNCs on the top surface without affecting the AgNCs in the cavities. In this way, we can generate AgNC clusters selectively at pre-determined positions. To prevent interference from adjacent pores, we need to pattern the array with sufficient pore separation. The number of particles in a cluster can be controlled by changing the

diameter of the pore. The cylindrical pore shape enables us to generate various configurations of clusters.

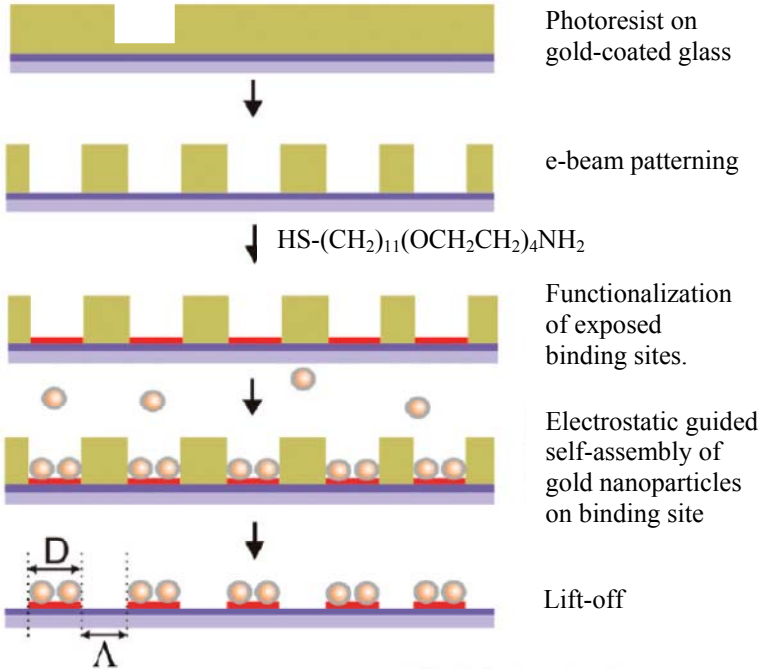

Figure 3.5. Schematic diagram of gold nanoparticle clustering using chemical patterning. The selected area was functionalized by thiol-$(CH_2)_{11}EG_7$-amine and positively charged. The electrostatic force facilitated the deposition of the negatively charged gold nanospheres. D(binding site diameter) and Λ(cluster edge-to-edge separation) were controlled.[37]

An alternative way to form arrays of cluster is using chemical patterning. The formation of pores is replaced by the patterned functionalization of the surface of the substrate. The functionalized area will trap or repulse the metal nanoparticles. In one example of the method, Yan *et al.* functionalized a metal film and utilized electrostatic forces for the deposition of Au nanoparticles as depicted in Figure 3.5.[37] This substrate contains nanoscale gaps not only between nanoparticles but also between nanoparticles and a metal layer on the substrate. The vertical deposition method is superior to methods based on chemical patterning because it is simple and recyclable. After measuring SERS signals of molecules, AgNCs can be easily

removed by an acid wash. Another set of AgNC clusters can be formed readily on the same substrate, since the patterns etched by nanolithography in the silicon substrate are intact after the acid treatment.

In this chapter, we demonstrated the formation of AgNC clusters at pre-determined positions using the vertical deposition technique and analyzed the SERS response of different dimer configurations. This work led to the determination of a desirable configuration for high and reproducible SERS enhancement.

3.3 Formation of AgNC Dimers

3.3.1 E-Beam Lithography and Directed Self-Assembly

An array of pores was formed by conventional e-beam lithography. PMMA resist (950PMMA A4, Microchem) was spin-coated on a silicon wafer (4K RPM, 45sec, thickness 200nm) and dried (180^{o}C, 1min). Patterns containing pores and alignment markers were drawn using the e-beam writer (e_LiNE, Raith). After writing, the film was developed by stirring in the developing agent solution (MIBK:IPA=1:3,1.5min) and cleaned by rinsing with DI water. The pattern in the PMMA film was transferred to the underlying silicon substrate by reactive ion etching (RIE). The etch rate was 10 nm/sec (100W, 50mTorr under flow of 50sccm SF_6 and 10sccm O_2). The wafer was cleaned by rinsing with acetone, aqua-regia, and O_2 plasma treatment (50W, 50mTorr, 50sccm O_2).

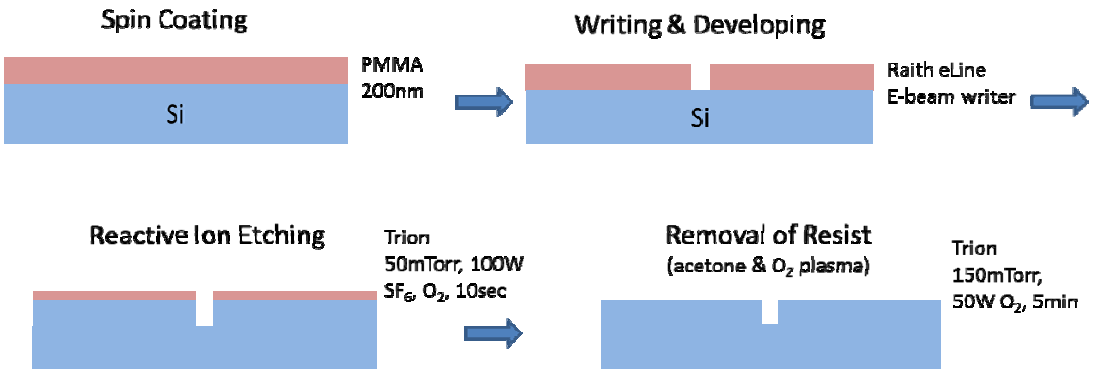

Scheme 3.2. Schematic diagram describing procedures of the substrate preparation.

AgNCs were deposited on the patterned substrates. For the deposition, the AgNC colloidal solution was diluted 15 times with EtOH, cleaned several times with EtOH, followed by changing the solvent into deionized water. The patterned substrate was immersed in the aqueous solution of AgNCs and slowly pulled out upward by means of a motorized stage.

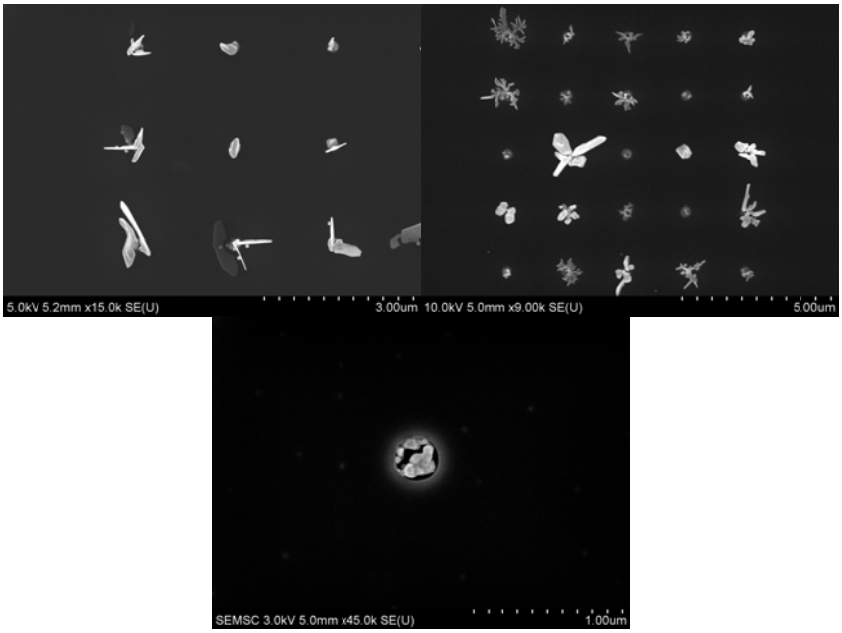

Figure 3.6. Irregular silver growth along the edge of pores.

In early experiments, unintended growth of silver at the edges of the pores was observed after the deposition process (Figure 3.6). The unintended silver growth prevented the formation of well-defined AgNC clusters in the pores. Further investigation revealed the formation mechanism of the irregular structures. The details of the irregular growth mechanism will be discussed in Chapter 6. The irregular growth was suppressed by cleaning the patterned substrate with aqua-regia and successive oxygen plasma treatment.

When we started this research, AgNC colloidal solutions in EtOH were used for the deposition of AgNC on the substrate. The substrate was placed vertically in an open vial and the EtOH was allowed to evaporate overnight. The meniscus along the interface of air and solution recedes as the EtOH was evaporated. After the air/solution interface swept across the surface of the substrate, AgNCs were left behind on the substrate. The deposition using EtOH solution resulted in large deviation in the fraction of pores containing cubes between 20% and 80%. The reason of the deviation is that the natural evaporation of EtOH was utilized without controlling the evaporation rate. The EtOH evaporation method has additional drawbacks: (1) Slowing down the evaporation rate is not easy. (2) The concentration of AgNCs in the solution increases during the evaporation. For these reasons, we decided to use water as the solvent. Using colloidal solutions in water and a motorized stage, the sweeping speed of the interface was controlled. The amount of water evaporating during the deposition is negligible. We carried out a study varying the pull-out speed. Table 3.1 shows the effect of the pull-out speed on the filling efficiency. Filling efficiency was defined as a portion of pores contain at least one

AgNC. The deposition with the highest pull-out speed resulted in 100% empty pores. As the pull-out speed decreases, the filling efficiency reaches a maximum, 87%, at 0.63mm/hr and decreases again to 44% at 0.16mm/hr. As shown in Table 3.1, the pull-out speed yielding the highest filling efficiency was 0.63mm/hr. However, the formation of monomers contributed a lot to the highest filling efficiency of the deposition with 0.63mm/hr. For the formation of large clusters such as dimers, trimers and so on, 0.31mm/hr pull-out speed was adopted.

Table 3.1. The distribution of clusters by number and its dependence on pull-out speed [as % of total number of pores].

	0.16mm/hr	0.31mm/hr	0.63mm/hr	1.25mm/hr	2.5mm/hr
Empty	56	22	13	74	100
1particle	10	26	65	25	0
2particles	5	25	20	1	0
3particles	5	14	2	0	0
4particles	2	9	0	0	0
5+particles	22	3	0	0	0

3.3.2 SERS on AgNC Dimers

With the directed self-assembly method, we formed hundreds of clusters. To measure the effect of the configuration on the SERS enhancement, we needed to form a self-assembled monolayer of reporter molecules (4-aminothiophenol) on the surface

of the AgNCs in the pores. After the formation of clusters in pores, the substrate was immersed in a 0.2mM 4-aminothiophenol (ATP) solution in ethanol for 3 hours, rinsed extensively with ethanol, and dried under nitrogen.

SERS spectra were measured with a Horiba Jobin-Yvon LabRAM HR-VIS microRaman spectrometer equipped with a 632.8 nm laser source, a confocal microscope, and an x-y scanning stage. A 50x objective (numerical aperture NA = 0.5) was used for signal collection. SERS spectra were acquired with incident laser power of 0.6mW and acquisition time of 4sec. Images of the pores were recorded by SEM (Hitachi, SU-70) immediately after the Raman measurement.

The Raman signal intensity is quantified as the integrated peak area for the carbon-sulfur bond stretch of ATP at 1078 cm^{-1} in each spectrum. Using the same spectrometer settings, the reference Raman spectrum of a 1M ATP solution in 1,5-pentanediol was measured, and the Raman signal intensity per molecule was calculated assuming a cylindrical focal volume with a diameter of 2.2um and a height of 16um. The SERS substrate enhancement factor (EF) is calculated as the Raman signal intensity divided by the number of molecules on the AgNCs and by the Raman signal intensity per molecule of the reference solution. A monolayer of ATP molecules on the six {001} facets of the AgNCs is assumed, with a density of 5 molecules/nm^2.[38]

For this analysis, we collected SERS signals from dimers, since they are the simplest cluster.

First, we focused on the SERS signal dependence on the angle between the dimer axis and the laser polarization direction (θ). A $\cos^2\theta$ dependency of the signal

was already reported by previous researcher.[39, 40] To check the SERS signal anisotropy, we measured SERS spectra of dimers twice with two different laser polarization directions, perpendicular to one another. The SERS signal anisotropy was calculated by Equation 3.1.

$$\text{SERS signal anisotropy} = \frac{A_x - A_y}{max(A_x, A_y)} \qquad (3.1)$$

where A_i is peak area at 1078cm^{-1} of ATP Raman spectra measured with the *i*-direction polarized laser.

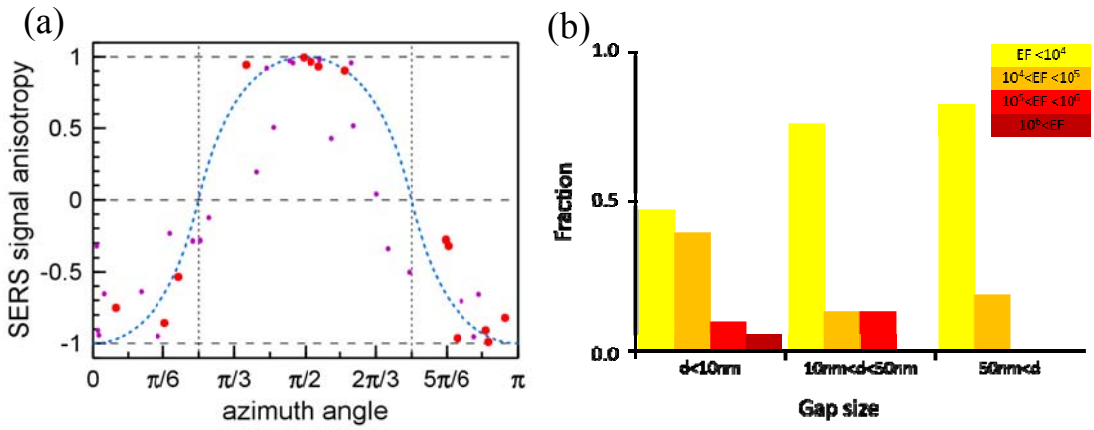

Figure 3.7. (a) SERS signal anisotropy. Red circles are data from dimers with strong SERS enhancement, purple spots from dimers with weak enhancement, and blue dashed line is the simulated curve. (b) Population fraction as a function of SERS enhancement factor with different gap sizes.

Figure 3.7a shows the plot of the SERS signal anisotropy as function of the angle between dimer axis and laser polarization direction. Large red circles indicate the data points from dimers with high enhancement factor (EF >10^5), and small purple circles indicate the data points from dimers with low enhancement factor, and the blue dashed line is drawn under the assumption that signal intensity is proportional to $\cos^2\theta$. Red circles match the blue dashed line very well. The purple circles are spread out farther from the line. The low EF value indicates there is no

good coupling between the particles. They may act more like two individual AgNCs than a dimer. If the interaction between the particles is weak, the polarization direction has a lesser effect on the SERS signal.

We investigated the effect of the gap size on the enhancement factor. The study was limited by the fact that the number of dimers with wide gap was low. Only 30 out of 238 dimers had a gap larger than 10nm. Figure 3.7b shows the distribution of EF values with different gap sizes. 15% of the dimer with gap less than 10nm have an enhancement value larger than 10^5, while only one out of 30 dimers with gap more than 10nm has an enhancement value larger than 10^5. The necessary condition to achieve high enhancement factors is that the gap should be less than 10nm.

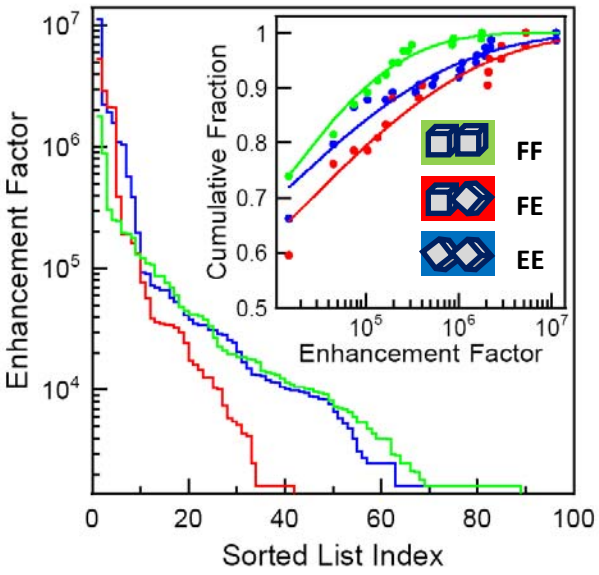

Figure 3.8. SERS substrate enhancement factors for EE dimers (blue), FE dimers (red) and FF dimers (green). Inset: Experimental cumulative fractions and fit to the Weibull distribution model.(Solid circles: experimental data. Solid lines: fit values.)

We collected more than 200 SERS spectra from AgNC dimers with gap size less than 10nm. All the dimers were sorted into 3 categories according to their configuration, *i.e.* Face-to-Face (FF), Face-to-Edge (FE), and Edge-to-Edge (EE).

(The detailed definitions of the categories are available in Appendix 3.A.) All the EF values of each category were arranged in diminishing order and plotted (Figure 3.8). The sorted list index of a dimer indicates its position in the list of diminishing EF values. A sorted list index of 1 corresponds to the dimer with the highest EF value, an index of 2 corresponds to the dimer with the second highest EF value, and so on. From the plot, it is difficult to see a significant difference between the EFs of the three dimer types, since each category contains different number of dimers. Cumulative fraction is used for normalization. Plots of cumulative fraction versus EF value of each category clearly show the difference between each category. Cumulative fraction indicates the fraction of population up to certain EF value. For example, if the cumulative fraction is 0.9 at EF of 100000, 90% of dimers have an EF value of 100000 or less. The cumulative fraction of FF type dimers approaches 1 more quickly than those of the other type dimers (inset of Figure 3.8). This indicates more FF type dimers have low EF values than other type dimers.

To quantify the difference, we fit the data to the 2-parameter Weibull distribution function,

$$F_{Weibull}(x) = 1 - \exp\left\{-\left(\frac{x}{b}\right)^{c}\right\} \qquad (3.2)$$

where $F_{Weibull}$ is the cumulative fraction, x is the enhancement factor value, b is the "scaling parameter" and c is the "shape parameter". The scaling parameter is related to the mean of EF values and the shape parameter is related to the spread of EF values. Analysis based on this model will clearly show difference between different configurations.

To extract the Weibull parameters, we carried out a simple linear regression analysis after taking multiple logarithms: The transformations of $Y = \ln\{-\ln\{1 - F(x)\}\}$ and $X = \ln\{x\}$ and their relation of $Y = c(X - \ln\{b\})$ were used to estimate the values of *b* and *c* of each category (Table 3.2). The results indicate the shape parameters of EE and FE type dimers can be regarded equal. The same shape parameters, *c*, mean the distributions of enhancement factors in EE and FE type dimers have same dispersion. However, the scale parameter, *b*, of FE type dimers is higher than that of EE type dimers by 2 times. It indicates that the mean enhancement factor of FE dimers is larger than that of EE type dimers by 2 times. FF type dimers have a higher shape parameter than the other type dimers, which describes the cumulative fraction of FF type dimers approaches 1 faster than the others. The modeled curve of each type of dimer in the inset of Figure 3.8 matches well with the experimental results. This statistical analysis reveals that the FE type is more desirable configuration for SERS than other types. The notion of desirable configuration is distinct from the configuration with the highest EF. The FE type dimers showed higher and more reproducible EF value, though the highest EF value was recorded from an EE type dimer. Since to date no lithography technique can provide highly precise control in nanometer scale, deviation in gap size is inevitable. Thus, forming FE type dimers can guarantee stably high EF values.

Calculations by Prof. Mayergoyz's group also support our analysis of the experimental results. Plasmon resonance frequencies and the surface charge distributions were calculated for each type of dimers. The EF values of each type of dimer were estimated with different gap sizes. Table 3.3 shows the dependence of the

resonance wavelength and SERS EF on the gap distance for each type of dimer. FF dimers are very sensitive to the gap distance, which agrees with the fact that the shape parameter of FF dimers is higher. The calculation results indicate that FE dimers are desirable for high SERS enhancement.

Table 3.2. Parameters obtained from the Weibull distribution model.

	EE dimers	FE dimers	FF dimers
shape parameter (*c*)	0.196 ± 0.014	0.205 ± 0.017	0.284 ± 0.021
scale parameter (*b*)	4483 ± 613	10812 ± 1510	5237 ± 683

Table 3.3. Theoretical resonance wavelengths and SERS enhancement factors for 80nm AgNC dimers on silicon calculated by Prof. Mayergoyz's group.

gap distance (nm)	**FF**		**FE**		**EE**	
	resonance wavelength (nm)	SERS EF*	resonance wavelength (nm)	SERS EF*	resonance wavelength (nm)	SERS EF*
3.0	604.63	6.77E+06	577.48	1.19E+06	569.03	6.95E+05
3.5	595.61	1.63E+06	573.58	6.87E+05	567.12	5.01E+05
4.0	589.08	7.71E+05	570.52	4.43E+05	565.35	3.77E+05
4.5	583.73	4.80E+05	568.03	3.10E+05	563.74	2.96E+05
5.0	578.43	3.49E+05	565.95	2.32E+05	562.27	2.40E+05
5.5	573.13	2.75E+05	564.19	1.82E+05	560.95	2.00E+05
6.0	567.78	2.18E+05	562.67	1.49E+05	559.74	1.71E+05
6.5	562.18	1.59E+05	561.34	1.26E+05	558.64	1.48E+05
7.0	556.32	1.02E+05	560.17	1.09E+05	557.63	1.31E+05
7.5	550.38	5.82E+04	559.12	9.62E+04	556.71	1.18E+05
8.0	544.74	3.21E+04	558.17	8.64E+04	555.87	1.07E+05
8.5	539.46	1.79E+04	557.32	7.85E+04	555.08	9.78E+04
9.0	534.54	1.04E+04	556.53	7.22E+04	554.36	9.04E+04
9.5	530.00	6.19E+03	555.82	6.70E+04	553.69	8.42E+04
10.0	525.79	4.07E+03	555.16	6.27E+04	553.07	7.89E+04

* EF values are estimated with incident wavelength of 633nm and scattered wavelength of 678nm.

3.4 Formation of AgNC Trimers and Tetramers

3.4.1 Expected Advantage of AgNC Trimers and Tetramers

Our results in Section 3.4 show that the laser polarization direction should be aligned along the dimer direction to maximize the enhancement. To explore trimer and tetramer system, we need to reduce the number of structural parameters described in Section 3.2.1. Thus, all the clusters will be aligned in the direction of the laser polarization. This alignment will be achieved by changing the pore shape: Aligned cluster will be formed in rectangular cavities instead of circular ones. Trimers or tetramers of AgNCs are expected to have their plasmon resonance at a long wavelength around 785nm which is the longest wavelength of laser we have available. As the wavelength increases in the visible and the infrared light range, the absolute value of the ratio of $\varepsilon_1/\varepsilon_2$ increases as shown in Figure 3.9, which results in an increase of the cross section in Equation 1.1. We expect that the longer wavelength laser will result in a higher EF.

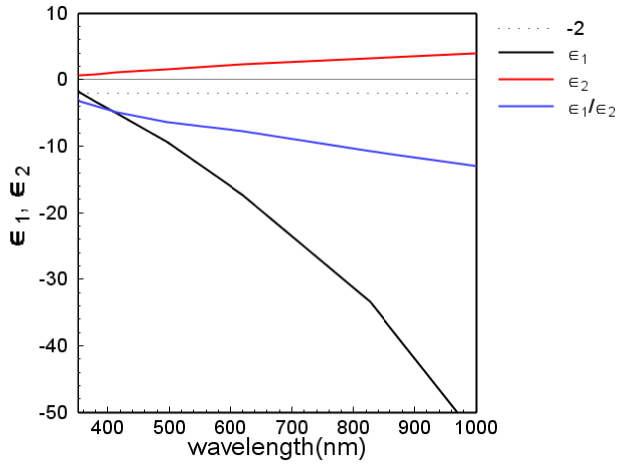

Figure 3.9. The complex dielectric function of silver. The absolute value of the ratio of $\varepsilon_1/\varepsilon_2$ (blue line) increases with the wavelength.

3.4.2 Vertical Deposition for AgNC Trimers and Tetramers

For the formation of AgNC trimers and tetramers, RIE etched silicon substrates were prepared by the same e-beam lithography procedure described in Section 3.1. To align clusters in pores linearly in the direction of the laser polarization, rectangular pores with 150nm width and 350~450nm length were formed in the silicon substrates.

To optimize the conditions of the vertical deposition, we tried pull-out speeds from 0.16 ~ 2.5mm/hr and several solvents such as DI water, butanol, and octanol. Also, we tried two different pull-out directions, parallel and perpendicular to the rectangular width. However, we could not get any consistency of the deposition results in the rectangular pores. Very rarely, trimers and tetramers were formed in the pores. These examples are shown in Figure 3.10. The formation of trimers and tetramers was not reproducible. Moreover, the AgNC clusters in the rectangular pores tended to have large gaps.

Poor reproducibility and large gap formation made us look for alternative deposition methods. These will be dicussed in Chapter 4.

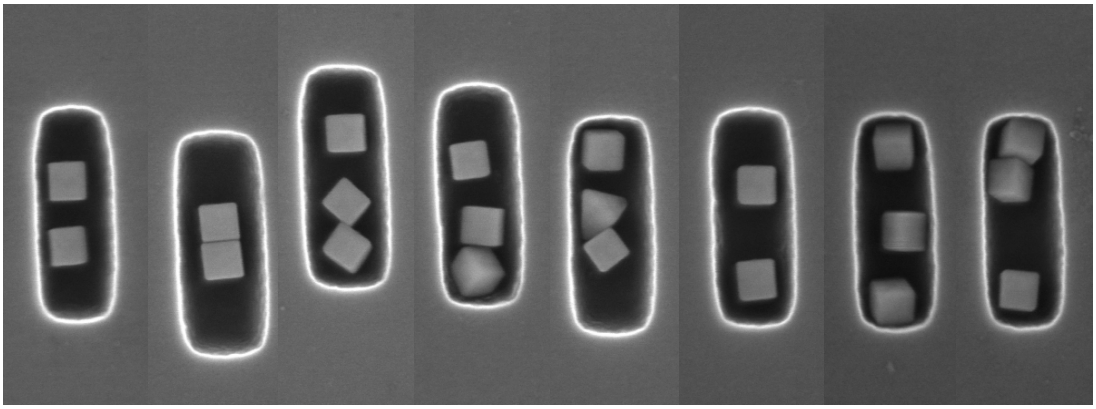

Figure 3.10. SEM images of clusters in the rectangular pores. AgNC size : 85nm

3.5 Conclusions

By trapping the AgNCs in cavities in pre-patterned substrates, AgNC dimers were successfully formed in pre-determined position by vertical deposition. This technique enables us to analyze more than 200 AgNC dimers. We correlated SERS enhancement to various structural parameters of the AgNC dimers. The alignment of the dimer axis with the laser polarization and a small gap size less than 10nm are essential for a large SERS enhancement. Face-to-edge dimers are better for SERS enhancement than face-to-face and edge-to-edge dimers. Face-to-edge configuration is desirable for high and reproducible SERS enhancement.

We could not form aligned AgNC trimers and tetramers by vertical deposition. We need to find alternative ways to form big clusters.

3.6 Supplementary Research – AgNC Clusters on Si_3N_4 Membrane

The numerical calculations for AgNC dimers in Table 3.3 indicates that the plasmon resonance frequency is very sensitive to the gap. Half nanometer change in gap size can have a large effect on EF as shown in Table 3.3. In our experiment with vertical deposition, SEM was used for the characterization of dimer angle, gap size and configuration, since merits of using SEM is the ease in the preparation of substrates. However, SEM does not provide sufficient resolution. Thus, we tried to utilize TEM for high resolution imaging to characterize the geometric configuration of the clusters.

For the TEM observations, substrates should be sufficiently thin, since electron beam need to penetrate the substrates. The patterns were formed in 150nm-thick Si_3N_4 membranes which the electron beam of TEM can penetrate. Because the etch rate of Si_3N_4 is slower than Si, we could not use PMMA layer as mask. Thus, metal mask for RIE is needed. To minimize the e-beam writing time, a negative e-beam resist was used.

A negative e-beam resist (MaN2401, Micro resist technology GmbH) was spin-coated on the Si_3N_4/Si substrate (3K RPM, 60sec), and dried (90^oC, 1min). Patterns were drawn using 30kV acceleration voltage with 7.5μm by the e-beam writer (e_LiNE, Raith). The dose amount of e-beam was 600uC/cm^2. The film was developed by stirring in the developing agent solution (CD-26, Rohm and Haas Electronic Materials LLC) for 4min and cleaned by rinsing with DI water. After the development, 20nm-thick Cr layer was deposited by e-beam evaporation. Lift-off was carried out by sonication in acetone for 1 hour. The pattern in the Cr film was transferred to the underlying Si_3N_4 substrate by reactive ion etching (RIE). The etch rate was 5nm/sec (100W, 100mTorr under flow of 50sccm SF_6 and 10sccm O_2). The wafer was cleaned by rinsing with acetone, aqua-regia, and O_2 plasma treatment (50W, 50mTorr, 50sccm O_2, 150sec). AgNCs were deposited by vertical deposition. The Si_3N_4/Si substrate was mechanically pulled out of a AgNC aqueous solution at a speed of 0.625mm/hr to form AgNC clusters in the pores. The substrate was soaked in 0.5mM ATP ethanoic solution for 3hrs. SERS response was measured using 515nm laser and D0 filter for 60sec.

From the SERS measurement, we found out that monomers on Si_3N_4/Si did not give out any signals of ATP molecules. Figure 3.11a shows a Raman spectrum from a monomer on Si_3N_4. Due to the high laser power, we could see strong peaks from Si_3N_4 and Si at 520cm^{-1} and 900-1000cm^{-1}, respectively. For comparison, monomers were formed on Si and measured under the same conditions. We could see stronger ATP peaks using silicon as substrate. The peak at 1078cm^{-1} of the ATP molecule is comparable in intensity to the peak of bulk (Figure 9b).

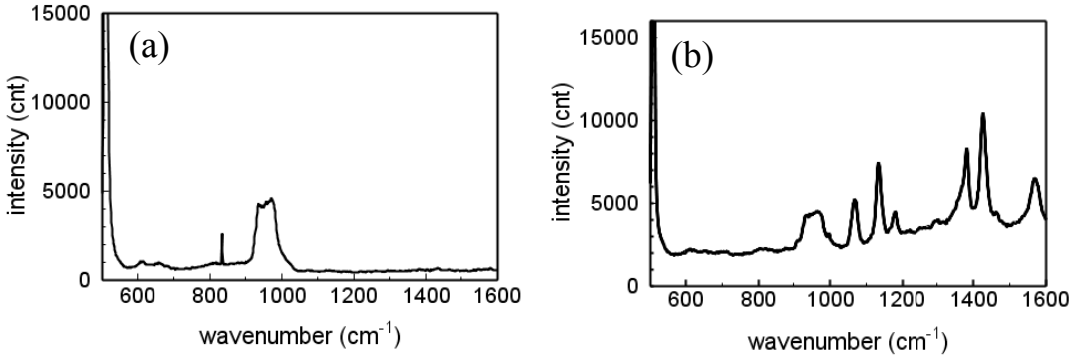

Figure 3.11. Raman spectra obtained by 515nm laser from a monomer (a) on the Si_3N_4 substrate and (b) on the silicon substrate.

The difference in the dielectric constant of the substrates makes a difference in the plasmon resonance frequency. The calculated plasmon resonance frequency (by Prof. Mayergoyz's group) of AgNC monomers on silicon is 533nm and that on glass is 440nm. The plasmon resonance of AgNC monomers on Si_3N_4 is near 440nm, considering that the dielectric constant of Si_3N_4. The plasmon resonance of AgNC monomers on Si_3N_4 is far from 515nm of the laser wavelength.

We concluded that it is useless to continue SERS experiment with Si_3N_4 substrates, since we will need to form larger clusters to tune the plasmon resonance to

the laser wavelength. The SER experiment with Si_3N_4 substrates does not have continuity with SERS response of AgNC dimers.

4 Surface-Enhanced Raman Scattering on Silver Nanocubes with Electrophoretic Deposition

4.1 Introduction

As mentioned at the chapter 3, we could not reproduce the optimum results of the vertical deposition for AgNC trimers and tetramers. We sought for efficient alternative ways. The electrophoretic deposition (EPD) is the most promising approach, because the EPD is a very time-efficient process with high throughput and it is compatible with the e-beam lithography process already used for the vertical deposition.

4.1.1 Electrophoretic Deposition

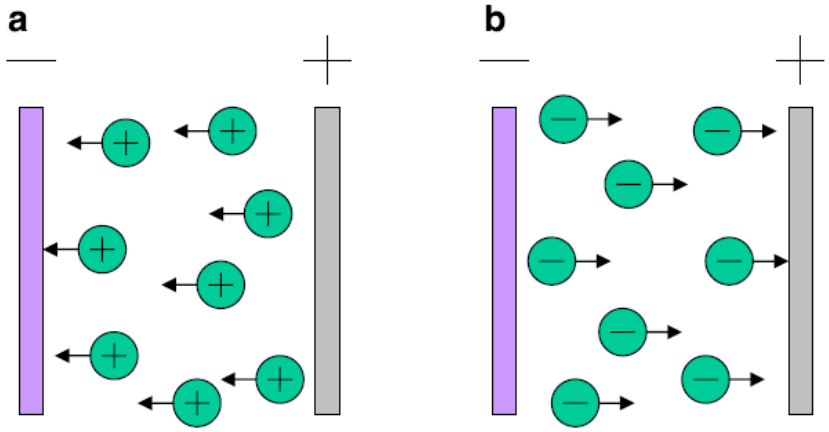

Scheme 4.1. Schematic diagram of electrophoretic deposition. (a) Cathodic EPD and (b) anodic EPD.[41]

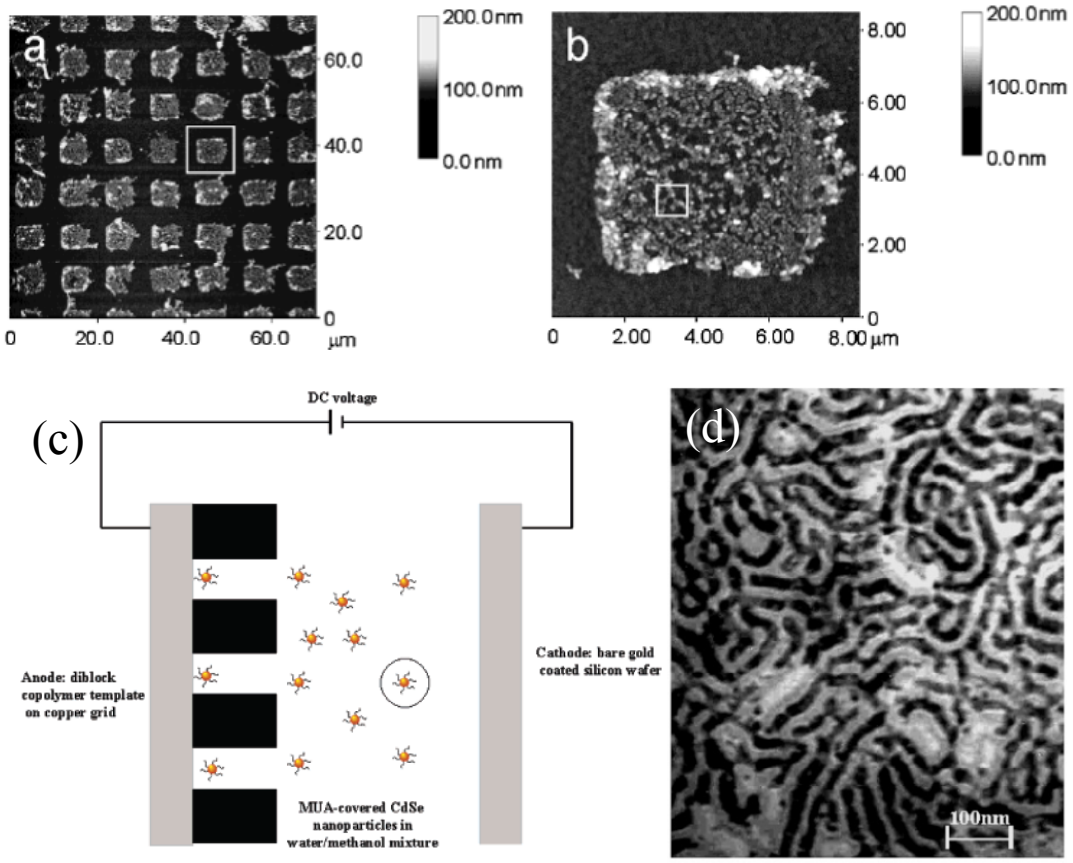

Figure 4.1. (a) AFM height image of a micropatterned gold nanoparticle thin film, (b) AFM height image of the area indicated by the white box in (a). (c) Schematic diagram of the EPD setup used for CdSe deposition into diblock copolymer templates.[42] (d) TEM image. Black worm-like structures are CdSe nanoparticles, while gray worm-like lines are polystyrene template, and bright areas are unfilled space within nanotrenches.[43]

During the EPD process, a DC electric field is applied between two electrodes in a colloidal solution consisting of a liquid medium and particles. Charged particles in a liquid medium are attracted and deposited on a conductive electrode of opposite charge as shown in Scheme 4.1. EPD is one of the colloidal processes commonly used for ceramic production.[41] It has several advantages for ceramic production: short formation time, simple apparatus, and little restriction of the shape of substrate. Minor changes in electrode design enable versatile deposition on various substrates. Moreover, the thickness and morphology of a deposited film can be easily controlled

by adjusting the deposition time and applied potential. The difference between typical EPD and electroplating is that solid particles – not ions – are used, the current level is negligible and liquid medium with low conductance is needed.

Even though EPD is a well-known process in ceramics, not too many applications of EPD for metal nanoparticle have been made. In 1993, Giersig *et al.* demonstrated the formation of ordered monolayer of gold nanoparticles on carbon-coated copper grids by EPD.[44] Bailey *et al.* reported micropatterned thin films of gold nanoparticles in 2000.[42] As shown in Figure 4.1, gold nanoparticles formed an array of square pattern (~5um x5um). This is the first work forming nanoparticle micropatterns utilizing the EPD process as far as I know.

For quantum-dots, Zhang et. al demonstrated CdSe nanoparticles were selectively deposited into nanopores and nanotrenches derived from diblock copolymers.[43]

Scheme 4.2 explains our assembly strategy using an EPD process. Nanometer-sized PMMA patterns as an electrode are immersed in a AgNC colloidal solution. The applied electric field attracts the AgNCs towards the electrode, which results in the deposition of AgNCs. AgNCs which are located on the PMMA layer are removed during the PMMA removal. Consequently, AgNCs should be located at the positions pre-determined by the PMMA patterns.

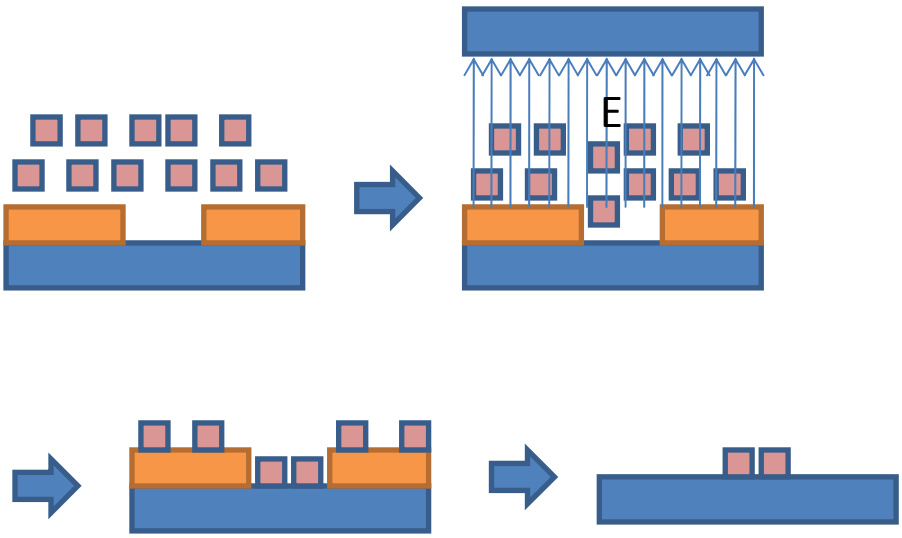

Scheme 4.2. AgNCs (purple squares) in colloidal solution can be pulled by applied electric field. AgNCs can be placed in the pores as well as on the PMMA layer (orange colored layer). After the removal of PMMA, AgNCs remain only in the pores.

It is worthwhile to point out pros and cons of EPD in the context of SERS research.

- The AgNCs are deposited on flat substrates as well as in etched pores by the EPD, while the AgNCs are placed in the etched pores by the vertical deposition. The AgNCs on a flat surface will not generate lateral mirror images.
- The AgNCs on a flat surface are the only scattering center for the incident light due to the absence of the etched pore. This fact enables us not only to recognize the AgNCs with optical microscope, but also obtain the dark field spectra from the AgNCs.
- The electrostatic force exerted on the AgNCs in the EPD is more efficient and easier to control than the capillary force in the vertical deposition. The result is a high throughput.

- On the other hand, in EPD we cannot recycle the patterned substrate like the etched substrate for the vertical deposition. More time is spent in preparing patterned substrates by e-beam writing process.

4.2 Preliminary Experiment of EPD Process

To check the feasibility of the EPD with AgNCs, preliminary experiments were carried out with pieces of bare silicon without patterning. The AgNC solution was cleaned by centrifugation at 8K RPM for 5min with ethanol 4 times and DI water 2 times. The final aqueous solution was diluted by 7.5 times from the original concentration (to approx. 2mM concentration of the Ag atoms). PMMA cuvettes (VWR Cat# 97000-590) were cut into a dimension of 10mm x 10mm x 15mm and used as the vessel for EPD. Two pieces of silicon wafer with 10mm x 30mm dimension were used as anode and cathode. The electric potential was applied by a DC power supply (E3612A, Agilent). We carried out the EPD with different potentials and durations. We noticed that the AgNCs were attracted to the anode, *i.e.* they are negatively charged in the water. Figure 4.2 shows SEM images of anodes following EPD with different applied voltages. For the same duration (1min) higher voltages resulted in denser deposition of AgNCs (Figure 4.2). The coverage of AgNCs on a flat silicon substrate increased with EPD time (Figure 4.3). The applied voltage and the deposition time are important factors controlling the AgNC deposition.

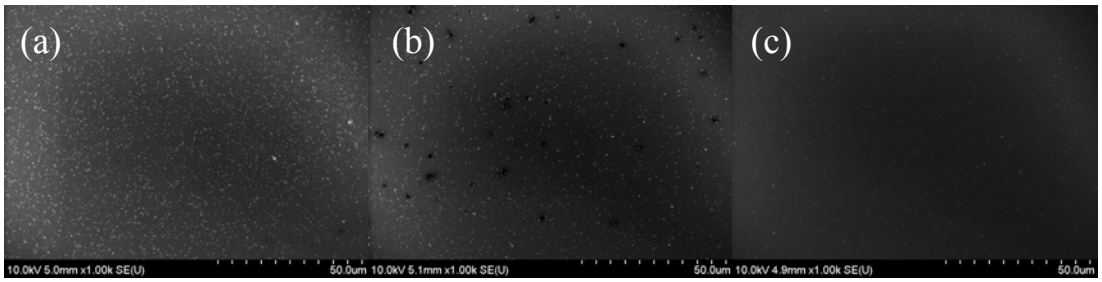

Figure 4.2. SEM images of deposited AgNC layers with different applied potential for 1 min. (a,b) 20V, (c,d) 10V, (e,f) 5V.

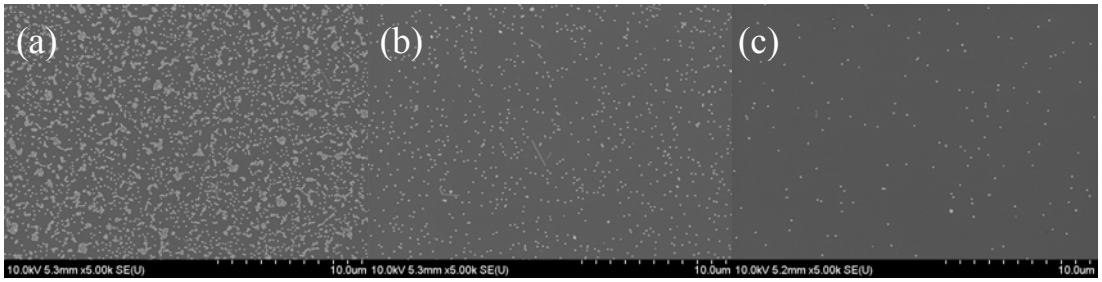

Figure 4.3. SEM images of AgNC layers formed by EPD with 40V potential for (a) 5min, (b) 1min, and (c) 10sec.

4.3 Experimental Procedures

Patterning of the anode : PMMA resist (950PMMA A4, Microchem) was spin-coated on a silicon wafer (4K RPM, 45sec, thickness 200nm) and dried (180^{o}C, 1min). Rectangular pores were drawn by e-beam writer, e_LiNE (Raith). The film was soaked and stirred in a development agent solution (MIBK:IPA=1:3) for 1.5mins for development. To remove the residual development agent, the film was rinsed by copious DI water.

Preparation of AgNC solution : A 110nm-AgNC solution was cleaned by centrifugation with EtOH and DI water. AgNC aqueous solutions were 7.5 ~ 60-fold diluted from the original AgNC solution.

EPD : The EPD set-up is depicted in Scheme 4.3. The substrates with PMMA patterns were used as anodes and a rectangular steel mesh piece (10mm x 20mm) was

used as the EPD of AgNCs. The distance between a steel-mesh cathode and a PMMA patterned silicon anode is 9.8mm. 1mL of AgNC solution was added to the cuvette. Potential (15~30V) was applied for 5 ~ 15sec.

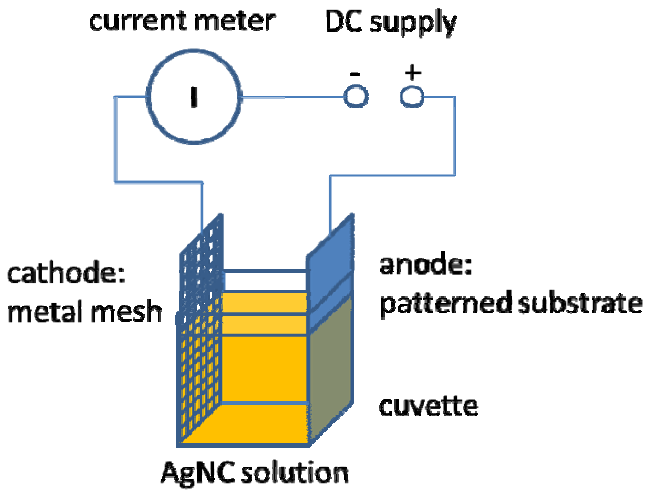

Scheme 4.3. Schematic diagram of the EPD set-up. Cathode: a metal mesh. Anode: a silicon piece with PMMA patterns. Distance between anode and cathode: 9.8mm. Current was monitored during EPD.

ATP adsorption and PMMA removal : Aminothiophenol (ATP) was used as Raman reporter, since it can easily form a monolayer on the silver surface and the number density per surface area are well known. After the EPD, the substrates were soaked in 0.4mM ATP solution for the ATP adsorption. Unbound ATP molecules were removed by rinsing extensively with ethanol. PMMA layer was removed by rinsing extensively with acetone. PMMA removal prior to ATP adsorption is also possible.

SERS measurements and SEM observations: Raman spectra were measured by microRaman (Horiba Jobin-Yvon LabRAM HR-VIS microRaman spectrometer). For the SERS measurements, the substrates were aligned so that the direction of the AgNC clusters matched with the polarization direction of the laser. SERS spectra

from all the clusters were obtained using 633nm (D2 filter, 10sec acquisition) and 785nm (D2 filter, 50sec acquisition) lasers. Soon after the SERS measurement, the number of AgNCs in each cluster was determined by SEM observation. SERS enhancement factor (EF) values were calculated by comparing the area of the Raman peak at 1078cm^{-1} (per molecule) in the clusters and in a 0.5M ATP reference solution.

4.4 Results and Discussion

4.4.1 Formation of AgNC Trimers and Tetramers with EPD

Figure 4.4 shows the result of the EPD with 30V for 15sec. Dark areas in Figure 4.4 indicate the PMMA layer, while bright areas are the exposed silicon surface. Most AgNCs are located on the silicon surface or on the PMMA layer near the exposed silicon surface. The AgNCs were successfully attracted toward the patterned areas.

We tried to reduce the applied potential as much as we could. The AgNC deposition into the pores was successful with voltage down to 15V. Sometimes, large clusters including double layered clusters formed under the EPD condition of 15V-5sec and current level around 40μA. The formation of large clusters could be prevented using a 60-fold dilute AgNC solution (~0.25mM) for EPD. The optimized EPD process is applying 15V potential for 10sec (9~12μA) with 60-fold dilute AgNC aqueous solution (~0.25mM).

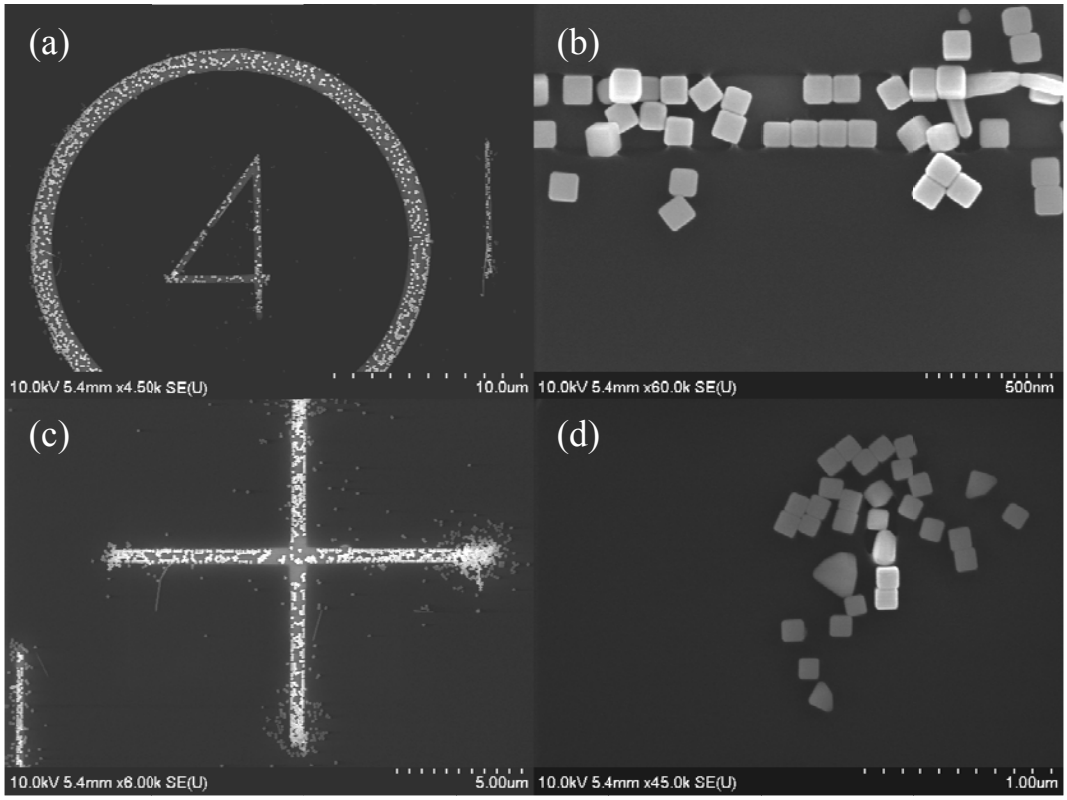

Figure 4.4. AgNCs on the PMMA patterned Si deposited by EPD at 30V-15sec. AgNCs in (a) the ring marker, (b) horizontal marker, (c) cross marker, and (d) rectangular pore.

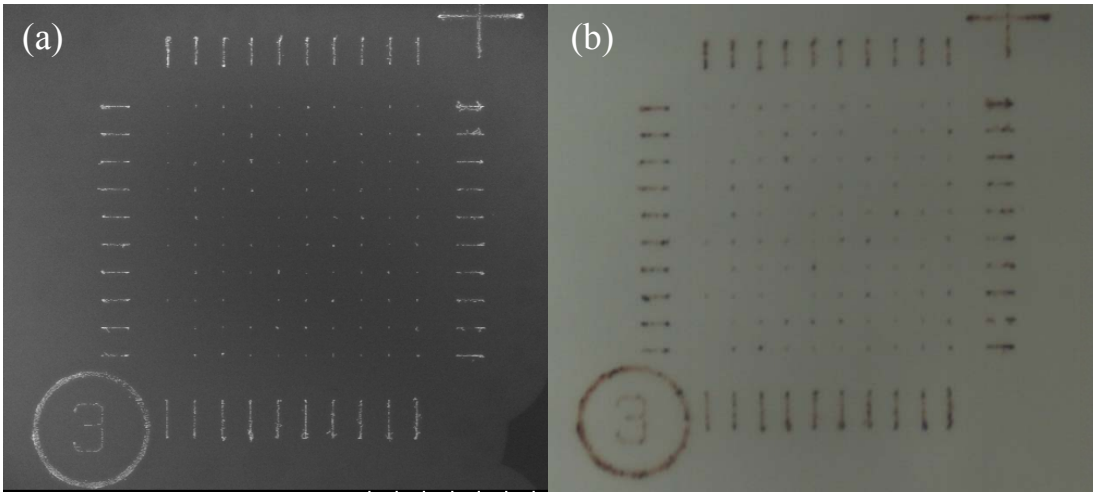

Figure 4.5. (a) a SEM image and (b) an optical microscope image of an array followed by EPD and PMMA removal process. Clusters are formed on the pre-determined positions.

The PMMA layer was removed by rinsing extensively with acetone. Figure 4.5 shows the AgNC clusters on the substrate after the PMMA removal. The AgNCs

which used to be on the PMMA layer (and not in the pores) were successfully removed during the PMMA removal. The AgNCs are located only at the pre-determined positions, *i.e.* rectangular pores and markers.

AgNC clusters were found in around 90% of the pore sites after the PMMA removal. The EPD process is a very efficient deposition method. In Figure 4.5b, gray spots indicate AgNC clusters. Darker spots represent bigger AgNC clusters. It is a benefit of EPD process with flat silicon substrates that scattered light by clusters on the substrate helps us recognize the presence of clusters.

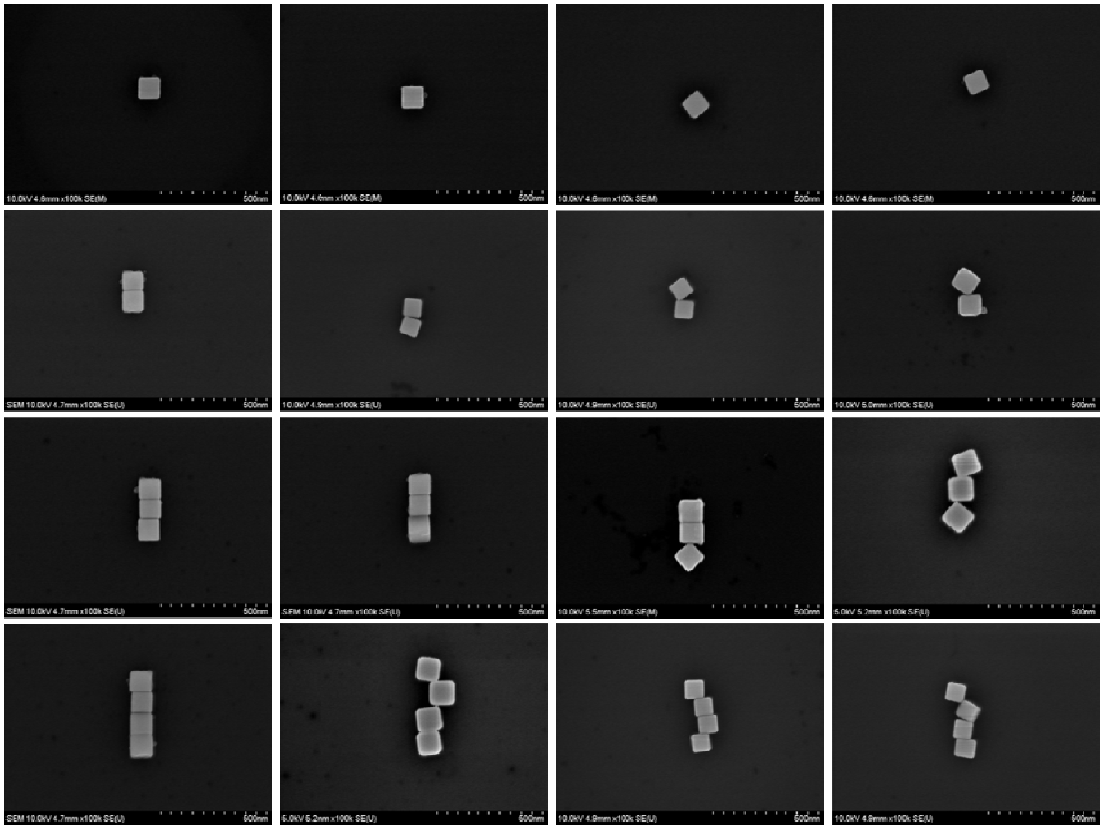

Figure 4.6. SEM images of different sized clusters formed by EPD process.

Figure 4.6 shows the magnified SEM images of clusters formed by the EPD process. Linearly aligned AgNC clusters were successfully formed in the rectangular pores so that the variations in azimuth angle were eliminated.

4.4.2 SERS with AgNC Trimers and Tetramers

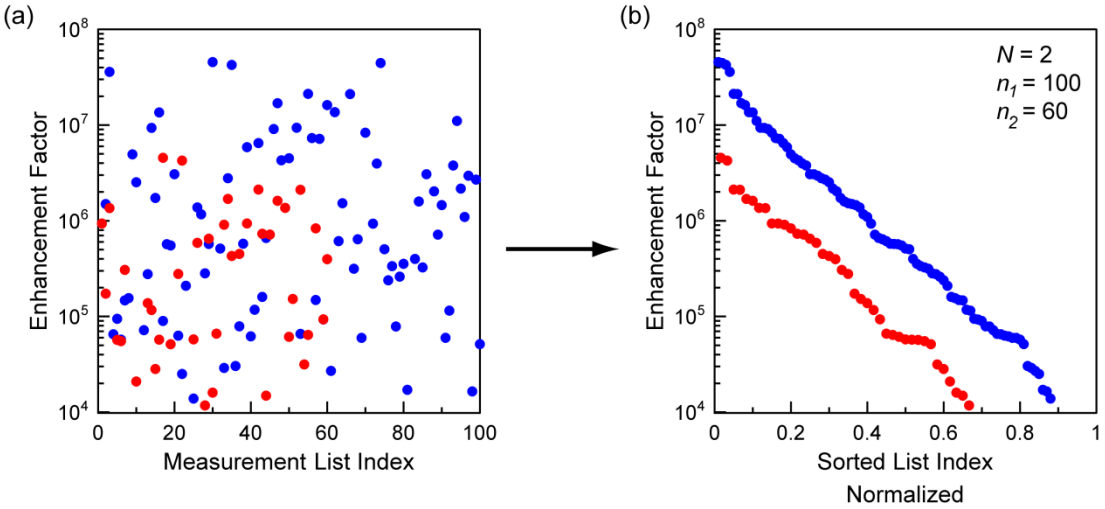

Figure 4.7. (a) The data was grouped into N categories (N=2): set 1 consists of a list of 100 values (blue), and set 2 consists of a list of 60 values (red). The list content is plotted against the list index that indicates the sequence in which the data was collected and has no physical meaning. (b) The values within each category are sorted in descending order. The list index is normalized to allow a direct comparison between the lists. The normalized list indices are 0.01, 0.02,..., 1 for set 1 with n_1=100 (blue) and 1/60, 1/30, 1/20,..., 1 for set 2 with n_2=60 (red). Note that 12% of the SSEF values in set 1 and 33% of the values in set 2 are lower than 104 and thus are not displayed in either plot.

For the analysis of the EF distribution, we grouped EF values by a category (*e.g.* number of cubes in a cluster). The grouped EF values are randomly distributed as shown in Figure 4.7a just after grouping. The EF values are sorted in diminishing manner from high to low. Then, we can obtain a trend line for the EF values in a certain category. However, the number of clusters in each category is not the same. Normalization of list index is needed to compare trend lines of categories with

different cluster populations. List index is divided by the number of cluster in the category (n_N). In Figure 4.7b, trend lines are built with the normalized list index (from $1/n_i$ to 1). By constructing these trend lines, it is easy to compare different data sets.

4.4.3 The Number of Nanocubes in the Clusters

Following the methods described in Section 4.4.2, we analyzed the effect of the number of nanocubes in the clusters on the EF values. Figure 4.8 shows the EF trend of each category with 2 different incident lasers.

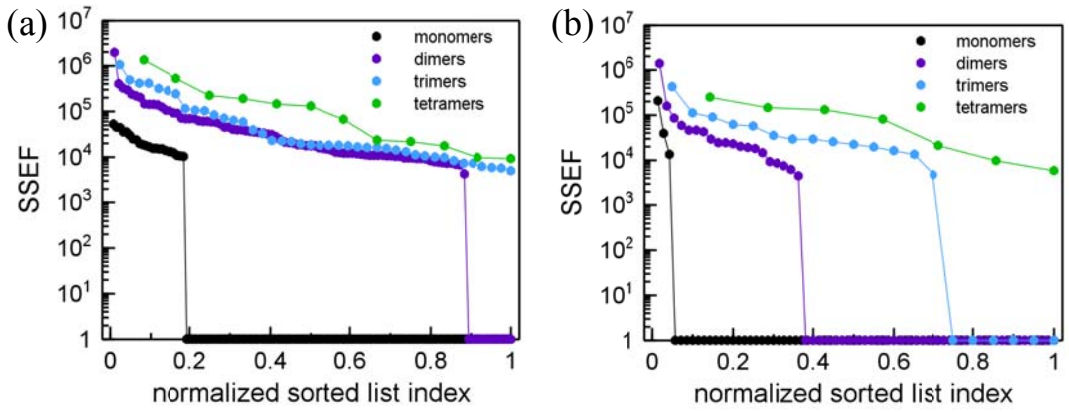

Figure 4.8. EF value trends of monomers, dimers, trimers, and tetramers measured with (a) 633 nm and (b) 785 nm lasers.

In Figure 4.8, each graph contains 4 trend lines indicating EF values of monomers, dimers, trimmers, and tetramers. Data points at the bottom forming horizontal line represent clusters whose SERS signal intensity is less than the detectable level around 10^4 of EF value. We call them 'silent clusters'. High portion of silent clusters represents low EF value trend, it is assumed that slopes of trend lines are same or high slope of EF value trend line indicates a fast decay of EF value from the highest EF value.

In the measurement with 633nm laser, there is a dramatic difference in the EF values between monomers and multi-cube clusters. Monomers do not contain any junction with neighboring nanocubes that can generate hot-spots. From a different point of view, the plasmon resonance frequency of the AgNC monomers on the silicon wafer, 533nm (calculated by Prof. Mayergoyz's group), is far away from the incident laser wavelength, 633nm, so the monomers cannot generate a significant enhancement of the field. Tetramers made a little higher trend line than trimers. The fact that 10% of dimers were silent indicates that the EF trends of the trimers and tetramers are a little higher than that of the dimers. The plasmon resonance frequencies of trimers and tetramers might be closer to 633nm than that of dimers.

With 785nm laser excitation, the change in the EF value trend by the number of cubes is clearer than with 633nm. More cubes in the clusters, more reproducible EF values are achieved. The slope of the trend line decreases, as the cluster size increase. The portion of silent clusters decreases as well from 95% of monomers to 0% of tetramers, as the cluster size increases. The difference in the portion of silent clusters indicates that tetramers are superior to monomers. Tetramers are robust, when 785nm laser is used.

We can use our data to deduce information on the plasmon resonance. The portion of silent clusters is 10% of dimers and 0% of trimers with 633nm laser and 60% of dimers and 25% of trimers with 785nm laser. The plasmon resonance frequencies of dimers and trimers are presumably closer to 633nm than 785nm.

Many researchers have focused on obtaining the largest EF by tuning cluster parameters.[30, 31] As shown in Figure 4.8, the EF values have a broad distribution

ranging 10^2. The maximum value must be affected by the number of data in this broad distribution. Thus, it is not proper to compare the maximum EF values, since the populations of trimers and tetramers are not comparable to that of dimers. For this reason, the EF trend lines are more meaningful than the maximum values.

The analysis on the cluster size indicates that the enhancement trend from the large cluster is higher (633nm) and more reliable (784nm).

4.4.4 The Configuration of the Clusters

Previously, it has been reported that the largest SERS enhancements occur when the nanocube dimers form face-to-face (FF) configuration with experiments and calculations.[31, 45] FF dimers can provide larger surface area at the junction than the other types of dimers. More molecules at the junction were expected to give out stronger signal.

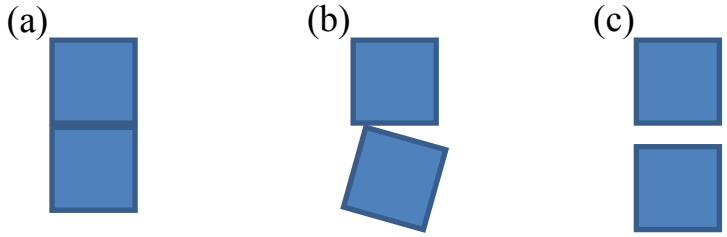

Scheme 4.4. (a) A face-to-face dimer, (b) a non face-to-face dimer, and (c) a dimer with a gap

In this analysis, we tried to delve into the effect of configurations on the SERS enhancement in fixed size clusters. Thus, all the dimers and trimers were sorted into three categories: FF gapless clusters, non-FF gapless clusters, and clusters with a gap. These configurations are illustrated in Scheme 4.4. Clusters whose gap cannot be

resolved by the SEM (≤ 3nm) are regarded as gapless. Clusters which contain at least one face-to-edge or edge-to-edge junction are regarded as non-FF clusters.

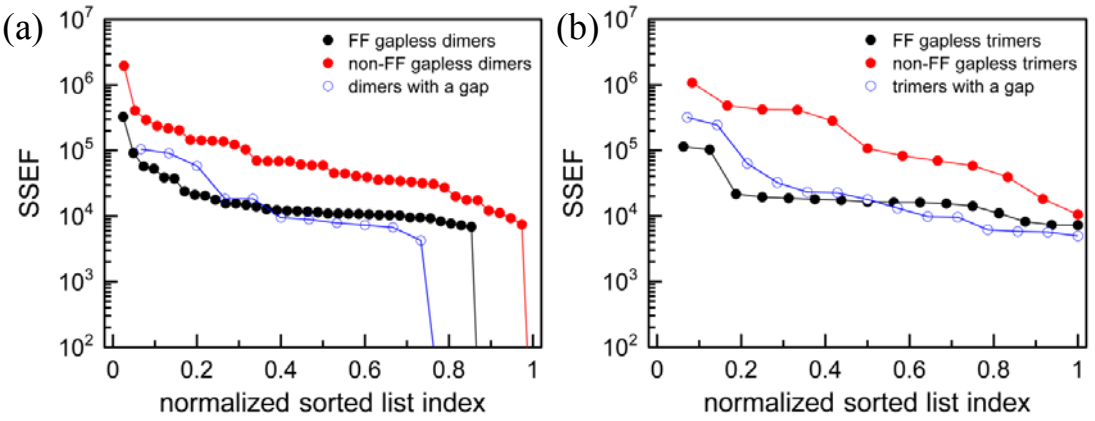

Figure 4.9. EF value trends (with 633nm laser) of (a) FF dimers, non-FF dimers, and dimers with a gap. (b) The corresponding data for trimers.

Two graphs are presented in Figure 4.9. One is for the dimers and the other for the trimers. Each graph contains 3 different trend lines for the 3 categories. Even though the dimers and trimers have difference in the cluster size, they have similar EF trend by configurations. The EF values of FF dimers and FF trimers are collectively lower than those of non-FF dimers and trimers. Strikingly, the FF clusters are comparable in their EF to clusters in which a sizeable gap (> 3nm) is observed. The change of the portion of silent dimers also agrees with this conclusion. The portion of silent dimers in the FF dimer category is higher than that in the non-FF dimer category. Our analysis for dimers and trimer by the configuration reveals that FF configuration is not desirable.

It is plausible (hypothesis) that the EF trend of the FF gapless clusters is lower than those of the non-FF gapless clusters because the ATP molecule cannot reach the

surfaces forming the junctions due to the very narrow gap in the FF configuration. To verify this hypothesis, the following experiments were designed and performed.

To make sure all the surface of AgNCs is covered with ATP molecules, the functionalization was carried out in advance to the EPD process (pre-functionalization). A monolayer of ATP molecules were formed on the surface of nanocubes by the dispersing AgNCs in 1mM ATP solution for 3hrs and removing unbound ATP molecules. These pre-functionalized nanocubes were deposited on patterned substrates containing rectangular pores by dropcasting. After the removal of PMMA layer, AgNC clusters were formed at only few among the pre-determined positions due to the dropcasting method. SERS spectra from the clusters were obtained and analyzed.

We obtained EF value trend lines for monomers and dimers (Figure 4.10). As shown in Figure 4.10, we did not get large number of monomers and dimers, since effective attracting force such as electrostatic force in EPD was not exerted on AgNCs during the dropcasting. Figure 4.10a indicates that the non-FF gapless dimers show higher EF trend line than FF gapless. What makes difference in EF trends between the two categories is not slow diffusion of ATP molecules to the FF type gap region. The result proves that the configuration of AgNC clusters is a critical parameter in SERS enhancement.

Despite of this proof, we cannot ignore the difference in the trend lines of monomers. If we compare the trend line of pre-functionalized monomers to the trend line of monomers functionalized after deposition (post-functionalization). The silent monomer portion decreased a lot from 80% to 55% due to the pre-functionalization

(Figure 4.10b). The large decrease in the ratio of the silent monomers can be explained by smaller gap formed by PVP molecules attached during the polyol reduction synthesis.[46] The gap distance between two cubes in a dimer (LATERAL gap) is twice the gap between a cube and silicon substrate (BOTTOM gap): The LATERAL gap is twice the thickness of the molecular layer on the AgNC surface. In Figure 4.10a, EF trend of FF dimer with pre-functionalization is a little higher than that with post-functionalization. The difference between them indicates a contribution of BOTTOM gaps in dimers to SERS enhancement. The fact that non-FF dimers showed higher EF trend than FF dimers regardless of the timing of the functionalization indicates that the LATERAL gap contribute to SERS enhancement more dominantly than the BOTTOM gap.

In summary, the BOTTOM gap is too narrow for ATP molecule to diffuse, while the LATERAL gap is sufficiently wide. Even though dimers consist of 2 BOTTOM gaps and 1 LATERAL gap, the LATERAL gap contributes to SERS enhancement more dominantly than the BOTTOM gap.

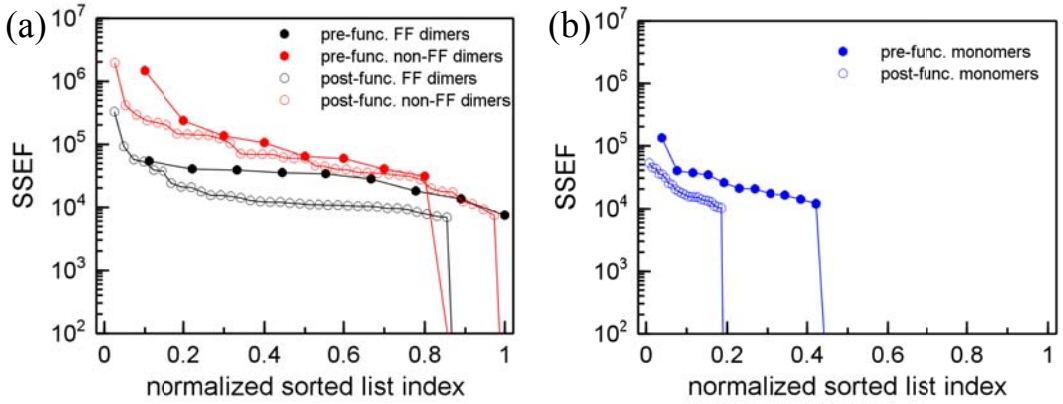

Figure 4.10. The result of pre-functionalization experiment with 633nm laser. The EF trend lines of (a) different configurations of the pre-functionalized and the post-functionalized dimers (from Figure 4.9a). (b) The EF trend line of the pre-functionlized and post-functionlized monomers. Post functionalization data was obtained from Figure 4.8a and Figure 4.9a.

The non-FF clusters are superior to the FF clusters in the SERS enhancement. The non-FF clusters overcome fewer molecules at the junction relative to the FF clusters. The electric field at the face-to-edge and edge-to-edge gap must be stronger than that at the face-to-face gap. The sharp corner at the junction must play an importance role in the SERS enhancement

4.5 Conclusions

EPD is a versatile tool for positioning of AgNCs. We succeeded in forming AgNC trimers and tetramers with good linear alignment using EPD. The deposition time and the applied potential are important factors in controlling the EPD process.

A large leap in EF values can be observed as the plasmonic structure increases in size from a single cube to a cluster of multiple cubes. Increasing cluster size from dimers to tetramers improves the reproducibility of EF values. The reason of this increase is that a plasmon resonance frequency of trimers and tetramers might be closer to 633nm than that of dimer. For the same reason, the reproducibility of EF values with 785nm increases as clusters get bigger.

Through the analysis for different configurations of dimers and trimers, we suggest that non-FF clusters are desirable for the preparation of SERS substrates with silver nanocubes. We think the decrease in EF values of FF gapless clusters is mainly caused by the absence of a sharp corner at the junction, not by the poor accessibility of ATP molecules into the face-to-face gaps. The gap between neighboring AgNCs contributes to SERS enhancement more than the gap between a AgNC and substrate.

Pre-functionalization guarantees the presence of the reporter molecules at all the surface regardless of gap size. Pre-functionalization is meaningful for scientific investigation and maximum enhancement. However, sample molecules cannot be adsorbed on the metal surface in advance to the formation of metal nanostructures in practical usage. Narrow gaps cannot contribute to SERS enhancement in practical applications.

4.6 Supplementary Research – Acquisition of Darkfield Scattering Spectra of AgNC cluster

Other researchers have reported darkfield scattering spectra of individual metal clusters.[21, 26, 47, 48] The darkfield spectra were taken using darkfield condenser. Usually, clusters were formed on transparent substrates, because the illuminating part including darkfield condenser was located opposite to the detecting part including objective lens (Figure 4.11a).

We tried to measure darkfield scattering spectra of the AgNC clusters formed by the EPD process using our microRaman equipment. For the measurement, we removed a cut-off filter before the detector and installed an external light source (HL250-AY, 150W Halogen lamp, AmScope), which illuminated the samples with an oblique angle with respect to the beam path of the detector (Figure 4.11b). Only light scattered by the cluster could reach the detector. Thus, the darkfield scattering spectra of the AgNC clusters can be obtained.

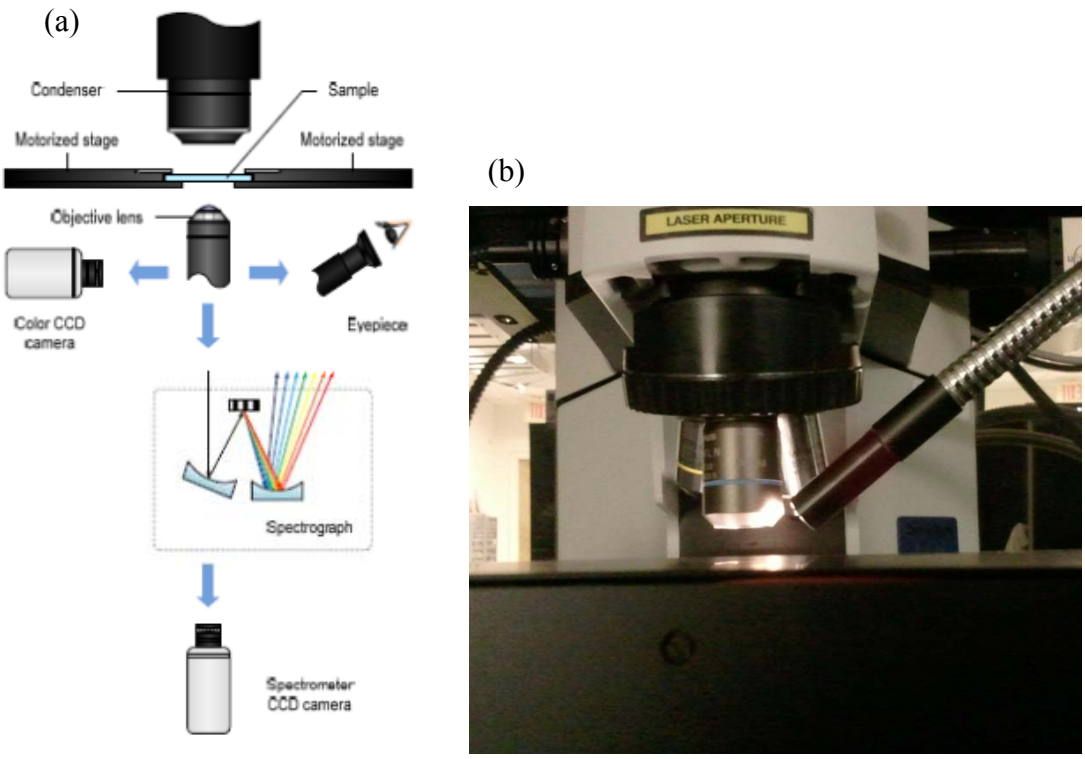

Figure 4.11. (a) Schematic diagram depicting equipment for the measurement of darkfield scattering spectra.[48] (b) Our microRaman with external illumination.

Spectra were taken from a monomer and a dimer for various illumination angles by rotating the samples. In Figure 4.13a, arrows indicate the various directions of illumination. As-measured scattering spectra of the monomer (Figure 4.13b) were normalized using blank spectra as described in Equation 4.1 (Figure 4.13c). The blank spectra are darkfield scattering spectra from the substrate without clusters. All spectra taken from the monomer contain only one peak (Figure 4.13c), while the spectra of the dimer are not consistent in the number of peaks or their positions (Figure 4.13d).

$$\boldsymbol{I_{normalized}} = \frac{\boldsymbol{I_{cluster} - I_{blank}}}{\boldsymbol{I_{blank}}} \qquad (4.1)$$

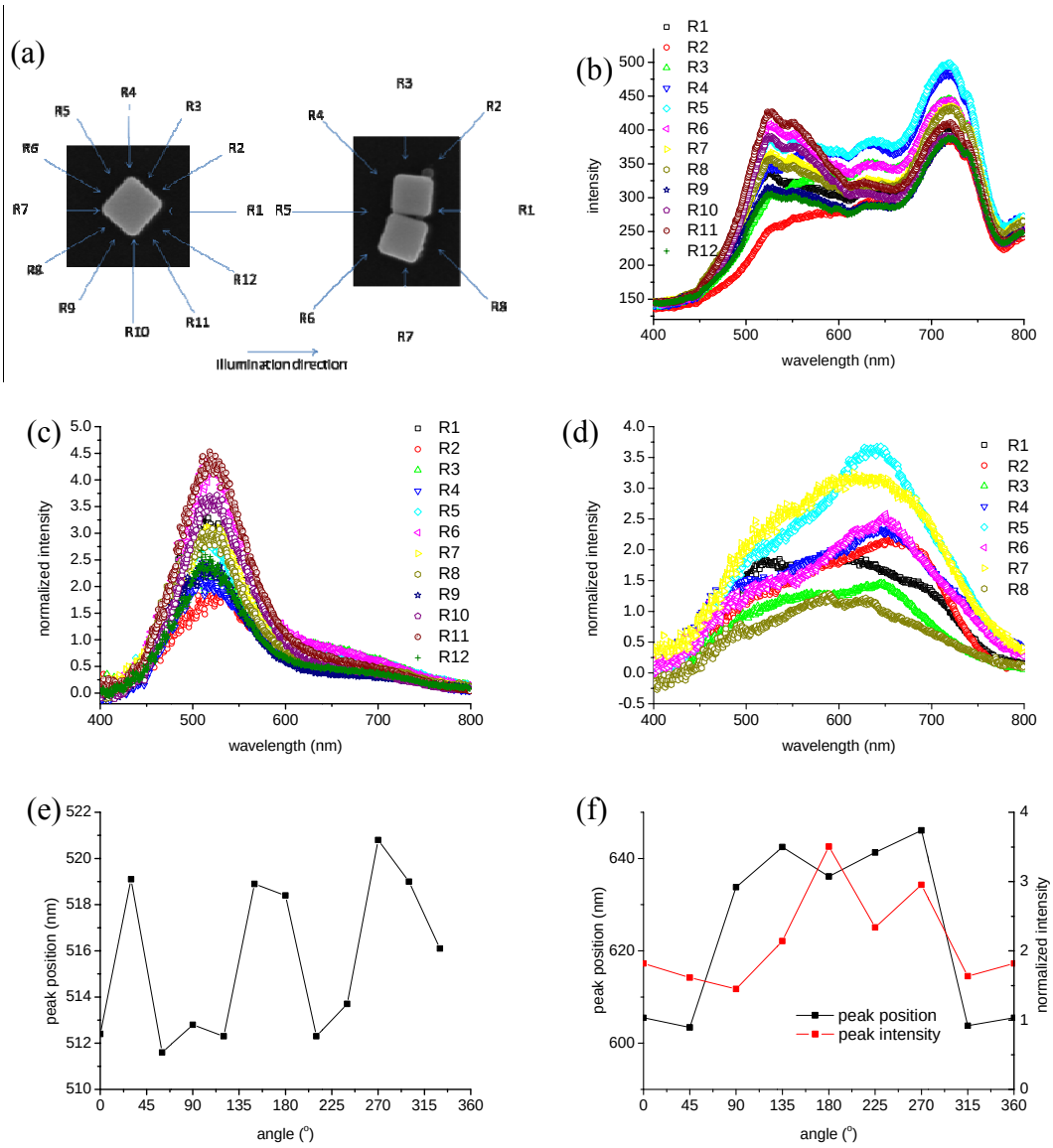

Figure 4.12. (a) Micrographs of a monomer and a dimer. Arrows indicate the directions of illumination. (b) Spectra of the monomer as measured. (c) Spectra of the monomer after normalization. (c) Spectra of the dimer after normalization. (e) Peak position of the monomer as a function of illumination angle. (f) Peak position and intensity of the dimer as a function of illumination angle.

Peak positions were analyzed as a function of illumination angle (Figures 4.13e and 4.13f). The peak of the monomer is at 516±5nm, whereas one of the peaks of the dimer is at 635±21nm. If the measurement shows angular dependence, the periodicity should be 90° for the monomer and 180° for the dimer. However, we cannot observe the periodicity in Figures 4.12e and 4.12f. Since no angular

dependence is observed in these deviations, they must be caused by deviations in the cluster position. We could not produce usable data with the modification of the microRaman equipment.

5 Self-Assembled SERS substrate with Tunable Surface Plasmon

5.1 Introduction

In preparation of SERS substrates, allocating metal nanostructures and tuning plasmon resonance are the main issues as mentioned in Chapter 1. Usually, the allocation of metal nanostructures in nano-scale with top-down method is expensive and time-consuming. The hybrid approaches using top-down and bottom-up exemplified in Chapter 3 and Chapter 4 are compromises between cost and precision. Still, we could not avoid the e-beam writing process. Utilizing block-copolymer can be an alternative method replacing the e-beam writing process.

Block-copolymers consist of two or more homopolymer subunits linked by covalent bonds. A homopolymer is made up of only one kind of monomers. Phase separation causes the formation of nanostructures. Several simple factors control the structural properties of the polymer film.[49] The volume fraction of the polymer blocks determines the block-copolymer morphology. The size and the distance between domains are determined by the overall molecular weight. In this way, block-copolymer can form body-centered cubic sphere, hexagonally packed cylinder, gyroid and lamellae structure in nanoscale. They can provide periodic nanostructures with great cost- and time-efficiency. Thus, the block-copolymer system is thought as one of the ideal candidates for templates, so that lots of effort has been devoted to guiding nanoparticle (NP) deposition by the block-copolymer templates.[43, 50-53] Capillary force, chemical reaction, electric field were used for attracting NPs.

On the contrary to other attempts utilizing the block-copolymer system for SERS substrates,[54, 55] in this research, we demonstrated the preparation of SERS substrates only with self-assembly technique. Periodic metal nanostructure was formed only by self-assembly and the surface plasmon resonance was tuned by wet chemical method. The controllability over metal NPs in nanoscale opens up the possibility of block-polymer templates for SERS substrates in the most time- and cost- efficient way.

5.2 Experimental Procedures

Materials: Polystyrene-*block*-poly(4-vinylpyridine) (PS-*b*-P4VP) block copolymer (number average molecular weight $M_n{}^{PS}$ = 47 kgmol^{-1}, $M_n{}^{P4VP}$ = 10 kgmol^{-1}, polydispersity index = 1.1) was purchased from Polymer Source, Inc., and used without further purification. Hexadecyl-trimethyl-ammonium bromide (CTAB), ascorbic acid, tetrahydrofuran (THF), 1,4-dibromobutane (DBB) and 4-aminothiophenol (ATP) were purchased from Sigma-Aldrich. Citrate-capped gold nanoparticle (AuNP) colloidal solution with 15 nm mean diameter was purchased from BBInternational. Silver nitrate ($AgNO_3$) and hydrogen tetrachloroaurate(III) trihydrate ($HAuCl_4$ $3H_2O$) were purchased from Alfa Aesar.

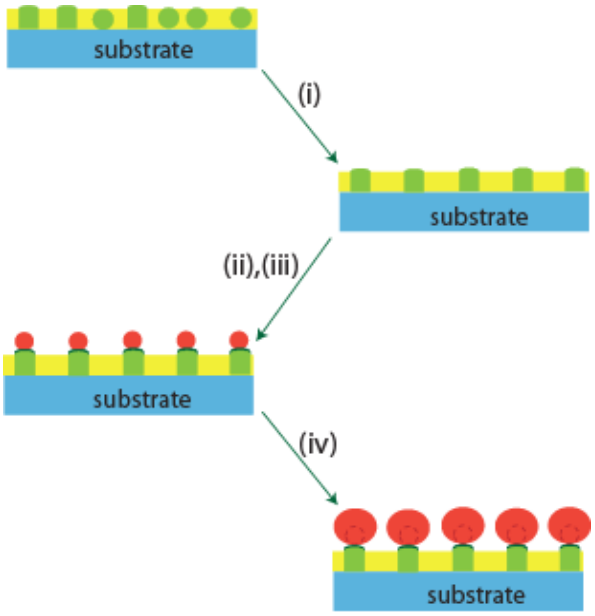

Scheme 5.1. SERS substrate fabrication scheme. (i) Solvent annealing. (ii) Quaternization. (iii) Colloid adsorption. (iv) Overgrowth. [key: cyan – substrate; green – P4VP; yellow – PS; red –Au].

Fabrication of SERS Substrates: PS-*b*-P4VP block copolymer was dissolved in THF to yield a 0.5 wt% polymer solution. The polymer solutions were filtered through a Millipore 0.45 μm poly(tetrafluoroethylene) filter. PS-*b*-P4VP films were prepared by spincoating at 3000 rpm for 30 s on silicon or glass substrates at ~23% RH. As-spun films were annealed in THF at room temperature for 6hrs. For the annealing, the films were placed in a glass chamber where THF in a glass dish was vaporized. The P4VP blocks in the PS-*b*-P4VP film were quaternized in DBB vapor. The annealed polymer film and a beaker containing DBB were placed in a desiccator. They were stored in vacuum for 6 hours. The PS-*b*-P4VP films were floated facing the citrate-capped AuNP solutions (15nm diameter, 1.4×10^{12}particles/ml) for 3 hours. The film was rinsed by DI water and blown by N_2 gas. Gold growth solutions were prepared by mixing 6 ml of 0.2 M CTAB, 0.384 ml of 0.04 M $HAuCl_4$, 0.228 ml of 0.01 M $AgNO_3$, 0.96 ml of 0.1 M ascorbic acid, and 11 ml of deionized water.[56]

The film was soaked in the solution for 1 ~ 15min. The growth reaction was stopped by rinsing the film with DI water. Scheme c1 depicts the preparation of the substrate.

Thin Film Characterization: Thin film surface morphology was characterized using a Dimension 3000 AFM from Digital Instruments, Inc. Silicon tips on a cantilever with spring constants ranging between 20.0 and 80.0 Nm (as specified by the manufacturer) were used. The degree of quaternization was measured using XPS on a Kratos AXIS 165 X-ray photoelectron spectrometer using a monochromatic Al Kα X-ray source (1486.6 eV). SEM observations were conducted using a Hitachi SU-70 Schottky FE-SEM working at 10 kV accelerating voltage and working distance around 5.5 mm. UV/Vis absorption spectra of the AuNP array films on glass substrates were measured using a Perkin-Elmer Lambda 25 UV/Vis spectrometer. For SERS spectrum collection, the substrates were immersed in 0.4 mM ATP solution in ethanol for 3 hours, rinsed extensively with ethanol, and dried under nitrogen. SERS spectra were measured with a Horiba Jobin-Yvon LabRAM HR-VIS micro-Raman spectrometer equipped with 515 nm, 633 nm, and 785 nm laser sources, a confocal microscope, and an x-y scanning stage. A 50x objective (numerical aperture NA=0.5) was used for all of the measurements. SERS spectra were obtained with incident laser power of 0.18 mW (515 nm), 0.11 mW (633 nm) and 0.67 mW (785 nm), and acquisition time of 30 sec. The Raman spectrum from a reference solution of 1.0 M ATP in pentanediol was acquired using the same spectrometer settings. The *Raman signal intensity* was quantified as the integrated peak area for the carbon-sulfur bond stretch of ATP at 1078 cm^{-1}. The number of molecules probed in each SERS substrate was calculated assuming that all the

particles were perfect spheres, a focal diameter of 2.2 μm and a monolayer surface density of 5 molecules nm^{-2} for ATP on gold.[38, 57] The number of molecules probed in the reference solution was calculated assuming a cylindrical focal volume of $\pi \times (1.1)^2 \times 16\ \mu m^3$. The *substrate enhancement factor* is the ratio of the Raman signal intensity per molecule of the SERS substrate and that of the reference solution.

5.3 Results and Discussion

5.3.1 The Properties of the Block-Copolymer Template

Quaternized block-copolymer templates were prepared and characterized by our coworker (Dr. Wonjoo Lee) in Prof. Briber's group. The topography of the self-assembly film is depicted in Figure 5.1a. The cylindrical P4VP domains (20nm in diameter) form hexagonal array in diameter in the PS matrix. The P4VP domains are slightly elevated. The hexagonal lattice parameter is 42nm. The center-to-center spacing and the diameter of the P4VP domain can be controlled by the choice of the molecular weight of the polymers and the ratio between the number of 4-vinyl pyridine and styrene repeat units.

The film was exposed to 1,4-dibromobutane (DBB) vapor, which converted pyridine groups of the P4VP block into quaternary pyridinium group as well as crosslinked[58]. The crosslinking can enhance the stability of the structure, reducing swelling and surface-reconstruction upon exposure to various solvents. Moreover, the quaternization reaction makes the P4VP domain positively-charged so that the domain can selectively trap negatively-charged particles in the solution. Thus, the quaternization reaction is crucial for the improvement of attracting force of the block-

copolymer film. XPS analysis of the quaternized film shows that 66% of pyridine groups are converted into the pyridinium bromide (Figure 5.2).

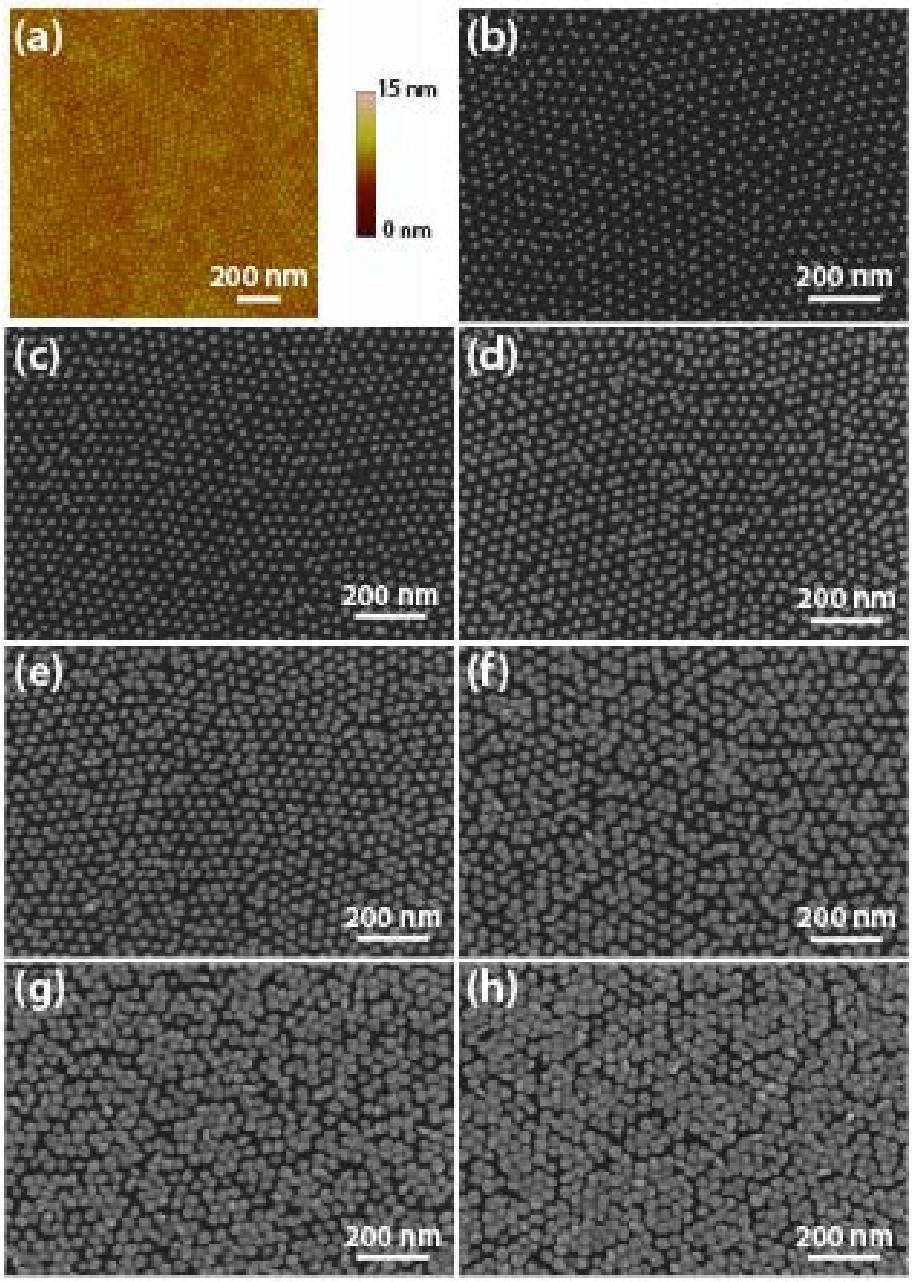

Figure 5.1. (a) AFM image of the THF annealed PS-*b*-P4VP ordered film. (b-h) SEM images of AuNP arrays on the quaternized PS-*b*-P4VP films after different overgrowth times: (b) 0 minutes, (c) 1 minute, (d) 3 minutes, (e) 5 minutes, (f) 7 minutes, (g) 10 minutes and (h) 15 minutes

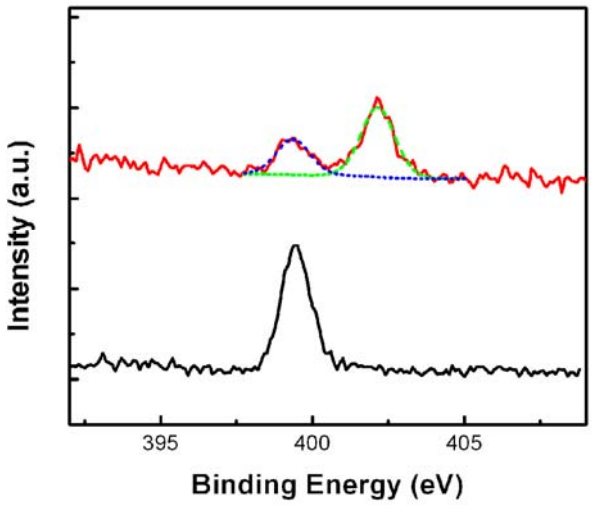

Figure 5.2. XPS N 1s core-level spectra of PS-*b*-P4VP film before (black line) and after (red line) quaternization. The peak at 399.4 eV is attributed to the nitrogen in the pyridine group. After quaternization, an additional peak appears at a binding energy above 402 eV, attributed to the positively-charged nitrogen.

5.3.2 Deposition of AuNPs and Tuning of Plasmon Resonances

Immersion of the quaternized block copolymer film in a solution of citrate-stabilized gold nanosphere results in self-assembly of the nanospheres into a hexagonal array commensurate with the array of P4VP domains (Figure 5.1b). 3hr adsorption of the gold nanospheres made 97% of the P4VP domains covered by the nanospheres. The electrostatic interactions existed between the positively charged pyridinium groups on the substrate and the negatively charged surface ligands of the nanospheres, which results in the deposition of AuNPs on the P4VP domains. The nanospheres adhere strongly to the block copolymer film. Therefore, the substrate can be washed and manipulated without the risk of losing the hexagonal order. In addition, the AgNPs can be chemically grown further to tune the plasmon resonance. This assembly has flexibility for the deposition of other negatively charged NPs.

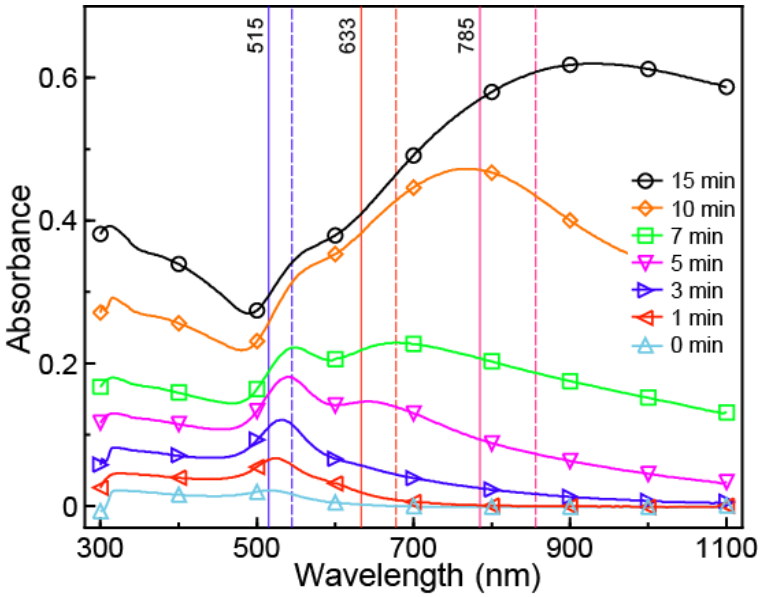

Figure 5.3. UV/Vis attenuation spectra of SERS substrates fabricated on glass with overgrowth times ranging from 0 to 15 min. The vertical lines indicate the wavelengths of the incident (solid) and the scattered (dash) light utilized in our SERS measurements

The gap size between adjacent NPs is one of the key factors determining the surface resonance frequency and the SERS enhancement factor as mentioned in Chapter 1.[16, 59-63] The inter-particle gap size can be defined as the difference between the center-to-center spacing and the nanosphere diameter. The former is set by the block-copolymer template. Thus, tuning of the gap size can be carried out by tuning the nanosphere diameter. The nanospheres were gradually grown from their original size by soaking the substrates in an aqueous solution of chloroauric acid, silver nitrate, ascorbic acid and hexadecyltrimethylammonium bromide ("Au growth solution"). As the nanospheres gradually grow in diameter, the gap size decreases (Figures 5.1b-h and Table 5.1). Since the overgrowth reaction rate slows significantly at the narrow gaps between the particles, growth of individual NPs is favored over coalescence of adjacent NPs. This makes the process highly controllable (by varying

the soaking time) and the product uniform. The uniformity of the substrates is manifested in the marked peaks observed in the UV/Vis attenuation spectra of the SERS substrates fabricated on glass represent (Figure 5.3). Two extinction peaks can be seen in the spectra. The high photon energy peak is assigned as a resonance peak from the localized surface plasmons of the individual nanospheres. The low photon energy peak is related with an extended surface plasmon delocalized over the array. Both peaks gradually evolve with overgrowth reaction time. As the nanospheres forming a hexagonal array grow larger and the gaps between them narrow, the localized surface plasmon resonance peak at 520nm gradually red-shifts and the emerging lower-energy peak red-shifts and noticeably intensifies. These spectral changes results from the increase in the coupling between plasmons on adjacent nanospheres. Figure 5.4 shows a photograph of a series of SERS substrates prepared on silicon with varying overgrowth times, corresponding to the spectra shown in Figure 5.3. Clearly, the spectral shifts are perceptible also in reflection mode. Thus, the substrates can be tuned to realize SERS substrate operating at a range of wavelength from 500 to 900nm.

Table 5.1. Evolution of the parameters of the NP arrays as a function of overgrowth time.

Reaction time [min]	NP diameter (average ± standard deviation) [nm] [a]	Gap size (calculated average) [nm] [b]
0	16.6 ± 1.8	23.0
1	20.2 ± 1.5	18.4
3	24.8 ± 2.0	14.6
5	27.6 ± 2.4	11.2
7	32.7 ± 3.3	9.5
10	34.3 ± 4.4	6.6
15	36.5 ± 6.3	4.1

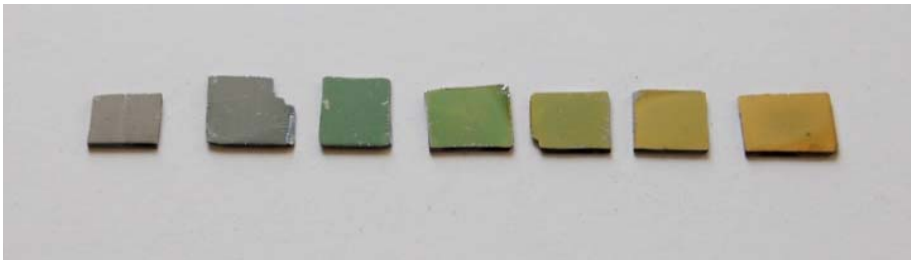

Figure 5.4. Photograph of SERS substrates fabricated on silicon with overgrowth times ranging from 0 (left) to 15 min (right), under white light illumination. The change in the perceived color implies a variation in the frequency of the surface plasmon resonances. [Credit: Faye Levine]

5.3.3 Characterization and Appreciation of SERS Substrates

For the SERS measurement, reporter molecules, ATP, were adsorbed on the gold surface by soaking the substrates in a dilute solution of the molecule. After unbound molecules removed by rinsing with ethanol, a monolayer of the molecules was formed. SERS spectra from a series of SERS substrates with varying diameter of gold nanospheres were collected. The SERS signals from the same SERS substrates were measured using 3 different lasers. All the SERS spectra contain characteristic peaks of 4-aminobenzenethiol, however, the signal intensity (peak area at 1078cm^{-1}) per molecule changes dramatically from SERS substrate to substrate. That is, the maximum SERS enhancement is achieved with the substrate in which the overgrowth process in the Au growth solution was carried out for 7min, when the SERS spectra were obtained with a He-Ne 633nm laser (Figure 5.5).

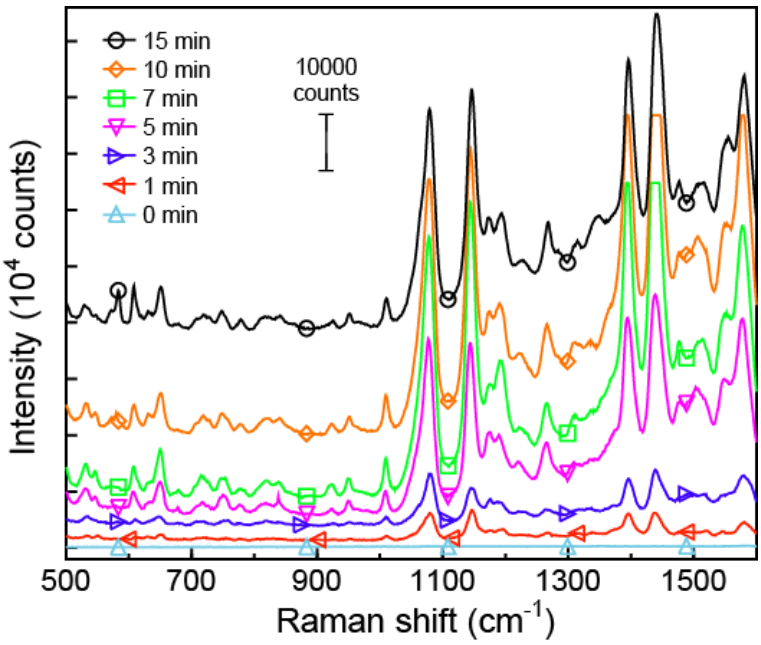

Figure 5.5. Surface-enhanced Raman spectra of 4-aminobenzenethiol on our series of SERS substrates with 633nm laser. The meaning of the colors/symbols is the same as in Figure 5.3. The spectra were shifted vertically for clarity.

The enhancement factors of the SERS substrates were calculated taking into account the number of molecules on the surface of the plasmonic nanospheres and in the focal volume of the reference solution. Figure 5.6 describes the dependence of the SERS substrate enhancement factor on the overgrowth time and the laser wavelength. Two guiding principles can explain the trends in the magnitude of the enhancement factor: (i) The enhancement factor increases as the absolute value of the ratio of the real to imaginary components of the permittivity of the metal, $|\varepsilon_1/\varepsilon_2|$, increases.[8, 64] For gold, this ratio increases with the increase in wavelength in the range 500 – 900nm (from ~1 to 33).[65] As a result, the highest enhancement factors were obtained using the 785nm laser and the lowest using the 515nm laser. (ii) The optimal SERS performance is achieved when the surface plasmon resonance peaks of the substrate is slightly red-shifted with respect to the incident laser wavelength.[66]

Thus, for a given laser, there is an optimal overgrowth time (*i.e.* diameter to gap ratio) that maximizes the enhancement factor.[13] For a longer wavelength laser, the optimal overgrowth time is longer. The optimal overgrowth time correlates with the shift in wavelength of the low-frequency extended surface plasmon resonance peak (λ_{max}=678 at 7min and λ_{max} =768nm at 10min). In the case of the 515nm argon ion laser, the high-frequency surface plasmon resonance peak in all our substrates matches the laser. Consequently, the enhancement factors measured by the 515nm laser show a small variation range (Figure 5.6). These experimental results are in agreement with theoretical calculations on field enhancement in periodic 2D arrays.[59]

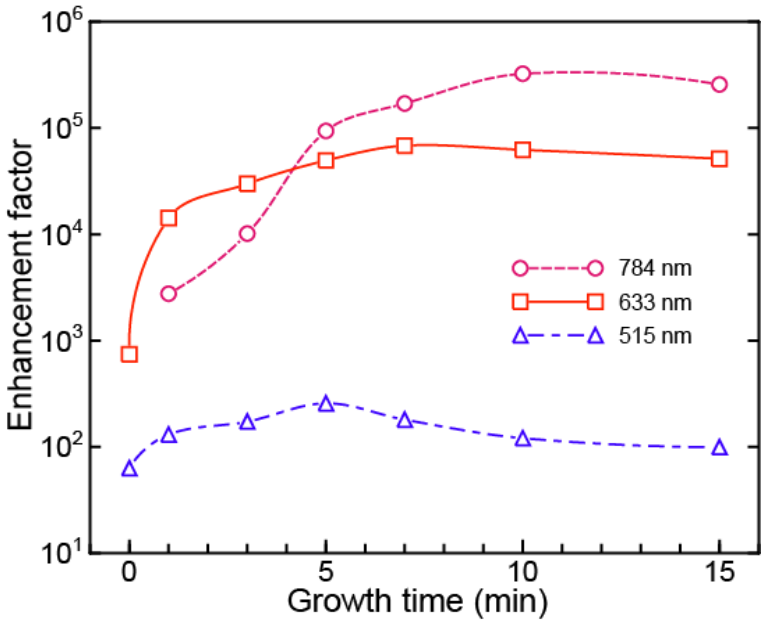

Figure 5.6. SERS substrate enhancement factors as a function of overgrowth time and probing (incident) laser wavelength.

5.3.4 Uniformity of SERS Enhancement

The SERS substrates were fabricated on glass and silicon wafers with areas of at least 1cm^2. Since the fabrication process consists of self-assembly and templating, a hexagonal array with perfect periodicity cannot be achieved. Defects in the registry of the polymer domains and in the deposition of the nanospheres are observed (Figure 5.1). These structural defects may cause variation in SERS enhancement location-by-location, undermining the utility of these SERS substrates. To mitigate this concern, 120 different sites on each substrate were probed and SERS enhancement factor distribution was obtained. As shown in Figure 5.7 and Table 5.2, the site-to-site variations within a substrate are small, while the enhancement factor variations resulting from varying the overgrowth reaction time are significant. The substrates with high enhancement factor (overgrowth time of 5 – 7min) show most uniform enhancement. For comparison, the enhancement factor distribution of an e-beam evaporated thin silver film on a silicon wafer was analyzed. In this substrate, the standard deviation is 50% of the average enhancement value, while the standard deviation is less than 10% of the 5min-overgrowth substrate. This comparison indicates that the SERS substrates prepared by self-assembly and templating are effectively homogeneous.

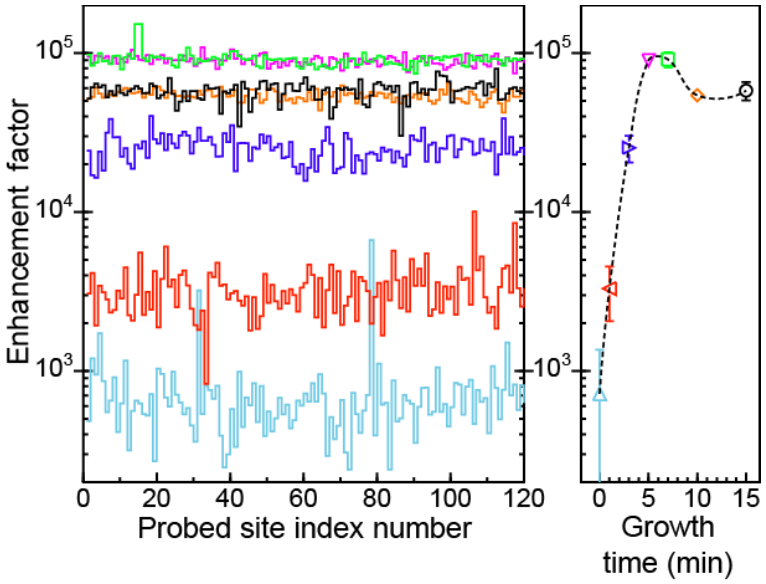

Figure 5.7. SERS substrate enhancement factor as a function of overgrowth time. Left: Collection of data from 120 sites probed by a 633 nm laser. Right: Average values and standard deviation. The meaning of the colors/symbols is the same as in Figure 5.3.

The SERS substrate enhancement factor values we got by self-assembly are significant in magnitude; enhancement factors could be increased by using silver instead of gold.[67-69] The enhancement factor values are lower than those from silver nanocube cluster in Chapter 2, however the SERS response of individual clusters is highly anisotropic: strong enhancement is obtained only at parallel orientation of the cluster axis and the laser polarization.[40, 45, 70-72] Our SERS substrates with hexagonal array of gold nanospheres display a uniform SERS response regardless of orientation and position, which is extremely convenient for practical applications. The substrates retained their SERS activity for at least 6 months of storage in air.

Table 5.2. Evolution of the enhancement factor as a function of overgrowth time.

Reaction time [min]	Enhancement factor (average ± standard deviation) [a]
0	720 ± 640
1	3300 ± 1200
3	25300 ± 4900
5	89800 ± 6200
7	91100 ± 10000
10	54100 ± 5200
15	57900 ± 7600

[a] Analysis based on measurements on 120 different sites on each substrate, using the 633 nm laser and the 1078 cm^{-1} Raman peak of ATP.

5.4 Conclusions

We have characterized SERS substrates made through the self-assembly of gold nanospheres, guided by a chemically modified PS-*b*-P4VP block copolymer template. Tuning the nanosphere size and the gap size is effective to optimize the SERS enhancement factor. By overgrowing metal on the anchored nanospheres, the plasmon resonances of the substrate were tuned and the SERS substrate enhancement factor was maximized for a given type of input laser. These SERS substrates show enhancement factors that are significant in magnitude and highly uniform spatially. Due to their low-cost, reproducibility and tenability, these SERS substrates could make Raman the method-of-choice in a wide range of chemical sensing applications.

6 A unique Solid-Solid Transformation of Silver Nanoparticles on Reactive-Ion Etching Processed Silicon

6.1 Introduction

During the preparation of the substrate for SERS with AgNCs in Chapter 3, we encountered unintended silver deposit growth. The silver deposits in the cavities stopped us from the SERS research with AgNCs. We needed to find a way to get rid of these silver deposits. However, the silver deposits had very exotic shapes of metal nanostructures. Furthermore, their shapes were different from the AgNCs in shape and some of them were smaller than AgNCs in size. The silver deposits consumed solid-phase particles, not ions for its growth. This phenomenon is sufficiently intriguing to make us investigate further.

In the further investigation, we found out that the unintended growth reaction is associated with accumulated re-deposition during SF_6/O_2 RIE process established the way to control over the silver deposits. We demonstrated the formation of nanoscale patterns consisting of arrays of silver nanoparticles using microfabrication technique, *i.e.* conventional photolithography. This is the first work to realize nano-sized features using edge sidewalls of micropatterns as far as I know. This work suggests a way to allocate metal nanostructure with high precision.

6.2 Experimental Procedures

Materials: 1,5-Pentanediol (Acros, 98%), silver nitrate (Alfa-Aesar, 99.995% metal base), copper(II) chloride (Sigma-Aldrich, 97%), polyvinylpyrrolidone (Sigma-

Aldrich, M_w=55K), 4-mercapto-1-butanol (Sigma-Aldrich, 95%), sodium borohydride (Fisher Scientific) and ethanol (Pharmaco-AAPER, 200 Proof, anhydrous) were used as received. P-type (100) boron-doped silicon wafers, 20-30 ohm-cm resistivity, were used as substrates (Silicon Inc.). Polymethylmethacrylate e-beam resist (950PMMA A4) and developer (MIBK/IPA 1:3 developer) were purchased from MicroChem Corp. S1813 photo resist and CD-30 developer were purchased from Shipley. Deionized (DI) water was obtained from a Thermo Scientific EASYpure® RoDi ultrapure water purification system.

E-beam lithography (EBL): Polymethylmethacrylate (PMMA) resist was spin-coated on silicon substrates at 4000 rpm for 45 sec and subsequently baked at 180°C. E-beam writing was performed with a Raith e_LiNE system, an electron beam lithography tool, using an accelerating voltage of 15 keV and an exposure dose of 145 $\mu C/cm^2$ with a 10 μm aperture. In patterning dose matrices, exposure dose was varied in the range of 70–301 $\mu C/cm^2$. After the patterns were developed in a MIBK/IPA developer solution, the patterns were transferred to the underlying silicon substrates by dry etching. The dry etch was carried out in a reactive ion etching system (Trion tech.) for 10 sec with 100 W power and a pressure of 50 mTorr in a flow of SF_6/O_2 (50:10 sccm). Unless noted otherwise, the PMMA resist was retained during subsequent steps. The EBL patterns were square arrays of circular pores 0–250 nm in diameter, lines 100 μm long and 150 nm wide, and rings 2.15 μm wide. Additionally, a clean silicon wafer was processed by RIE as a control.

Photo-lithography: 100 μm squares, 50 μm cross-bars and 10 μm wide line trenches were patterned onto silicon by conventional photolithography and dry

etching. Shipley1813 photoresist was spin-coated on silicon substrates at 3000 rpm for 40 sec, followed by soft bake of the coated substrate at 90°C for 1 min. The exposure was carried out for 6 sec using a Cr-mask (EVG 620 mask aligner). Patterns were developed in the CD-30 developer for 60 sec. The patterns were transferred to the silicon substrates in a reactive ion etching system (Trion tech.) using the same conditions as with the EBL patterns. After the RIE process, the photoresist layer was removed with toluene. Additional control experiments were performed without removing the photoresist from the patterned wafers.

Preparation of Ag solutions: Solutions of silver ions and suspensions of silver nanospheres (AgNSs) and silver nanoparticles (AgNCs) were freshly prepared. The suspensions contained borate-coated AgNSs 20±10 nm in diameter (1 mM or 0.025 mM by metal) or polyvinylpyrrolidone-coated AgNCs 70±5 to 100±10 nm in edge length (1 mM or 0.5 mM by metal). Silver ion solutions were prepared as 1 mM $AgNO_3$ in DI water or ethanol.

AgNCs were synthesized in pentanediol by the polyol reduction process.[73] The AgNCs were cleaned with ethanol (EtOH) by 4 cycles of centrifugation for 5 min at 13000 rpm to remove pentanediol, excess polyvinylpyrrolidone (PVP) and residual silver ions. The AgNCs were resuspended in EtOH or DI water for the experiments.

AgNSs were synthesized by reduction with sodium borohydride.[74] The AgNS suspensions were used as made or after 10-fold dilution with DI water.

For ligand exchange, 10 μL of 10 mM 4-mercapto-1-butanol (MBuOH) solution were added to 1 mL of the nanoparticle suspensions (0.025 mM AgNSs or

0.5 mM AgNCs). The solutions were then cleaned by centrifugation-resuspension cycles to remove excess MBuOH molecules.

Oxygen plasma treatment: The O_2 plasma treatment of the substrates was carried out in a reactive ion etching system (Trion tech.) using 150 mTorr O_2 atmosphere at a power of 50 W for 30, 45, 60, 150, and 300 sec.

Formation of silver deposits on patterned silicon substrates: Silicon substrates were submerged in the silver solutions for 30 min and 15 hrs at room temperature. At the end of the reaction period, the substrates were thoroughly rinsed with ethanol and DI water.

Galvanic exchange: Gold nanoparticles were grown by galvanic exchange at an elevated temperature (100°C).[75] Silicon substrates were placed in a vial containing 10 mL of boiling DI water. While stirring, 5 mL of 0.1 mM $HAuCl_4$ were added dropwise to the vial. After 10min, the substrates were retrieved, thoroughly rinsed with DI water and dried.

Silicon nanowire (SiNW) growth: Growth of SiNWs was conducted in a CVD reactor (Atomate Corp.). Silicon substrates bearing gold nanoparticles were placed in the center of the reactor. The chamber was evacuated with a roughing pump and back-filled with Ar (0.5 Torr, 100 sccm). The substrate temperature was raised to 480°C at a rate of 10°C/min. SiH_4 was introduced to the chamber at a flow rate of 20 sccm and pressure of 2 Torr for 2 min resulting in gold-catalyzed nanowire growth.

6.3 Results and Discussion

6.3.1 Conditions Affecting the Solid-Solid Transformation of Silver Nanoparticles

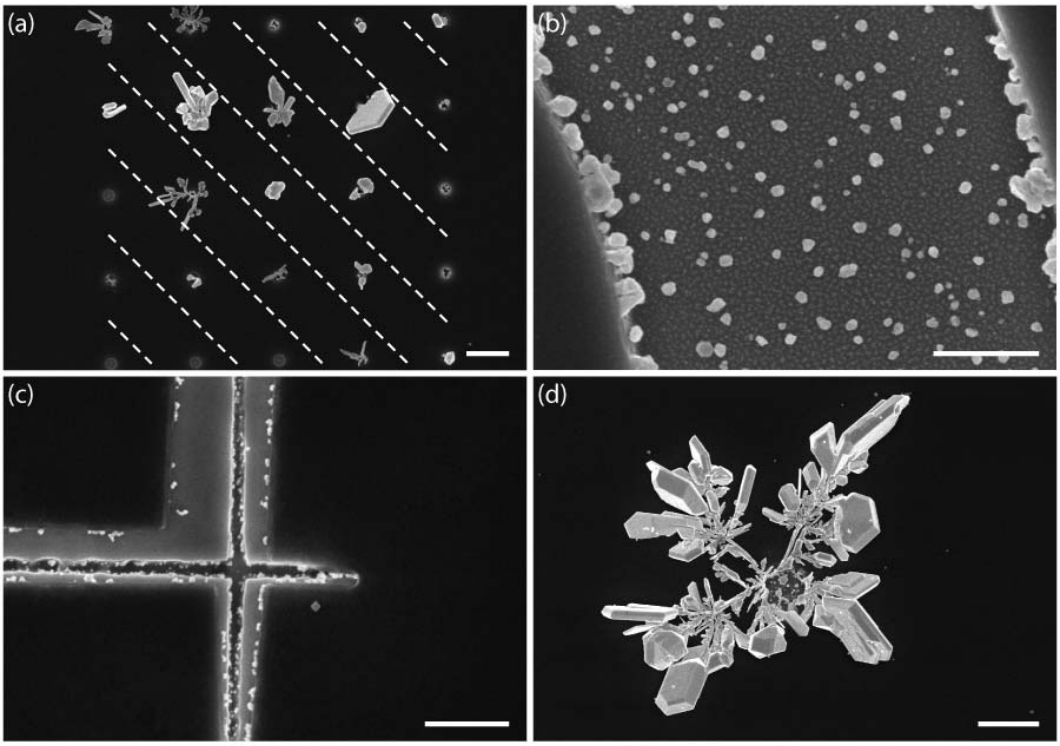

Figure 6.1. SEM images of silver deposits on EBL-patterned substrates that were dipped in EtOH suspensions of AgNCs for 15 hours. (a) Deposits in a dose matrix. Exposure dose: 70 – 301 μC/cm^2. Scale bar: 1 μm. (b) Deposits in a section of a wide ring pattern. Scale bar: 500 nm. (c) Deposits along a crossing of two narrow lines. Scale bar: 1 μm. (d) A deposit with dendritic shape and faceted ends on a defect site. Scale bar: 2 μm.

Silver nanoparticles in EtOH or DI water suspensions react at room temperature with lithographically-patterned silicon substrates to generate deposits of silver ranging in size from several nanometers to several microns. We will first present the results from the reaction between PVP-coated AgNCs in EtOH and e-beam patterned, dry-etched substrates (covered with the patterned PMMA layer). As a benchmark reaction, this reaction was studied to the largest extent.

Figure 6.1 shows the morphology of the reaction products obtained in (a) small pores, (b) a portion of a wide ring-shaped trench, (c) a thin, long trench and (d) an isolated, micron-size defect in the PMMA film. The morphology of the deposit can be globular, facetted or dendritic, and has no resemblance to the original cubic shape of the silver nanoparticles in solution. Furthermore, deposits smaller in size than the original AgNCs and others much larger in size were found on the silicon substrates. The images clearly demonstrate that the deposition of silver is localized to the patterned areas that were exposed to the electron beam and the reactive ion beam. No silver particles were found on planar areas covered with PMMA. Moreover, regardless of the aspect ratio of the patterns the products form at substantially higher densities along the edges and the vertical walls of the patterns than along its horizontal surfaces.. This is clearly observed in the micron-size patterns in Figures 6.1b and 6.1d, where the larger and denser silver deposits line the vertical walls of the trench and the perimeter of the defect. The same trend holds for the sub-micron patterns in Figures 6.1a and 6.1c, yet due to the large size of the deposits compared to the patterns, the edges are not always discerned.

The 5-by-5 array of small pores in Figure 6.1a is a "dose matrix" consisting of pores, ranging from 0 to 250 nm in diameter. Diagonal dashed lines separate groups of pores of the same size. The pore diameter increases as the dose of the e-beam increases from 70 $\mu C/cm^2$ (bottom left pore) to 301 $\mu C/cm^2$ (top right pore). This matrix demonstrates that the size and morphology of the silver deposits has a complex dependence on the lithography parameters. While there is a wide variation in the size and shape of the deposits in the pores, the average size of the deposits

increases with pore size up to ~200 nm in diameter, and then decreases. We attribute this non-monotonic trend to the dependence of the amount of silver deposited on both the pore size and the pore aspect ratio: the larger the pore and the larger the pore aspect ratio, the larger the amount of silver deposited. Comparing Figures 6.1b and 6.1c leads to the same conclusion: larger silver particles are formed in the high-aspect ratio line pattern compared to the wide trench.

Figure 6.1c provides an additional clue to the mechanism of formation of silver deposits. The line pattern created by the EBL writer on the PMMA film and transferred to the silicon by RIE is 150 nm wide. While the substrate was immersed in EtOH the PMMA layer swelled and shifted with respect to the underlying substrate to expose a ~1-3 μm wide band of silicon. We observe that the planar silicon surface exposed by a shift of the PMMA is free of silver, while the vertical walls of the line pattern in both the PMMA and the silicon are decorated with silver nanoparticles. The nanoparticles attached to the upper section of the side-wall (PMMA) are larger than those in the lower section (silicon).

The silver deposit shown in Figure 6.1d is typical to those seen in defect sites. The center of the structure displays a dendritic morphology, suggesting a high reaction rate at the initial stage of formation, and the peripheral grains are large, facetted single crystals that were formed at slower rates. The size of the silver structures formed in the defect sites is on average larger than the structures formed in the EBL patterns, possibly due to the lack of competing nucleation sites in close proximity.

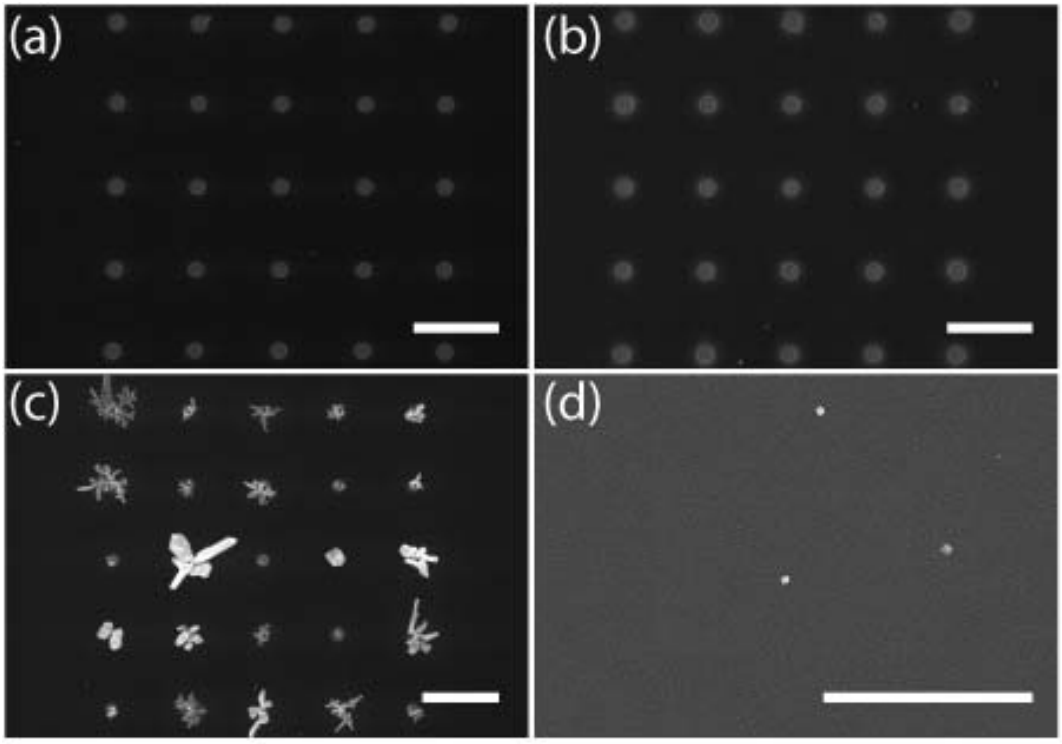

Figure 6.2. SEM images of silicon substrates that were dipped in EtOH suspensions of AgNCs for 24 hours at various patterning stages. (a) After electron beam exposure (array of uniform circles patterned at 145 μC/cm^2). (b) After developing the PMMA resist. (c) After RIE. (d) Silicon wafer dipped in an EtOH suspension after SF_6/O_2 RIE with no resist (not patterned). All scale bars: 2 μm.

The conditions for the formation of silver nanostructures along the lithographic patterns were investigated by varying the substrate (Figures 6.2, 3b and 3e) and the silver source (Figure 6.3). The formation of the silver deposits was investigated by submerging the silicon substrate in the AgNC suspension following every step in the sequence of the nanofabrication of arrays of uniform pores. The substrate was tested after spin-coating, after exposure to the electron beam (Figure 6.2a), after soaking in the developer (Figure 6.2b), after the exposure to the ion beam (Figure 6.2c) and after removal of the resist in acetone. No silver deposits were found in substrates prior to the SF_6/O_2 RIE treatment, and all silicon substrates contained silver deposits if they have been previously treated by SF_6/O_2 RIE. Furthermore,

experiments to form silver deposits on RIE-treated silicon wafer that contained no lithographic patterns tested negatively (Figure 6.2d), with only unperturbed AgNCs occasionally adhering to the surface. These tests indicate that the RIE process makes the silicon reactive towards silver nanoparticles and that the EBL step has an indirect role in facilitating the solid-solid silver transformation. To exclude the possibility that sensitized PMMA polymer chains interacted with the AgNCs to form the deposits, the transformation was demonstrated to occur also (i) when PMMA was replaced by Shipley 1813 photoresist and e-beam lithography was replaced by photolithography (Figure 6.3e) and (ii) after the removal of the resist with an organic solvent.

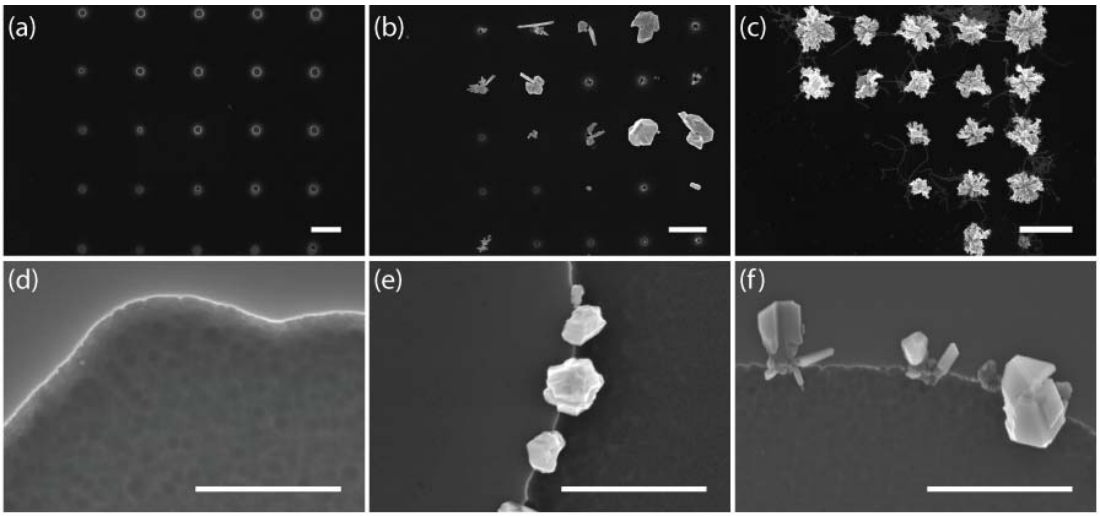

Figure 6.3. Deposits in EBL-patterned dose matrices (Exposure dose: 70 – 214 $\mu C/cm^2$) using different sources of silver: (a) 1 mM $AgNO_3$ in EtOH, (b) 1 mM AgNCs in EtOH, and (c) 1 mM AgNSs in water. Deposits in photolithography-patterned step edges using different sources of silver: (d) 1 mM $AgNO_3$ in water, (e) 0.5 mM AgNCs in water, and (f) 0.025 mM AgNSs in water. Substrates (d-f) were cleaned with O_2 plasma for 45 sec prior to the reaction with silver. All scale bars: 1 μm.

Experiments were repeated with different sources of silver, namely Ag(I) ions from solvated $AgNO_3$ (Figures 6.3a and 6.3d), PVP-coated AgNCs (Figures 6.3b and 6.3e) and borate-coated AgNSs (Figures 6.3c and 6.3f). The AgNCs and AgNSs

formed silver deposits on the edges of EBL and photolithography patterns. Silver deposits *did not* form when using the $AgNO_3$ solutions. The nanoparticle suspensions may contain trace amounts of silver ions, but substantially less than 1 mM, the concentration of Ag(I) in the $AgNO_3$ solutions. . These experiments establish that silver deposits do not form through the reduction of silver ions from solution. When supplied with a high concentration of AgNSs (1 mM), the solid-solid transformation resulted in two new silver deposit morphologies: Nanoflowers, similar to the dendritic morphologies seen with AgNCs but lacking facetted regions, and Nanofilaments with high aspect-ratios. These morphologies suggest that the reaction rate is higher for the AgNSs compared to the AgNCs. The stronger driving force for the reaction with AgNSs may originate from their smaller size, their lattice defects (*e.g.* twin planes) or the weak surface passivation by the borate groups. With lower concentrations of AgNSs (25 μM) and larger patterns, dense and facetted silver nanoparticles were obtained with AgNSs, predominantly in platelet shape (Figure 6.3f).

6.3.2 Mechanism of the Solid-Solid Transformation of Silver Nanoparticles

The aggregated evidence presented in section 3.1 suggests that the formation of silver deposits on patterned silicon substrates is a reaction that is unique to metallic nanoparticles. The reaction observed here does not result in galvanic exchange. Silver does not change its oxidation state when transforming from reactant to product. The rate of reduction of silver ions on silicon is insignificant under the reaction conditions, because of the absence of an etchant for the semiconductor (*e.g.* HF). The reaction is induced by SF_6/O_2 RIE and is localized to the vertical side-walls of lithographic patterns. The reaction proceeds with nanoparticles of different shapes,

sizes and surfactants, in water and EtOH as solvents, and is independent of the type of resist used for patterning.

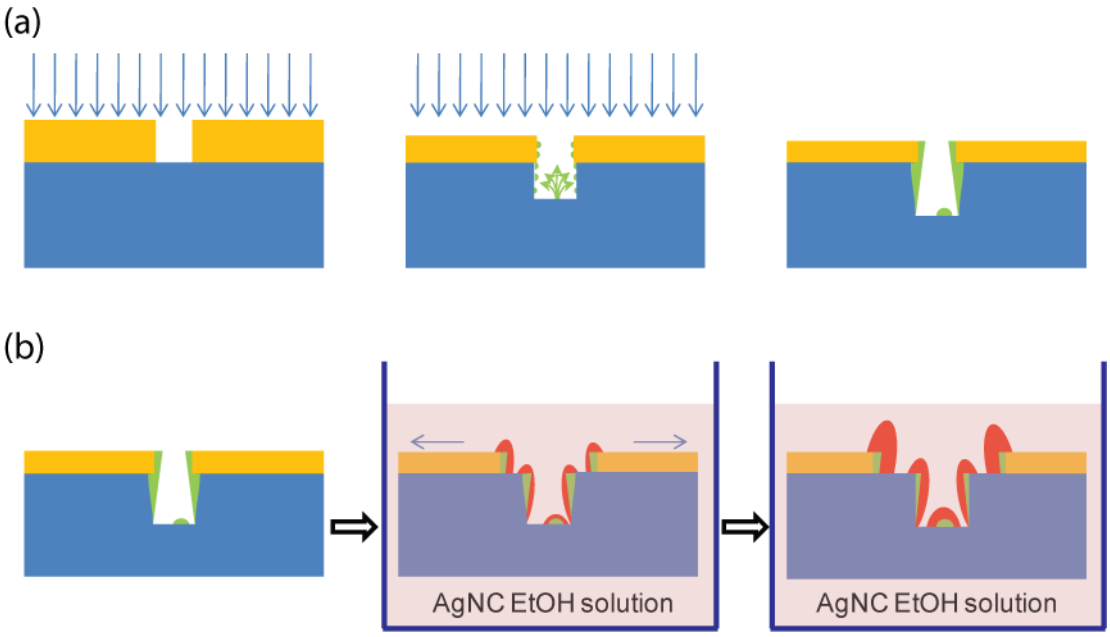

Scheme 6.1. (a) The redeposition of RIE products in a trench. (b) Formation of silver deposits and the shrinkage of PMMA. Color Key: BLUE - silicon substrate; YELLOW – resist; GREEN – reactive ion etching products (SiOxFy); PINK – silver nanocube suspension; RED – silver.

The proposed reaction mechanism involves the interaction of silver nanoparticles with residual products of the RIE process. In RIE processes, plasma components remove material from the substrate via a combination of physical and chemical etching. RIE of Si using fluorine-based plasmas results in a surface layer of SiF_x and amorphized silicon.[76-78] Reaction of silver with dangling bonds in this surface layer[79] is excluded as the main mechanism for silver deposition, because deposits were found on the edge of the resist and were not found on the planar wafer. Based on the localization of the silver deposits to the vertical walls, the reaction is proposed to involve sputtered RIE etch products. These products originate from molecular fragments that are ejected from the substrate when it is impinged by

energetic ions from the plasma.[80-82] Molecular fragments that are ejected from the bottom of the patterns either dissipate into the plasma or collide with the walls of the pattern and redeposit there.[83] With SF6/O_2 etching plasmas, the products found on the sidewall have the composition SiO_xF_y.[84-86] The redeposition of the sputtered fragments is critical for the sidewalls passivation that leads to the anisotropic etch and vertical features.[84, 87, 88] As a consequence of the shape evolution of the pattern and the etch undercut, redeposition of RIE products is more prevalent in high-aspect ratio features, on the side-walls compared to the horizontal surfaces, and on the upper sections of the vertical walls. The distribution of silver deposits in the patterns perfectly matches the anticipated distribution of redeposited RIE products. The redeposition of the sputtered products and the subsequent formation of silver nanoparticle, including the effect of solvent on the resist layer, are illustrated in Scheme 6.1. The RIE sputtered products that initiate the transformation of the silver particles are expected to consist mainly of non-volatile polymeric fluorosilicon and fluoroxysilicon radicals. It is possible that they also incorporate carbon and hydrogen from RIE products of the resist. The sputtered products store chemical energy that is sufficiently large to detach atoms (or clusters) from the AgNCs and AgNSs. Silver can be regarded as catalyzing the decomposition of the fluoroxysilicon radicals. The rate of the reaction slows as the reaction progresses, as the more energetic chemical species are consumed. As SiO_xF_y is removed from the silicon surface, the metal fragments bond to it and form silver deposits bearing a completely new shape. The solid-solid reactions occurring at the interface between the etched silicon and the ligand-capped silver nanoparticle are not known at this point.

With the growing trend of incorporating nanomaterials with other technologies, new chemical transformations exclusive to the nanoscale will continue to be discovered. The unique properties of nanostructures and their tunability with size, however, make it particularly difficult to predict their chemical, mechanical and electronic interactions with micro- and macro-scale objects. This element of serendipity provides technological challenges and opportunities. In the following sections, we show that the unique silver transformation studied in this article can be applied advantageously to the selective growth of gold nanoparticles and silicon nanowires from the side walls of lithographically patterned trenches. Such nanobeams and nanobridges made of silicon nanowires are of interest for the miniaturization of electronic and acoustic devices.[89-92]

6.3.3 Controlling Silver Nanoparticle Deposition on Sidewalls

The insights gained through the study of the conditions affecting the solid-solid transformation of the silver nanoparticles can be used to eliminate the reaction or to engineer the reaction to proceed more uniformly. For example, we will seek to eliminate the transformation when we are interested in preserving the cubic shape of nanoparticles deposited on the substrate for their plasmonic properties, which are shape dependent.[45] Alternatively, we will seek to generate deposits uniform in size on patterned vertical walls when we are interested in assembling overhanging nanostructures.[89, 90, 92-95]

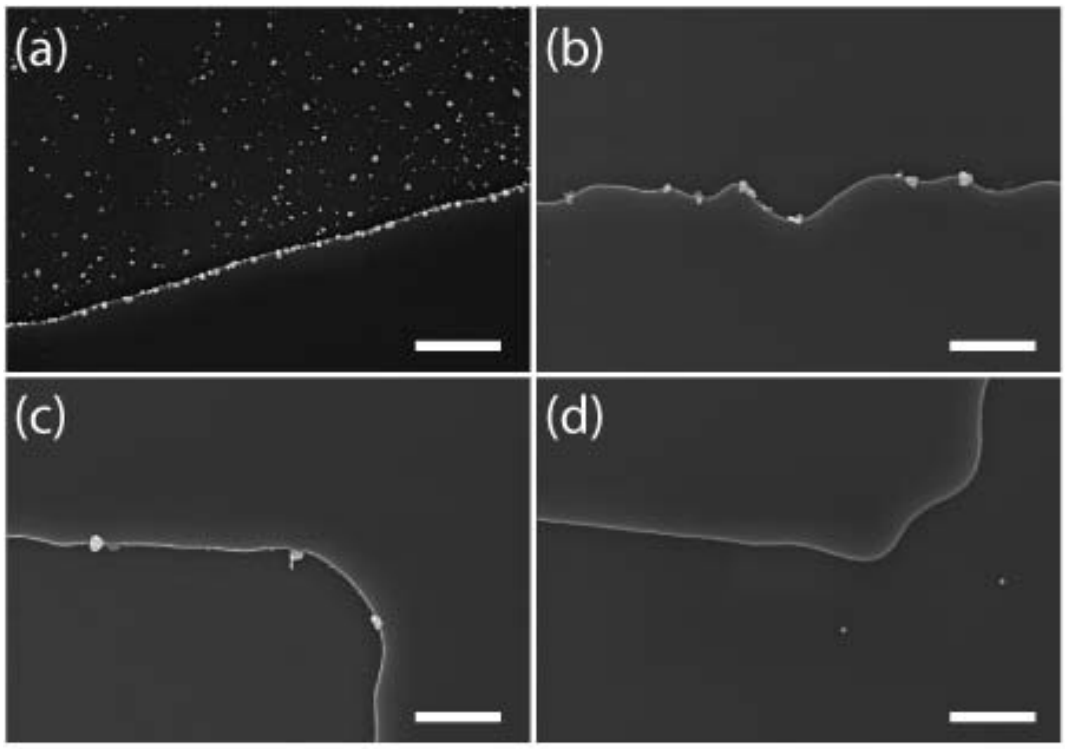

Figure 6.4. Influence of oxygen plasma on the distribution of silver deposits on the patterned silicon surface. Duration of O_2 plasma treatment: (a) 0sec, (b) 30sec, (c) 60sec, and (d) 150sec. Duration of growth: 30 min. All scale bars: 2 μm.

The solid-solid transformation can be suppressed by removing the redeposited RIE products prior to immersing the substrate in the nanoparticle suspension. RIE products can be selectively removed using an oxygen plasma treatment. Moreover, by tuning the duration of the O_2 plasma treatment it is possible to regulate the amount and distribution of silver deposits formed on the substrate. Figure 6.4 shows the distribution of deposits at the edge of a wide trench as a function of O_2 plasma treatment duration. In this example, after the RIE process and the dissolution of the resist in acetone, an oxygen plasma treatment was carried out for 0 to 150 seconds followed by soaking in the AgNC EtOH suspension for 30 min. The substrate that experienced no oxygen plasma (Figure 6.4a) is dotted with silver deposits both on the vertical wall and on the floor of the trench. The substrate that was treated for 150 sec

by O_2 plasma did not promote any transformations in the AgNCs (Figure 6.4d). With intermediate durations, the nucleation of silver deposits was restricted to the vertical side walls of the patterns, with fewer nucleation sites and larger deposits the longer the oxygen plasma treatment. Clearly the O_2 plasma treatment is capable of converting the redeposited RIE radicals to volatile or inactive forms. Because of shadow effects, the action of the plasma is most effective on horizontal surfaces and least effective on vertical/overhanging surfaces.

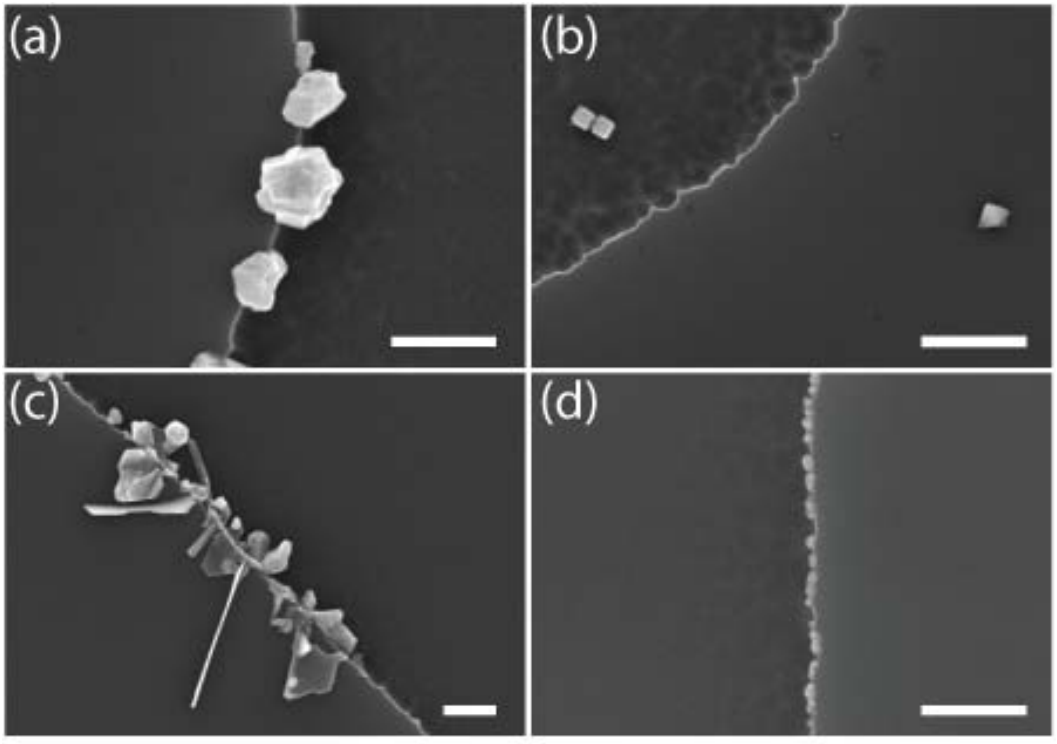

Figure 6.5. Deposits in photolithography-patterned step edges grown in DI water with (a) 0.5 mM PVP-capped AgNCs, (b) 0.5 mM MBuOH-capped AgNCs, (c) 0.025 mM borate-capped AgNSs, and (d) 0.025 mM MBuOH-capped AgNSs. The substrates were treated with O_2 plasma for 45 sec prior to the reaction with silver. Duration of growth: 15 hrs. All scale bars: 500 nm.

The transformation can also be chemically controlled by adjusting the affinity of the ligands to the surface of the nanoparticles. The AgNCs and AgNSs were coated with 4-mercapto-1-butanol by a ligand exchange process. The thiol molecule is

known to effectively passivate the surfaces of silver nanocrystals, particularly the {001} planes which terminate our AgNCs. In Figure 6.5 we compare the results of submerging O_2 plasma-treated, photolithographically-patterned silicon wafers for 2 hours in ethanoic suspensions of AgNCs and AgNSs before and after ligand exchange. The process with PVP-coated AgNCs and borate-coated AgNSs resulted in large deposits on the sidewall (Figures 6.5a and 6.5c). MBuOH-coated AgNCs yielded no deposits on the patterned substrate (Figure 6.5b), while MBuOH-coated AgNSs resulted in small deposits (Figure 6.5d). This comparison illustrates that surface modifications affect both the ability of the nanoparticle to participate in the solid-solid transformation and the shape of the silver deposits on the silicon surface. The thiol-capped nanoparticles show the lower efficiency and more uniformity in generating deposits when compared to their PVP-capped and borate-capped counterparts. Thus, it is plausible that the solid-solid transformation is initiated by contact between the redeposited RIE products and a bare area on the silver nanoparticle surface. The ligands may also affect the outcome of the reaction by adsorbing on the growing deposit, although their concentration in the reaction mixture is typically not high.

6.3.4 Sidewall Localization of Silicon Nanowires

The controlled deposition of nanoscale silver on the side-walls of silicon structures (*e.g.* mesas) can be utilized to seed the deposition and the growth of other types of nanostructures and materials in the same locations. We turn our attention to the seeding of gold nanoparticles and the growth of silicon nanowires. Silver is

exchanged galvanically with more noble metals under mild conditions. In Figures 6.6a and 6.6b the products of galvanic exchange with chloroauric acid are shown. Simultaneous Au plating and Ag dissolution lead to the formation of perforated nanoshells of golds on the sites where silver deposits previously resided. Despite gold not plating on bare silicon surfaces, the Au products of the galvanic exchange with silver adhered well to the edges of the patterns. No residual silver was detected by energy dispersive spectroscopy (EDS) performed in the SEM. The seeded Au nanoparticles were employed to catalyze the CVD growth of silicon nanowires. The Au catalyst mediates the one-dimensional growth of the silicon crystal (suppressing three-dimensional growth) and determines also the site of attachment of the nanowire to the substrate. Gold is a suitable catalyst for the growth of a variety of inorganic nanowires by the VLS mechanism, namely of those materials with which Au forms a eutectic. Silver may also act as a catalyst for nanowire growth without the need for galvanic exchange. As can be appreciated from Figures 6.6c and 6.6d the Au nanoparticles were highly effective in growing silicon nanowires so that the edges of the patterns became covered with a dense forest of ultra-thin nanowires. Additionally, there are thicker nanowires that are straight, more spaced out and project off the pattern edge. The latter would be useful as nano-cantilevers or as horizontal conductors bridging over a trench. Further optimization of the lithographic pattern and the nanowire growth conditions is needed to achieve reproducible growth for device fabrication.

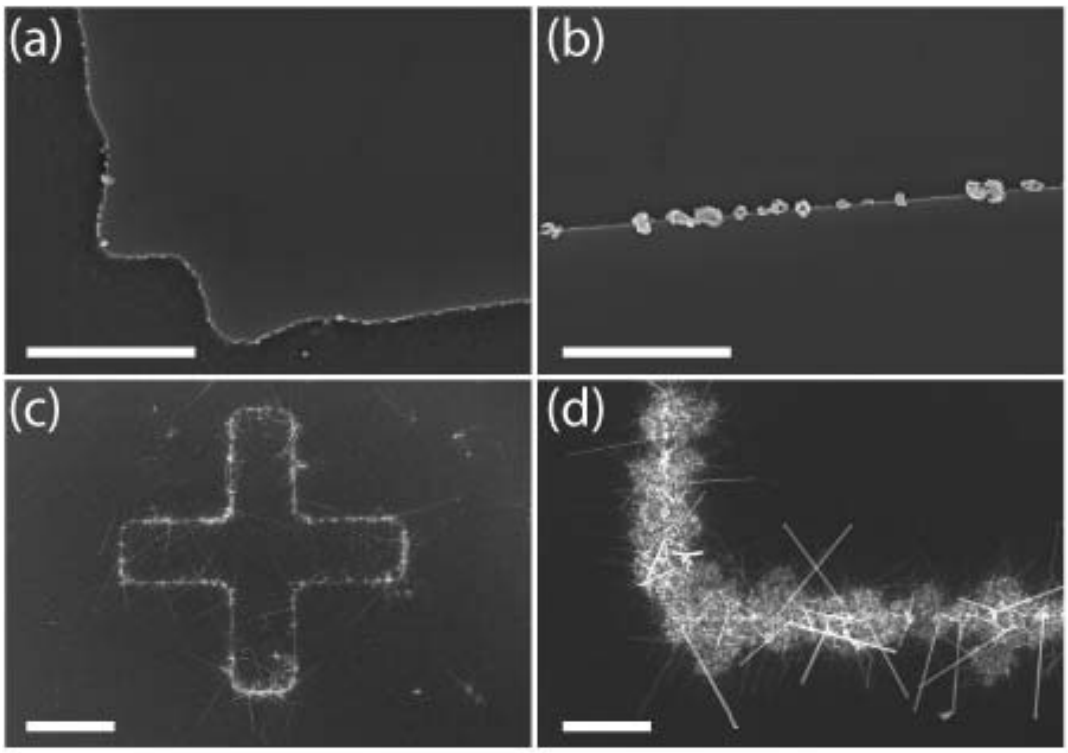

Figure 6.6. SEM images of (a, b) gold nanoparticles formed via galvanic exchange and (c, d) silicon nanowires grown via gold-catalyzed CVD. The nanostructures are localized to the edges of the lithographic patterns. 0.025 mM MBuOH-capped AgNSs were used as precursors in figures (a) and (c) and 0.5 mM PVP-capped AgNCs were used for (b) and (d). The substrates were treated with O_2 plasma for 60 sec prior to the reaction with silver. Duration of growth: 15 hrs. Scale bar: (a) 2 μm (b) 4 μm (c) 16 μm and (d) 8 μm.

6.4 Conclusions

Mixing reactive ion etched silicon substrates with silver nanoparticles results in a dramatic change in the nanoparticle shape and metal deposition mediated by redeposited RIE products that accumulate primarily along the side-walls of the patterns. The transformation is unique to metal nanoparticles, and can be modulated by controlling the particle type, the surfactants, and the distribution of reactive sites on the silicon wafer. Facetted, globular, dendritic, and fiber-like deposits of silver were obtained. The metal deposits can facilitate the growth of other nanostructures on

the vertical walls of patterns. This process could be the basis for the simple fabrication of acoustic and electronic devices. The combination of bottom-up and top-down approaches for nanofabrication will certainly result in the discovery of atypical transformations that do not occur under other circumstances.

7 Conclusions

To investigate several parameters affecting SERS enhancement, we needed to develop an efficient deposition method guiding metal nanoparticles into predetermined positions. We demonstrated metal nanoparticle deposition with three different methods: vertical deposition, electrophoretic deposition (EPD), and block-copolymer templated deposition (BCPTD).

In the vertical deposition utilizing capillary force, AgNC dimers were successfully formed in pre-determined position by trapping the AgNCs in cavities in pre-patterned substrates. This technique enabled us to analyze more than 200 AgNC dimers.

The EPD method is very efficient in forming large clusters of AgNCs. We succeeded in forming AgNC trimers and tetramers with good linear alignment. The deposition time and the applied potential are important factors in controlling the EPD process. They are easy to control.

In the BCPTD, hexagonal arrays of gold nanospheres were successfully formed by chemically modified PS-*b*-P4VP templates. Selective deposition of the gold nanospheres onto the P4VP domains was achieved by the attractive electrostatic interaction between them.

In these ways, we formed various nanostructures with metal nanoparticles and investigated the correlation between SERS enhancement to various structural parameters.

We demonstrated that proximity of plasmon resonance frequency of SERS substrates to laser frequency is essential to maximize SERS enhancement. It was observed that the maximum EF values increase as the laser wavelength increases from 515nm to 784nm. The increase of the SERS enhancement correlates with the increase of the ratio of the real part to the imaginary part of the dielectric constant of gold in this wavelength range.

As the AgNC cluster size increases from dimer to tetramer, the average of the SERS enhancement factors increases and, with the 784nm laser, the dispersion of the SERS enhancement factors decreases. Additionally, the portion of silent AgNC clusters decreases with cluster size and was completely eliminated by using AgNC tetramers. Thus, large AgNC clusters are better for SERS enhancement with 633nm and 784nm lasers.

Non-FF clusters of AgNCs are better for SERS enhancement than FF clusters despite of smaller number of sample molecules at the junction area. It is inferred that sharp corners at the junction area in non-FF clusters generate a higher electric field enhancement, compensating for the lower number of molecules in the junction area.

We demonstrated our approach to form isolated metal nanoparticle clusters. By adopting our approach, other researchers can easily prepare a large number of clusters and investigate their properties. We elucidated the effect of several geometrical parameters of metal nanostructures on SERS enhancement. Using our methodology, we have determined the preferred configurations of AgNC clusters for achieving large SERS enhancements. Researchers can used these recommendations to fabricate reliable SERS substrate.

8 Appendix

Criteria for assignment of dimers to EE, FE and FF groups
General: All dimers consist of two nanocubes, separated by less than 10nm. The average edge length of the cubes is 80nm.

Consider the projection of a dimer onto the surface of the substrate, indicated in the schematic below:

(1) Identify the corner of one cube that is closest to a face of the adjacent cube. Mark the corner point P, and draw a line A along the projection of the face. (Scheme 1)

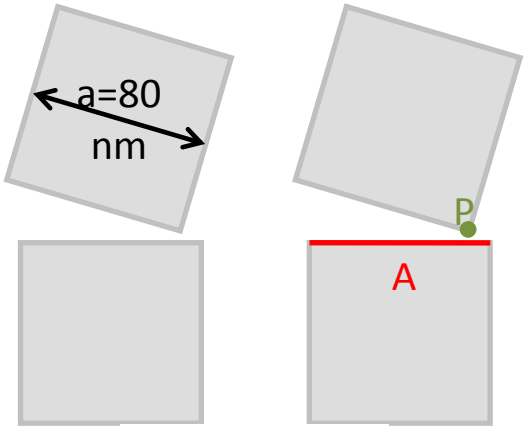

SCHEME 1

(2) Draw a line B through point P perpendicular to A. Line B splits A into two segments. Is one segment longer than $2/3$ of the cube edge? (Scheme 2)

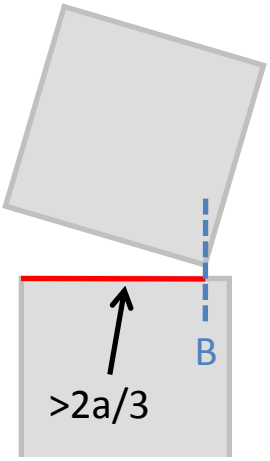

SCHEME 2

(2a) **If YES**: Consider the longer of these two segments. Identify the face of the cube containing point P that is on the same side of line B as this segment. Draw a line C along the projection of the face. Draw a line A' through point P parallel to A. Is the angle between A' and C larger than 10°? (Scheme 3)

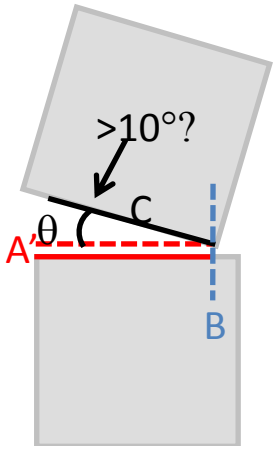

SCHEME 3

Assignment:

One segment > 2a/3 θ >10°	EE
One segment > 2a/3 θ >10°	FF

(2b) **If NO**: Identify the faces of the cube containing point P. Draw lines C and C' along the projections of the faces. Draw a line A' through point P parallel to A. Is the angle between A' and C (or C') smaller than 10° or larger than 80°? (Scheme 4)

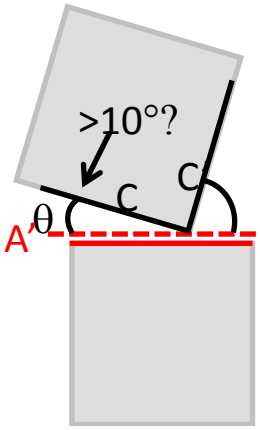

SCHEME 4

Assignment:

Both segments < 2a/3 θ < 10° or θ >80°	FF
Both segments < 2a/3 10° < θ < 80°	FE

9 References

1. Raman, C.V. and K.S. Krishnan, *A New Type of Secondary Radiation.* Nature, 1928. **121**(3048): p. 501-502.
2. Campion, A. and P. Kambhampati, *Surface-enhanced Raman scattering.* Chemical Society Reviews, 1998. **27**(4): p. 241-250.
3. Blackie, E.J., E.C. Le Ru, and P.G. Etchegoin, *Single-Molecule Surface-Enhanced Raman Spectroscopy of Nonresonant Molecules.* Journal of the American Chemical Society, 2009. **131**(40): p. 14466-14472.
4. Jeanmaire, D.L. and R.P. Vanduyne, *Surface Raman Spectroelectrochemistry .1. Heterocyclic, Aromatic, and Aliphatic-Amines Adsorbed on Anodized Silver Electrode.* Journal of Electroanalytical Chemistry, 1977. **84**(1): p. 1-20.
5. Schatz, G.C. and R.P. Van Duyne, *Theory and Instrumentation*. Handbook of Vibrational Spectroscopy, ed. J.M. Chalmers and P.R. Griffiths. Vol. 1. 2002, New York: Wiley.
6. Willets, K.A. and R.P. Van Duyne, *Localized surface plasmon resonance spectroscopy and sensing.* Annual Review of Physical Chemistry, 2007. **58**: p. 267-297.
7. Mie, G., *Beiträge zur Optik trüber Medien.* Ann. d. Physik, 1908. **25**: p. 377-445.
8. Kreibig, U. and M. Vollmer, *Optical Properties of Metal Clusters*. 1995, Berlin, German: Springer.
9. Sherry, L.J., et al., *Localized surface plasmon resonance spectroscopy of single silver nanocubes.* Nano Letters, 2005. **5**(10): p. 2034-2038.
10. Sherry, L.J., et al., *Localized surface plasmon resonance spectroscopy of single silver triangular nanoprisms.* Nano Letters, 2006. **6**(9): p. 2060-2065.
11. Schatz, G.C., *Theoretical-Studies of Surface Enhanced Raman-Scattering.* Accounts of Chemical Research, 1984. **17**(10): p. 370-376.
12. Michaels, A.M., J. Jiang, and L. Brus, *Ag nanocrystal junctions as the site for surface-enhanced Raman scattering of single Rhodamine 6G molecules.* Journal of Physical Chemistry B, 2000. **104**(50): p. 11965-11971.
13. Haynes, C.L., A.D. McFarland, and R.P. Van Duyne, *Surface-enhanced Raman spectroscopy.* Analytical Chemistry, 2005. **77**(17): p. 338a-346a.
14. Jain, P.K., W.Y. Huang, and M.A. El-Sayed, *On the universal scaling behavior of the distance decay of plasmon coupling in metal nanoparticle pairs: A plasmon ruler equation.* Nano Letters, 2007. **7**(7): p. 2080-2088.
15. Schuck, P.J., et al., *Improving the mismatch between light and nanoscale objects with gold bowtie nanoantennas.* Physical Review Letters, 2005. **94**(1): p. 0174020-0174023.
16. Wang, H.H., et al., *Highly Raman-enhancing substrates based on silver nanoparticle arrays with tunable sub-10 nm gaps.* Advanced Materials, 2006. **18**(4): p. 491-495.
17. Siegfried, T., et al., *Fabrication of sub-10 nm gap arrays over large areas for plasmonic sensors.* Applied Physics Letters, 2011. **99**(26): p. 263302-3.

18. Hatab, N.A., et al., *Free-Standing Optical Gold Bowtie Nanoantenna with Variable Gap Size for Enhanced Raman Spectroscopy.* Nano Letters, 2010. **10**(12): p. 4952-4955.
19. Barrow, S.J., et al., *Surface Plasmon Resonances in Strongly Coupled Gold Nanosphere Chains from Monomer to Hexamer.* Nano Letters, 2011. **11**(10): p. 4180-4187.
20. Chen, G., et al., *Measuring Ensemble-Averaged Surface-Enhanced Raman Scattering in the Hotspots of Colloidal Nanoparticle Dimers and Trimers.* Journal of the American Chemical Society, 2010. **132**(11): p. 3644-3645.
21. Wustholz, K.L., et al., *Structure-Activity Relationships in Gold Nanoparticle Dimers and Trimers for Surface-Enhanced Raman Spectroscopy.* Journal of the American Chemical Society, 2010. **132**(31): p. 10903-10910.
22. Rodriguez-Fernandez, J., et al., *Seeded growth of submicron Au colloids with quadrupole plasmon resonance modes.* Langmuir, 2006. **22**(16): p. 7007-7010.
23. Yao, H., et al., *DNA-directed self-assembly of gold nanoparticles into binary and ternary nanostructures.* Nanotechnology, 2007. **18**(1): 015102.
24. Rycenga, M., et al., *Surface-Enhanced Raman Scattering: Comparison of Three Different Molecules on Single-Crystal Nanocubes and Nanospheres of Silver.* Journal of Physical Chemistry A, 2009. **113**(16): p. 3932-3939.
25. Sun, Y.G. and Y.N. Xia, *Shape-controlled synthesis of gold and silver nanoparticles.* Science, 2002. **298**(5601): p. 2176-2179.
26. Tao, A., P. Sinsermsuksakul, and P.D. Yang, *Polyhedral silver nanocrystals with distinct scattering signatures.* Angewandte Chemie-International Edition, 2006. **45**(28): p. 4597-4601.
27. Wiley, B., et al., *Polyol synthesis of silver nanoparticles: Use of chloride and oxygen to promote the formation of single-crystal, truncated cubes and tetrahedrons.* Nano Letters, 2004. **4**(9): p. 1733-1739.
28. Skrabalak, S.E., et al., *On the polyol synthesis of silver nanostructures: Glycolaldehyde as a reducing agent.* Nano Letters, 2008. **8**(7): p. 2077-2081.
29. McLellan, J.M., et al., *The SERS activity of a supported Ag nanocube strongly depends on its orientation relative to laser polarization.* Nano Letters, 2007. **7**(4): p. 1013-1017.
30. Camargo, P.H.C., et al., *Measuring the surface-enhanced Raman scattering enhancement factors of hot spots formed between an individual Ag nanowire and a single Ag nanocube.* Nanotechnology, 2009. **20**(43): 434020.
31. Camargo, P.H.C., et al., *Measuring the SERS enhancement factors of dimers with different structures constructed from silver nanocubes.* Chemical Physics Letters, 2010. **484**(4-6): p. 304-308.
32. Rycenga, M., et al., *Generation of Hot Spots with Silver Nanocubes for Single-Molecule Detection by Surface-Enhanced Raman Scattering.* Angewandte Chemie-International Edition, 2011. **50**(24): p. 5473-5477.
33. Camargo, P.H.C., et al., *Isolating and Probing the Hot Spot Formed between Two Silver Nanocubes.* Angewandte Chemie-International Edition, 2009. **48**(12): p. 2180-2184.

34. Dadosh, T., et al., *Plasmonic Control of the Shape of the Raman Spectrum of a Single Molecule in a Silver Nanoparticle Dimer.* ACS Nano, 2009. **3**(7): p. 1988-1994.
35. Xu, H.X., et al., *Spectroscopy of single hemoglobin molecules by surface enhanced Raman scattering.* Physical Review Letters, 1999. **83**(21): p. 4357-4360.
36. Yin, Y.D., et al., *Template-assisted self-assembly: A practical route to complex aggregates of monodispersed colloids with well-defined sizes, shapes, and structures.* Journal of the American Chemical Society, 2001. **123**(36): p. 8718-8729.
37. Yan, B., et al., *Engineered SERS Substrates With Multiscale Signal Enhancement: Nanoplarticle Cluster Arrays.* ACS Nano, 2009. **3**(5): p. 1190-1202.
38. Gole, A., S.R. Sainkar, and M. Sastry, *Electrostatically Controlled Organization of Carboxylic Acid Derivatized Colloidal Silver Particles on Amine-Terminated Self-Assembled Monolayers.* Chemistry of Materials, 2000. **12**(5): p. 1234-1239.
39. Itoh, T., K. Hashimoto, and Y. Ozaki, *Polarization dependences of surface plasmon bands and surface-enhanced Raman bands of single Ag nanoparticles.* Applied Physics Letters, 2003. **83**(11): p. 2274-2276.
40. Du, C.L., et al., *Polymer-encapsulated silver nanoparticle monomer and dimer for surface-enhanced Raman scattering.* Chemical Physics Letters, 2009. **473**(4-6): p. 317-320.
41. Besra, L. and M. Liu, *A review on fundamentals and applications of electrophoretic deposition (EPD).* Progress in Materials Science, 2007. **52**(1): p. 1-61.
42. Bailey, R.C., K.J. Stevenson, and J.T. Hupp, *Assembly of micropatterned colloidal gold thin films via microtransfer molding and electrophoretic deposition.* Advanced Materials, 2000. **12**(24): p. 1930-1934.
43. Zhang, Q.L., et al., *Controlled placement of CdSe nanoparticles in diblock copolymer templates by electrophoretic deposition.* Nano Letters, 2005. **5**(2): p. 357-361.
44. Giersig, M. and P. Mulvaney, *Formation of Ordered 2-Dimensional Gold Colloid Lattices by Electrophoretic Deposition.* Journal of Physical Chemistry, 1993. **97**(24): p. 6334-6336.
45. Lee, S.Y., et al., *Dispersion in the SERS Enhancement with Silver Nanocube Dimers.* ACS Nano, 2010. **4**(10): p. 5763-5772.
46. Moran, C.H., et al., *Replacement of Poly(vinyl pyrrolidone) by Thiols: A Systematic Study of Ag Nanocube Functionalization by Surface-Enhanced Raman Scattering.* Journal of Physical Chemistry C, 2011. **115**(44): p. 21852-21857.
47. McMahon, J.A., et al., *Correlating the Structure, Optical Spectra, and Electrodynamics of Single Silver Nanocubes.* Journal of Physical Chemistry C, 2009. **113**(7): p. 2731-2735.

48. Guo, L.H., et al., *Nanoarray-Based Biomolecular Detection Using Individual Au Nanoparticles with Minimized Localized Surface Plasmon Resonance Variations.* Analytical Chemistry, 2011. **83**(7): p. 2605-2612.
49. Bates, F.S. and G.H. Fredrickson, *Block Copolymer Thermodynamics - Theory and Experiment.* Annual Review of Physical Chemistry, 1990. **41**: p. 525-557.
50. Mathur, A., A.D. Brown, and J. Erlebacher, *Self-ordering of colloidal particles in shallow nanoscale surface corrugations.* Langmuir, 2006. **22**(2): p. 582-589.
51. Zehner, R.W., et al., *Selective decoration of a phase-separated diblock copolymer with thiol-passivated gold nanocrystals.* Langmuir, 1998. **14**(2): p. 241-244.
52. Shenhar, R., et al., *Crosslinked nanoparticle stripes and hexagonal networks obtained via selective patterning of block copolymer thin films.* Advanced Materials, 2005. **17**(18): p. 2206-2210.
53. Choi, J.H., S.M. Adams, and R. Ragan, *Design of a versatile chemical assembly method for patterning colloidal nanoparticles.* Nanotechnology, 2009. **20**(6): 065301.
54. Wang, Y., et al., *Nanostructured Gold Films for SERS by Block Copolymer-Templated Galvanic Displacement Reactions.* Nano Letters, 2009. **9**(6): p. 2384-2389.
55. Yang, E.L., et al., *Nanofabrication of surface-enhanced Raman scattering device by an integrated block-copolymer and nanoimprint lithography method.* Journal of Vacuum Science & Technology B, 2010. **28**(6): p. C6m93-C6m97.
56. Sau, T.K. and C.J. Murphy, *Seeded high yield synthesis of short Au nanorods in aqueous solution.* Langmuir, 2004. **20**(15): p. 6414-6420.
57. Mohri, N., et al., *Kinetic-Study on Monolayer Formation with 4-Aminobenzenethiol on a Gold Surface.* Langmuir, 1995. **11**(5): p. 1612-1616.
58. Lam, Y.M., et al., *Controlled chemical stabilization of self-assembled PS-P4VP nanostructures.* Journal of Colloid and Interface Science, 2008. **317**(1): p. 255-263.
59. Genov, D.A., et al., *Resonant Field Enhancements from Metal Nanoparticle Arrays.* Nano Letters, 2003. **4**(1): p. 153-158.
60. Jensen, T.R., et al., *Nanosphere Lithography: Tunable Localized Surface Plasmon Resonance Spectra of Silver Nanoparticles.* The Journal of Physical Chemistry B, 2000. **104**(45): p. 10549-10556.
61. McMahon, J.M., et al., *Gold nanoparticle dimer plasmonics: finite element method calculations of the electromagnetic enhancement to surface-enhanced Raman spectroscopy.* Analytical and Bioanalytical Chemistry, 2009. **394**(7): p. 1819-1825.
62. Jain, P.K., W. Huang, and M.A. El-Sayed, *On the Universal Scaling Behavior of the Distance Decay of Plasmon Coupling in Metal Nanoparticle Pairs: A Plasmon Ruler Equation.* Nano Letters, 2007. **7**(7): p. 2080-2088.
63. Farcau, C. and S. Astilean, *Mapping the SERS Efficiency and Hot-Spots Localization on Gold Film over Nanospheres Substrates.* The Journal of Physical Chemistry C, 2010. **114**(27): p. 11717-11722.

64. Mayergoyz, I.D., Z. Zhang, and G. Miano, *Analysis of dynamics of excitation and dephasing of plasmon resonance modes in nanoparticles.* Physical Review Letters, 2007. **98**(14): p. 147401.
65. Palik, E. and G. Ghosh, *Handbook of optical constants of solids*. 1998, Boston: Academic Press.
66. Haynes, C.L. and R.P. Van Duyne, *Plasmon-Sampled Surface-Enhanced Raman Excitation Spectroscopy.* The Journal of Physical Chemistry B, 2003. **107**(30): p. 7426-7433.
67. Mock, J.J., et al., *Distance-dependent plasmon resonant coupling between a gold nanoparticle and gold film.* Nano Letters, 2008. **8**(8): p. 2245-2252.
68. Park, W.H., S.H. Ahn, and Z.H. Kim, *Surface-Enhanced Raman Scattering from a Single Nanoparticle-Plane Junction.* ChemPhysChem, 2008. **9**(17): p. 2491-2494.
69. Rodriguez-Lorenzo, L., et al., *Zeptomol Detection Through Controlled Ultrasensitive Surface-Enhanced Raman Scattering.* Journal of the American Chemical Society, 2009. **131**(13): p. 4616-4618.
70. Talley, C.E., et al., *Surface-Enhanced Raman Scattering from Individual Au Nanoparticles and Nanoparticle Dimer Substrates.* Nano Letters, 2005. **5**(8): p. 1569-1574.
71. Li, W.Y., et al., *Dimers of Silver Nanospheres: Facile Synthesis and Their Use as Hot Spots for Surface-Enhanced Raman Scattering.* Nano Letters, 2009. **9**(1): p. 485-490.
72. Kim, D.-S., et al., *Real-Space Mapping of the Strongly Coupled Plasmons of Nanoparticle Dimers.* Nano Letters, 2009. **9**(10): p. 3619-3625.
73. Tao, A., P. Sinsermsuksakul, and P. Yang, *Polyhedral Silver Nanocrystals with Distinct Scattering Signatures.* Angewandte Chemie International Edition, 2006. **45**(118): p. 4597-4601.
74. Solomon, S.D., et al., *Synthesis and study of silver nanoparticles.* Journal of Chemical Education, 2007. **84**(2): p. 322-325.
75. Skrabalak, S.E., et al., *Facile synthesis of Ag nanocubes and Au nanocages.* Nature Protocols, 2007. **2**(9): p. 2182-2190.
76. Buyanova, I.A., et al., *Photoluminescence of defects induced in silicon by SF6/O2 reactive-ion etching.* Journal of Applied Physics, 1995. **78**(5): p. 3348-3348.
77. Köster, T., et al., *Optical properties of reactive-ion-etched Si/$Si_{1-x}Ge_x$ heterostructures.* Journal of Vacuum Science & Technology B: Microelectronics and Nanometer Structures, 1996. **14**(2): p. 698-698.
78. Oehrlein, G.S., *Effects of ion bombardment in plasma etching on the fluorinated silicon surface layer: Real-time and postplasma surface studies.* Journal of Vacuum Science & Technology A: Vacuum, Surfaces, and Films, 1993. **11**(1): p. 34-34.
79. Kalkan, A.K. and S.J. Fonash, *Electroless synthesis of Ag nanoparticles on deposited nanostructured Si films.* Journal of Physical Chemistry B, 2005. **109**(44): p. 20779-20785.
80. Oehrlein, G.S., J.F. Rembetski, and E.H. Payne, *Study of Sidewall Passivation and Microscopic Silicon Roughness Phenomena in Chlorine-Based Reactive*

Ion Etching of Silicon Trenches. Journal of Vacuum Science & Technology B, 1990. **8**(6): p. 1199-1211.
81. Min, J.H., et al., *Redeposition of etch products on sidewalls during SiO2 etching in a fluorocarbon plasma. I. Effect of particle emission from the bottom surface in a CF4 plasma.* Journal of Vacuum Science & Technology a-Vacuum Surfaces and Films, 2002. **20**(5): p. 1574-1581.
82. Gray, D.C., V. Mohindra, and H.H. Sawin, *Redeposition kinetics in fluorocarbon plasma etching.* Journal of Vacuum Science & Technology A: Vacuum, Surfaces, and Films, 1994. **12**(2): p. 354-354.
83. Wang, X.D., et al., *Reactive ion beam etching of HfO_2 film and removal of sidewall redeposition.* Journal of Vacuum Science & Technology A, 2006. **24**(4): p. 1067-1072.
84. Jansen, H., et al., *The black silicon method: a universal method for determining the parameter setting of a fluorine-based reactive ion etcher in deep silicon trench etching with profile control.* Journal of Micromechanics and Microengineering, 1995. **5**(2): p. 115-120.
85. Dussart, R., et al., *Passivation mechanisms in cryogenic SF_6/O_2 etching process.* Journal of Micromechanics and Microengineering, 2004. **14**(2): p. 190-196.
86. van der Drift, E., et al., *XPS study on dry etching of Si/Ge_xSi_{1-x}.* Microelectronic Engineering, 1995. **27**(1-4): p. 481-485.
87. D'Emic, C.P., K.K. Chan, and J. Blum, *Deep trench plasma etching of single crystal silicon using SF6/O2 gas mixtures.* Journal of Vacuum Science & Technology B: Microelectronics and Nanometer Structures, 1992. **10**(3): p. 1105-1105.
88. Syau, T., B.J. Baliga, and R.W. Hamaker, *Reactive Ion Etching of Silicon Trenches Using SF_6/O_2 Gas Mixtures.* Journal of The Electrochemical Society, 1991. **138**(10): p. 3076-3076.
89. Feng, X.L., et al., *Very high frequency silicon nanowire electromechanical resonators.* Nano Letters, 2007. **7**(7): p. 1953-1959.
90. He, R.R., et al., *Self-transducing silicon nanowire electromechanical systems at room temperature.* Nano Letters, 2008. **8**(6): p. 1756-1761.
91. Islam, M.S., et al., *A novel interconnection technique for manufacturing nanowire devices.* Applied Physics A-Materials Science & Processing, 2005. **80**(6): p. 1133-1140.
92. Islam, M.S., et al., *Ultrahigh-density silicon nanobridges formed between two vertical silicon surfaces.* Nanotechnology, 2004. **15**(5): p. L5-L8.
93. Lee, J.S., M.S. Islam, and S. Kim, *Direct formation of catalyst-free ZnO nanobridge devices on an etched Si substrate using a thermal evaporation method.* Nano Letters, 2006. **6**(7): p. 1487-1490.
94. Conley, J.F., L. Stecker, and Y. Ono, *Directed integration of ZnO nanobridge devices on a Si substrate.* Applied Physics Letters, 2005. **87**(22): p. 223114.
95. Gao, P.X., et al., *Bridged ZnO nanowires across trenched electrodes.* Applied Physics Letters, 2007. **91**(14): p. 142108.